

# DISSERTATION

to obtain the academic degree  
doctor rerum naturalium (Dr. rer. nat.)  
in Faculty 1 - Physics / Electrical Engineering

---

## MINERAL DUST SIMULATIONS WITH ECHAM6.3-HAM2.3 FOR PRESENT-DAY AND PAST CLIMATE CONDITIONS

---

submitted to the  
UNIVERSITY OF BREMEN  
by

**Stephan Krätschmer**

DATE OF SUBMISSION: August 26, 2022

DATE OF DEFENCE: December 2, 2022

---

- SUPERVISOR & REVIEWER 1 -

Prof. Dr. Gerrit Lohmann

- REVIEWER 2 -

Prof. Dr. Fabrice Lambert



## ABSTRACT

---

Mineral dust aerosol constitutes an important component of the Earth's climate system due to direct and indirect influences on the radiation budget. It also acts as a fertilizer for the biosphere and thus affects the global carbon cycle. Marine sediment cores and ice cores indicate that dust fluxes were substantially higher during glacials compared to warmer climates. Since many physical processes influence dust emission, transport and deposition, mineral dust can be utilized as a climate proxy in order to obtain insights on past climatic conditions in the source regions as well as atmospheric circulation and precipitation patterns.

The aerosol-climate model ECHAM6.3-HAM2.3 is used to perform simulations for present-day (PD), pre-industrial (PI) and Last Glacial Maximum (LGM) climate conditions with a focus on the Southern Hemisphere. A novelty in the model is the fully interactive coupling between climate, vegetation and mineral dust emissions. The comparison to observational data shows that the model results are in good agreement in terms of global dust emissions and regional dust deposition for PD, PI and LGM. However, contrary to data studies, the model suggests that Australia instead of Patagonia represents the predominant source of dust deposited over Antarctica during the LGM. The discrepancy can be traced back to changes in regional climate conditions and precipitation patterns, which in turn are strongly affected by the prescribed sea surface temperatures (SST).

Due to different methods, current SST reconstructions suggest strongly varying global and regional coolings for the LGM. Reducing this uncertainty is of importance in order to assess the Earth's climate sensitivity. Two recent SST datasets, which provide general constraints on possible LGM cooling, are prescribed in the model. The simulated land surface temperatures are compared to data reconstructed based on noble gases in groundwater in order to investigate which SST reconstruction results in a higher agreement. The results are ambiguous. The colder SSTs result in a good agreement in low latitudes, but are systematically too cold in mid-latitudes, and vice versa for the warmer SSTs.

Finally, the sensitivity of the simulated mineral dust cycle to changes in SST is investigated by prescribing both datasets for LGM simulations. The model results suggest that the mineral dust cycle responds strongly to changes in SST in terms of individual dust source strength and contribution to the deposition in high latitudes. The differences can be traced back to regional changes in vegetation and meteorological factors on the one hand, and changes in the atmospheric circulation on the other hand. Generally, the atmospheric circulation during the LGM is characterized by a larger horizontal extent due to lower inertial stability, a reduced vertical extent due to lower temperatures and higher barotropicity during south.-hem. winter.



## PUBLICATIONS

---

**Krätschmer, S.**, van der Does, M., Lamy, F., Lohmann, G., Voelker, C., and Werner, M.: Simulating glacial dust changes in the Southern Hemisphere using ECHAM6.3-HAM2.3, *Climate of the Past*, 18, 67–87, <https://doi.org/10.5194/cp-18-67-2022>, 2022.

**Krätschmer, S.**, Lohmann, G., and Werner, M.: Glacial Sea Surface Conundrum not Resolved: A Modeling Perspective, *Geophysical Research Letters*, 2022 (*submitted*).

**Krätschmer, S.**, Lamy, F., Lohmann, G., Voelker, C., and Werner, M.: Using Mineral Dust to Obtain Insights on the Southern-Hemispheric Dynamics During the Last Glacial Maximum for Different Sea Surface Temperatures, *Atmospheric Chemistry and Physics*, 2022 (*in preparation*).

---

### - CONFERENCE CONTRIBUTIONS -

**Krätschmer, S.**, Werner, M., Lamy, F., Voelker, C., and van der Does, M.: DustIron: Global mineral dust simulations with ECHAM-HAMMOZ for modern and last glacial maximum climate conditions, 22nd EGU General Assembly, held online 4-8 May, <https://doi.org/10.5194/egusphere-egu2020-5463>, 2020.

**Krätschmer, S.**, van der Does, M., Lamy, F., Lohmann, G., Voelker, C., Werner, M.: Mineral dust simulations with ECHAM6.3-HAM2.3 for pre-industrial and last glacial maximum climate conditions with a focus on the Southern Hemisphere, online talk held at Goldschmidt Virtual 4-9 July, 2021.

**Krätschmer, S.**, van der Does, M., Lamy, F., Voelker, C., and Werner, M.: Global mineral dust simulations with ECHAM6.3-HAM2.3 for pre-industrial and last glacial maximum climate conditions using different sea surface temperature reconstructions, eLightning presentation at AGU Fall Meeting 2021, held in New Orleans, LA, 13-17 December, 2021.



## ACKNOWLEDGEMENTS

---

This PhD thesis has been written at the ALFRED WEGENER INSTITUTE (AWI), CENTRE FOR POLAR AND MARINE RESEARCH in Bremerhaven in the period from March 2019 to August 2022.

First of all, I would like to thank my doctoral supervisor GERRIT LOHMANN for giving me the opportunity to work on this topic, for many interesting conversations and his always helpful input on my scientific work.

A very special thanks goes to MARTIN WERNER for his excellent supervision, constant support and his always quick and well-thought feedback on paper drafts, posters, abstracts and other matters.

Last but not least, I would like to thank ...

- PAUL GIERZ, who was always willing to share his profound knowledge of software and programming and helped me many times to solve technical issues.
- NATALJA RAKOWSKY for her quick support with all kinds of HPC-related questions and problems.
- FRANK LAMY, CHRISTOPH VÖLKER and MICHÉLLE VAN DER DOES, who supported my work as members of my Thesis Advisory Committee and gave me lots of helpful input concerning my scientific work.
- DANIEL BALTING and FLORIAN TRYBEL, who provided me with lots of useful feedback after taking their time to read my thesis.
- my colleagues from the PALEO-CLIMATE DYNAMICS working group, who make working at AWI a really pleasant experience and whose company I only got to enjoy for a comparably short amount of time due to 2 years of Corona-related home office.



# CONTENTS

|   |    |
|---|----|
| 1. Introduction . . . . .   | 1  |
| 1.1. Motivation . . . . .   | 1  |
| 1.2. Objectives & Structure of the Thesis . . . . .   | 3  |
| 2. Theory . . . . .   | 6  |
| 2.1. The Climate System . . . . .   | 6  |
| 2.1.1. Components of the Climate System . . . . .   | 6  |
| 2.1.2. Interactions in the Climate System . . . . .   | 9  |
| 2.1.3. Climate Variability & Recent Climate History (800,000 yr) . . . .                                  | 12 |
| 2.2. Mineral Dust in the Climate System . . . . .   | 18 |
| 2.2.1. A Brief Overview on Atmospheric Aerosols . . . . .   | 18 |
| 2.2.2. Physical Processes in the Mineral Dust Cycle . . . . .   | 21 |
| 2.2.3. The Iron Hypothesis . . . . .  | 25 |
| 2.2.4. Mineral Dust as Climate Proxy . . . . .  | 28 |
| 3. Model and Methods . . . . .  | 31 |
| 3.1. ECHAM6.3-HAM2.3 . . . . .  | 31 |
| 3.1.1. Atmospheric General Circulation Model ECHAM6.3 . . . . .   | 32 |
| 3.1.2. Aerosol Model HAM2.3 . . . . .   | 34 |
| 3.2. HPC Environment & Data Analysis . . . . .  | 37 |
| 4. Glacial Dust Changes in the Southern Hemisphere . . . . .  | 41 |
| 4.1. The Role of Mineral Dust During the Last Glacial Maximum . . . . .                                   | 41 |
| 4.2. Simulation Setup and Experiments . . . . .   | 44 |
| 4.3. Results and Discussion . . . . .   | 45 |
| 4.3.1. Model Performance for Present-Day Climate Conditions . . . . .                                     | 45 |
| 4.3.2. The Dust Cycle Under Pre-Industrial and Last Glacial Maximum Climate Conditions . . . . .          | 46 |
| 4.4. Conclusions . . . . .  | 65 |
| 5. Modelling Perspective on the Glacial SST Conundrum . . . . .   | 68 |
| 5.1. The Importance of a Proper SST Reconstruction for the LGM . . . . .                                  | 68 |
| 5.2. Experiments and Experimental Setup . . . . .   | 70 |
| 5.3. Results and Discussion . . . . .   | 71 |
| 5.3.1. Globally and Zonally Simulated Surface Temperature Difference for GLOMAP and Tierney SST . . . . . | 71 |

|  |     |
|--|-----|
| 5.3.2. Comparison of Simulated Land Surface Temperature Anomaly<br>to Reconstructed Data . . . . . | 72  |
| 5.4. Conclusions . . . . .   | 75  |
| 6. Southern-Hemispheric Atmospheric Dynamics During the LGM . . . . .                              | 78  |
| 6.1. The Role of the Atmospheric Circulation for LGM Climate . . . . .                             | 78  |
| 6.2. Experiments and Experimental Setup . . . . .  | 81  |
| 6.3. Results and Discussion . . . . .  | 82  |
| 6.3.1. Mineral Dust Budget for GLOMAP and Tierney et al. SSTs . . . . .                            | 82  |
| 6.3.2. The Atmospheric Circulation During the LGM . . . . .  | 88  |
| 6.4. Summary and Conclusions . . . . .   | 99  |
| 7. Final Considerations . . . . .  | 103 |
| 7.1. Conclusion . . . . .  | 103 |
| 7.2. Outlook . . . . .   | 107 |
| Appendices . . . . .   | 110 |
| A. Model-Data Comparison for Present Day Climate . . . . .   | 111 |
| B. Source Strength Increase vs. Particle Lifetime . . . . .  | 113 |
| References . . . . .   | 116 |

## LIST OF ABBREVIATIONS

---

|        |   |
|--------|---|
| ACCMIP | Atmospheric Chemistry and Climate Model Intercomparison Project |
| AGCM   | Atmospheric General Circulation Model                           |
| AMIP   | Atmospheric Model Intercomparison Project                       |
| AWI    | Alfred Wegener Institute  |
| DJF    | December / January / February                                   |
| EDC    | EPICA Dome C  |
| EPICA  | European Project for Ice Coring in Antarctica                   |
| GLOMAP | Glacial Ocean Map   |
| HNLC   | High Nutrient-Low Chlorophyll                                   |
| HPC    | High Performance Computing                                      |
| IPCC   | Intergovernmental Panel on Climate Change                       |
| JJA    | June / July / August  |
| LGM    | Last Glacial Maximum (21 kyr BP)                                |
| LIG    | Last Interglacial (127 kyr BP)                                  |
| MI     | Meandering Index  |
| MAM    | March / April / May   |
| PCMDI  | Program for Climate Model Diagnosis and Intercomparison         |
| PD     | Present Day   |
| PI     | Pre-industrial (1850-1880 CE)                                   |
| PMIP   | Paleoclimate Modelling Intercomparison Project                  |
| SH     | Southern Hemisphere   |
| SIC    | Sea Ice Concentration   |
| SO     | Southern Ocean  |
| SON    | September / October / November                                  |
| SST    | Sea Surface Temperature   |



# PART I

OBJECTIVES - THEORY - METHODS



"In every outthrust headland, in every curving beach, in every grain of sand there is the story of the Earth."

---

(Rachel Carson)

## 1. INTRODUCTION

### 1.1. MOTIVATION

Mineral dust represents the most abundant atmospheric aerosol species by mass (Kok et al., 2021) and interacts with the Climate System in many ways. Dust particles influence the Earth's energy balance and alter the vertical temperature profile of the atmosphere (Boucher, 2015). In clouds, they affect the formation of precipitation and change their optical properties (Spracklen et al., 2008). Additionally, mineral dust often delivers nutrients to remote areas, e.g. the Amazon rainforest. Consequently, it serves as a fertilizer for the biosphere and therefore exerts an influence on the global carbon cycle (Reichholf, 1986; Schepanski, 2018). The impact on the global climate has in turn regional implications, e.g. in terms of dust emissions (Carslaw et al., 2010; Tegen and Schepanski, 2018).

Serious efforts to include aerosols into atmospheric general circulation models (AGCM) have been made since the 1990s and early 2000s (Tegen and Fung, 1994; Tegen and Lacis, 1996; Stocker, 2011) once it became obvious that the overall effect of their radiative forcing is only poorly constrained and associated with high uncertainties (Penner et al., 2001). However, despite all the progress that has been made since, it is still unclear whether mineral dust in particular has a net-warming or a net-cooling effect (Albani et al., 2014; Kok et al., 2017). The challenges in dust modelling can be traced back to the small spatial and short temporal scales of the underlying physical processes. A combination of wind tunnel experiments, in situ measurements and numerical modelling has shown that the dust emission process, for instance, depends on many small-scale features. These include type, texture and wetness of the soil, vegetation and the atmospheric flow patterns close to the surface, e.g. turbulence. The same holds true for dust transport and deposition, where particle size, shape and mineralogy influence their microphysical and transport properties (Richter and Gill, 2018). All aforementioned processes take place on scales that are far below what current weather and climate models are capable of resolving explicitly due to computational limits. Their considera-

tion relies therefore heavily on parameterizations, i.e. simplified representations of complex physical or chemical processes on the sub-grid scale. Expressed differently, processes involving mineral dust in AGCMs are parameterized based on variables which in turn are also often obtained from parameterizations. Therefore, models commonly still require regional correction factors (*'tuning'*) in order to achieve a reasonable agreement between simulation results and observational data (Cakmur et al., 2006; Knippertz and Todd, 2012).

In numerical weather prediction, the consideration of mineral dust has led to substantial progress in terms of reducing temperature biases in regions with high atmospheric dust loads (Pérez et al., 2006). However, the inclusion of mineral dust into climate models has also been recognized a necessity due to the radiative effects and its importance as a climate proxy. The analysis of ice cores from Antarctica, for instance, has revealed a striking coherence between temperature, CO<sub>2</sub> concentration and mineral aerosol concentration over the last 800 kyr. The results indicate that the dust deposition was high when CO<sub>2</sub> concentration and temperature were low and vice versa (Lambert et al., 2008; Kohfeld and Ridgwell, 2009). This raises naturally the question which long-term role mineral dust plays in the climate system. Due to its known fertilizing effects on marine ecosystems (Martin and Fitzwater, 1988; Martin et al., 1990), it has been suggested that enhanced dust deposition in the Southern Ocean (SO) during glacials caused phytoplankton blooms due to the supply of bioavailable iron. These blooms bound vast amounts of CO<sub>2</sub> dissolved in sea water and thus contributed to the decrease in the atmospheric CO<sub>2</sub> concentration from 280 ppm during interglacials to 190 ppm during the Last Glacial Maximum (LGM) (Martin, 1990). Based on data studies, the upper limit of this effect has been constrained to around 40 ppm (Martínez-García et al., 2011).

Early modelling studies for glacial climate conditions focused mostly on the provenance of dust found in ice cores from both hemispheres and the question whether changes in source strength or atmospheric circulation and transport efficiency were mainly responsible for the increased dustiness during the LGM (Lunt and Valdes, 2001, 2002; Werner et al., 2002; Mahowald et al., 2006). In later studies, increased computational resources and more sophisticated representations of dust in climate models allowed for the investigation of processes depending on particle size and mineralogy. These include the effects of mineral dust on the Earth's radiation balance (Takemura et al., 2009) and particle sorting during transport (Albani et al., 2012). Additionally, a focus has been put on the biogeochemical effects of

dust deposition over the SO during the LGM (Lambert et al., 2015), and how they might have been affected by sea ice (Albani et al., 2016). A more recent research topic is the influence of dust-radiation interactions on climate transitions, e.g. the dynamics of the last deglaciation (Albani and Mahowald, 2019).

## 1.2. OBJECTIVES & STRUCTURE OF THE THESIS

The research documented in this thesis has been performed in the scope of the AWI strategy fund project *DustIron*. This project aims for a improved characterization of the modern and past dust cycle and its link to SO iron fertilization and atmospheric CO<sub>2</sub> via the combination of modelling and data studies by utilizing the expertise of three AWI working groups. The focus of this work is the comprehensive modelling of the atmospheric mineral dust cycle, i.e. the process of dust emission, transport and deposition, for pre-industrial and LGM climate conditions by using a state-of-the-art aerosol-climate model.

The following three research questions are addressed in particular:

1. **How well is the chosen model able to simulate dust fluxes in comparison to observational data for present day, pre-industrial and LGM climate, particularly in the Southern Hemisphere?**

Recent modelling studies still lacked a dynamical vegetation model, and prescribed previously simulated vegetation according to the PMIP3 protocol instead (Albani et al., 2016; Albani and Mahowald, 2019). The novel model setup used in the scope of this thesis provides a fully interactive coupling between dust emissions, dynamic vegetation and climate. This feature is very important because it allows for new insights on the question whether changes in source strength or transport efficiency led to the increased dust deposition over Antarctica during the LGM from a modelling perspective. The assessment of the simulation results focuses particularly on the Southern Hemisphere in terms of dust source strength and contribution depending on meteorological factors, transport characteristics and deposition for pre-industrial (PI) and LGM climate. The simulated deposition fluxes are compared to marine sediment and ice core data (Kohfeld et al., 2013).

2. **Can simulation results help to improve constraining proper, global sea surface temperature reconstructions for the LGM?**

Different reconstruction methods based on different temperature proxies result in sea surface temperatures (SST) datasets for the LGM varying by around

2°C in terms of the suggested global average cooling (Tierney et al., 2020; Paul et al., 2021). Since the model used in this thesis requires the prescription of SSTs as boundary condition, a proper assessment of both datasets is necessary in order to interpret the mineral dust simulation results. A comparison between simulated and reconstructed land surface temperatures for the LGM (Seltzer et al., 2021) might help to tighten the constraints on the question which SST dataset results in better agreement and therefore suggests a more realistic cooling. A reduction in the uncertainty of the reconstructed SSTs for the LGM is of importance in order to assess the Earth's climate sensitivity and therefore to reduce the uncertainty in future climate projections.

**3. What are the effects of prescribing different sea surface temperature reconstructions on the mineral dust cycle and the atmospheric dynamics in the Southern Hemisphere?**

SSTs affect the energy exchange between ocean and atmosphere, the atmospheric circulation and precipitation patterns (Yin and Battisti, 2001; Tharammal et al., 2013). Particularly in the Southern Hemisphere, precipitation has been recognized to be the determining factor in terms of how much mineral aerosol deposits over the SO, respectively, gets transported from the source regions to Antarctica (Markle et al., 2018). Sensitivity studies with both SST reconstructions might yield insights how LGM climate in general and the mineral dust cycle in particular react to the variation. A focus is put on changes in dust source strength and contribution, meteorological factors in the source regions as well as atmospheric circulation patterns such as strength, shape and position of the midlatitude westerlies.

Chapter 2 provides an overview on the Climate System and the role of mineral dust therein. The model and methods are explained in detail in Chapter 3. Chapter 4 has been published in Krätschmer et al. (2022) in *Climate of the Past*. The results of Chapter 5 have been submitted in form of a manuscript to *Geophysical Research Letters* (Krätschmer et al., 2022b, *submitted*). The final Chapter 6 shows the current status of the research, which will be submitted to *Atmospheric Chemistry and Physics* (Krätschmer et al., 2022c, *in preparation*).



"The Earth would only have to move a few million kilometers sunward - or starward - for the delicate balance of climate to be destroyed. The Antarctic icecap would melt and flood all low-lying land; or the oceans would freeze and the whole world would be locked in eternal winter. Just a nudge in either direction would be enough."

---

(Arthur C. Clarke, *Rendezvous with Rama*)

## 2. THEORY

**Summary.** The Climate System consists of five subsystems, which interact with each other by the exchange of matter and energy often in form of cycles and feedback loops. It receives a constant energy flux by the sun, which enables it to maintain a state far away from the thermodynamic equilibrium, and emits longwave radiation back to space. The climate variability is determined by external (solar activity, orbital parameters) and internal (atmospheric composition, changes in albedo and plate tectonics) forcings, and ice cores enable the reconstruction of climate signals like temperature and atmospheric composition for the last one million years. These ice core records indicate that mineral aerosol played a crucial role on glacial-interglacial time scales, which has been suggested to be caused by its fertilizing effects on the marine ecosystem in the Southern Ocean. The knowledge about the underlying physical processes during dust emission, atmospheric transport and deposition enable its utilization as climate proxy.

### 2.1. THE CLIMATE SYSTEM

#### 2.1.1. COMPONENTS OF THE CLIMATE SYSTEM

According to the IPCC (e.g. (Masson-Delmotte et al., 2021)), *Climate* is defined as

“[...] the average weather, or more rigorously, as the statistical description in terms of the mean and variability of relevant quantities over a period of time ranging from months to thousands or millions of years. The classical period for averaging these variables is 30 years, as defined by the World Meteorological Organization (WMO). The relevant quantities are most often surface variables such as temperature, precipitation and wind.”

The aforementioned relevant quantities used to describe the climate are so-called *Climate Elements*, and their entirety including their interactions are considered the *Climate System*. For a methodical investigation, it has proven useful to divide it into five components (e.g. Peixoto and Oort (1992)):

- The **Atmosphere** is the gaseous shell around the Earth, which consists mainly of N<sub>2</sub> (ca. 78%), O<sub>2</sub> (ca. 21%) and Ar (ca. 0.9%), along with some trace gases (e.g. H<sub>2</sub>O, CO<sub>2</sub>, CH<sub>4</sub>). Additionally, it contains several aerosol species, i.e. solid or liquid particulate matter suspended in air, for instance mineral dust, soot or sea salt. In contrast to gases, their concentration usually varies spatially. Some processes taking place here are cloud formation, precipitation, convection, small-scale boundary layer turbulence and large-scale atmospheric circulation. Since many atmospheric processes occur on short timescales, e.g. cloud droplet collisions on 10<sup>-6</sup> s to 10<sup>-3</sup> s Stocker (2011), and due to its low specific heat and density, the response time <sup>1</sup> is rather short, ranging from days to weeks (Peixoto and Oort, 1992).
- The **Hydrosphere** includes all forms of liquid water on Earth, i.e. oceans, lakes, rivers and groundwater, which is approx. 97.8% of all water existing on Earth (Shikazono, 2012). Processes taking place here are a large-scale thermohaline circulation, which is driven by variations in the seawater density due to changes in temperature and salinity, enormous heat transport, small-scale eddies and a substantial exchange of matter, heat and momentum between the Atmosphere and the well-mixed, upper ocean layer (ca. 100 m). Due to its high density, mechanical inertia and heat capacity, it has a rather long response time, ranging from months (ocean mixed layer) up to millenia (deep ocean) (Peixoto and Oort, 1992).
- All water on Earth that exists in a frozen state (ca. 2.2% (Shikazono, 2012)), namely glaciers, sea ice, snow fields and permafrost, are part of the **Cryosphere**. The extend of snowy, respectively, icy surfaces influences how much energy the Earth absorbs from the incoming solar radiation due to its high albedo <sup>2</sup> and has therefore a huge climatic impact. Apart from seasonal variations in

---

<sup>1</sup> The *response time* is the time a system needs to relax back into a energetic equilibrium state after a small perturbation (Peixoto and Oort, 1992).

<sup>2</sup> The term *albedo* describes the reflectivity of a surface ranging from 0 (black body absorption) to 1 (total reflection), usually across the entire wavelength spectrum of the incident solar radiation.

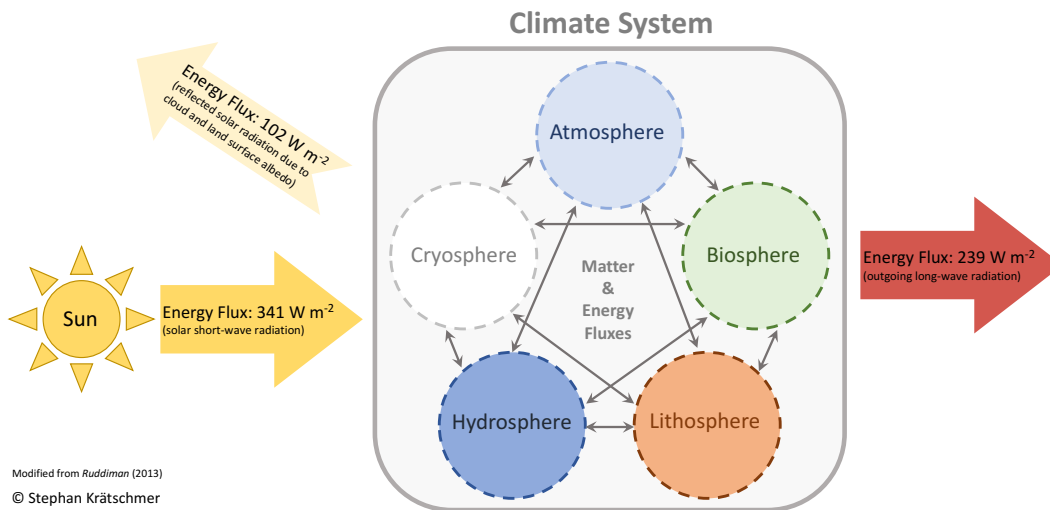
the sea ice extent, typical timescales of processes occurring in the Cryosphere, for instance substantially increasing or decreasing glaciation and thus changes in the sea level, are in the magnitude of tens of thousand of years (Peixoto and Oort, 1992).

- The **Biosphere** includes all terrestrial and marine flora and fauna. An important process taking place here is the gas exchange with the Atmosphere, particularly O<sub>2</sub> and CO<sub>2</sub> in the scope of the photosynthesis and H<sub>2</sub>O due to evapotranspiration, but also many other chemical compounds that act as aerosol precursor. The typical timescales are ranging from hours, e.g. the carbon exchange with the Atmosphere, to centuries, for instance the transformation of vegetation zones (and therefore changes in the albedo) as a response to a changing climate (Stocker, 2011).
- The final component is the **Lithosphere**, which includes all soils and rocks, i.e. basically all continents and the ocean floor. Even though there are continuous interactions with other spheres in terms of matter, energy and momentum, typical timescales of large-scale transformations taking place in this sphere, for instance continental shifts, are in the magnitude of tens of millions to hundreds of millions of years (Peixoto and Oort, 1992; Stocker, 2011).

Although the definition of the term *Climate* suggests that it is only determined by atmospheric processes, the overview on the five different components of the Climate System shows clearly that none of the spheres exists isolated from the others (see Fig. 2.1). Instead, they interact by the exchange of matter (e.g. CO<sub>2</sub> exchange between Biosphere and Atmosphere) and energy (e.g. heat exchange between Hydrosphere and Atmosphere) and are thus thermodynamically open (sub-) systems. The whole Climate System, however, represents in good approximation a closed system, i.e. it exchanges energy with its environment, but no matter <sup>3</sup> (Fieguth, 2017). The next section provides a closer look on the interactions within the Climate System.

---

<sup>3</sup> The Earth receives small amounts of mass by meteors and cosmic dust, and loses small amounts of mass due to space probes and highly energetic molecules. However, these contributions can be neglected.



Modified from Ruddiman (2013)  
© Stephan Krätschmer

**Figure 2.1.** The Climate System receives on average an energy flux of  $341 \text{ W m}^{-2}$  from the sun in form of short-wave radiation (Stocker, 2011). Around 30% is scattered back into space due to the albedo of clouds and the land surface. The remaining energy is taken up by the Climate System, where it is exchanged and driving various matter cycles between the five spheres, before it is finally dissipated and re-emitted into space. [Figure modified from Ruddiman (2013)]

### 2.1.2. INTERACTIONS IN THE CLIMATE SYSTEM

As schematically shown in Fig. 2.1, the Climate System receives on average an energy flux of  $341 \text{ W m}^{-2}$  provided by the sun in form of short-wave radiation. Around 30% ( $102 \text{ W m}^{-2}$ ) of the incoming energy flux is immediately scattered back to space due to clouds and the land surface albedo. The remaining energy is then cycled and distributed among the five subsystems, before it is eventually dissipated on the smallest scale and re-emitted into space in form of long-wave, respectively, infrared radiation. The constant energy supply enables the Climate System to maintain a state far away from the thermodynamic equilibrium.

On an abstract level, all spheres can be considered reservoirs for matter and energy, which are connected by according fluxes. Due to complex and numerous interactions, these fluxes often run in cycles (e.g. the carbon cycle or the hydrologic cycle), which in turn leads to feedback loops either diminishing or nonlinearly amplifying a given variable. This keeps the whole Climate System in a self-stabilized state in form of a dynamic equilibrium, i.e. all climate elements remain within a typical value range. However, that has been suggested to be the case only as long as specific thresholds of several climate elements are not exceeded as a consequence of changes in the forcing (e.g. in the insolation). Previous studies have

tried to identify several of these so-called *tipping elements*, along with boundaries and types of their threshold forcings (Lenton et al., 2008). Once such a threshold (so-called *tipping point*) is exceeded, the whole Climate System might transition into a completely new state. Analytical studies of simple energy balance models and numerical studies with more sophisticated energy balance models indicate that multiple equilibria exist in the Climate System, and that its overall state also depends on the previous climate history, an effect called *hysteresis* (Stocker, 2011); Dortmans et al. (2019). Simulations with more complex, coupled models also suggest the existence of several equilibrium states, albeit with some limitations, e.g. only for an aquaplanet configuration (Manabe and Stouffer, 1988; Ferreira et al., 2011). The actual existence of such tipping elements, their detectability and potential transition mechanisms are the subject of current research (e.g. Bathiany et al. (2016)).

Furthermore, the many different timescales of processes in the subsystems lead to strongly varying response times after perturbations in the mass or energy budget. Since material and energy cycles are often intertwined (e.g. the evaporation of water, which transfers matter and latent heat from the Hydrosphere to the Atmosphere), a comprehensive visualization of all interactions within the climate system is infeasible. However, the concept of feedback loops among several climate elements can be visualized schematically. Figure 2.2 shows the interactions of several climate elements in a highly simplified manner and puts the focus of this thesis, the global mineral dust cycle, into the bigger picture in the scope of the whole Climate System:

1. A rising atmospheric CO<sub>2</sub> concentration, e.g. due to natural (volcanoes) or anthropogenic (fossil fuel burning) causes, leads to an increase in the average global temperature. Due to their dipole moment, CO<sub>2</sub> molecules absorb parts of the spectrum of the outgoing long-wave radiation emitted from Earth. The absorbed energy is then either partly thermalized in the Atmosphere or re-emitted towards Earth, which leads to a temperature increase (Wallace and Hobbs, 2006). Due to its fertilizing effects, a higher atmospheric CO<sub>2</sub> concentration also facilitates more vegetation.
2. A increase in the average global temperature leads to a rising sea level due to thermal expansion, a reduced global ice volume due to melting and a stronger hydrologic cycle, because warmer air can hold more water vapor. A higher temperature also facilitates enhanced vegetation.

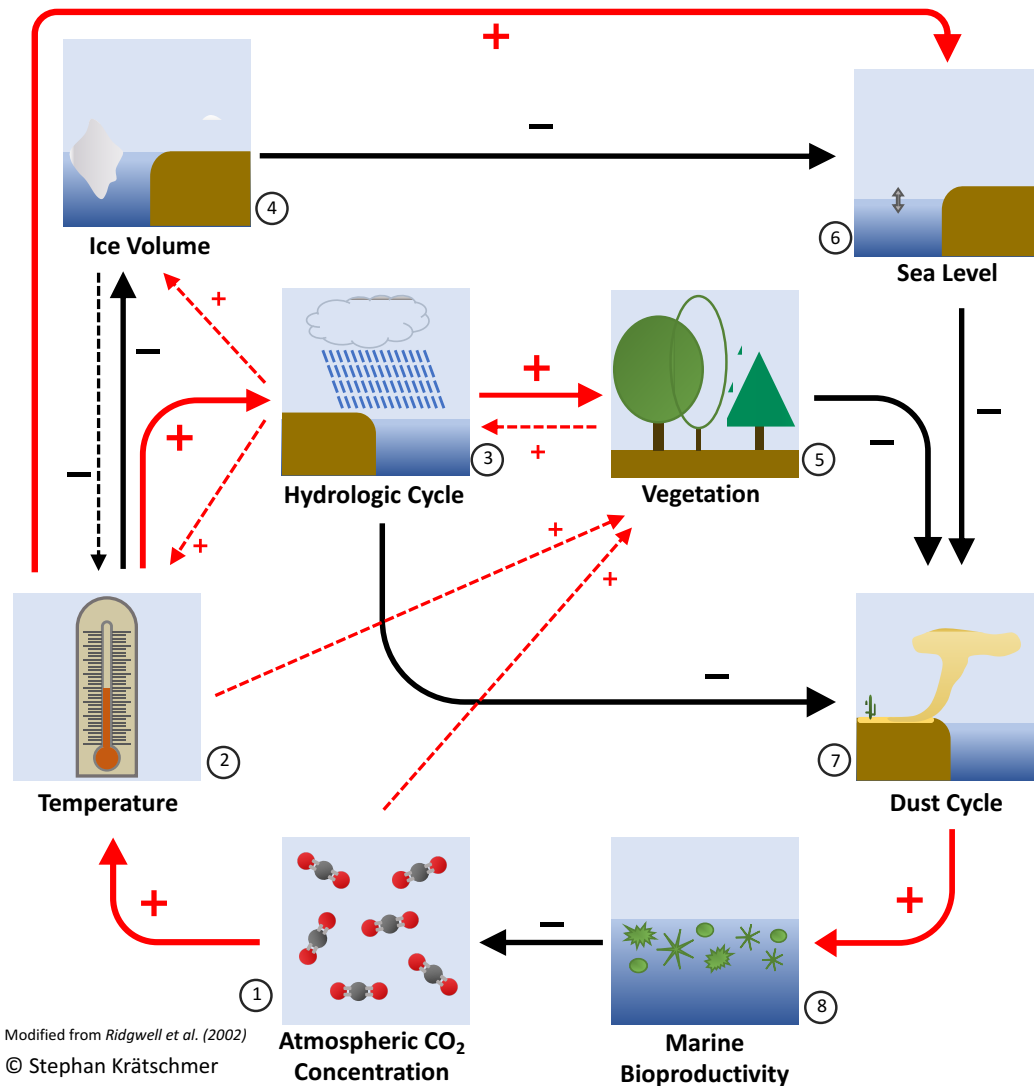


**Figure 2.2.** A highly simplified, schematic illustration of several feedback loops among various important climate elements in the Climate System. It is to be read as: *An increase in X leads to an increase (+) / decrease (-) in Y.* A detailed description following the numbering can be found in the text. [Figure modified from Ridgwell and Watson (2002)]

3. A stronger hydrologic cycle leads to more vegetation and a reduced global dust cycle, since water increases the inter-particle cohesive forces, which in turn leads to lower dust emissions (see section 2.2.2). It also partly leads to an increase in global ice volume, because more water is delivered to high latitudes, and a further increase in atmospheric temperature, because  $H_2O$  is exactly like  $CO_2$  a greenhouse gas and acts accordingly.
4. A increase in global ice volume leads to a reduced sea level, because more water is bound in the Cryosphere. Since a larger surface is then covered by

snow / ice, the Earth's albedo increases and the global temperature decreases as a consequence.

5. Increased vegetation leads to a reduction in global dust emissions, since it reduces the wind speed in the boundary layer (see section 2.2.2). It also leads to a stronger hydrologic cycle due to increased evapotranspiration.
6. A higher sea level leads to a decreased global dust cycle, since dust is also emitted in coastal regions (see chapter 4).
7. A stronger mineral dust cycle leads to increased marine bioproductivity, because mineral dust deposited over the oceans provides bioavailable iron, which is a key element for phytoplankton growth (see section 2.2.3).
8. Finally, increased marine bioproductivity leads to a decrease in the atmospheric CO<sub>2</sub> concentration. Carbon, which is continuously exchanged between the Atmosphere and the Oceans in form of CO<sub>2</sub>, is bound in biological matter. After death, large parts of this matter sinks to the ocean floor, effectively removing CO<sub>2</sub> from the Atmosphere (see section 2.2.3).

Figure 2.2 illustrates schematically the interactions between several climate elements as a response to a change in the atmospheric CO<sub>2</sub> concentration, i.e. in the climate forcing. There are, however, different types of forcings in the Climate System acting on different timescales, which eventually contributes to the Earth's climate variability over time.

### 2.1.3. CLIMATE VARIABILITY & RECENT CLIMATE HISTORY (800,000 YR)

A *climate forcing* is a driver of the Climate System, i.e. a mechanism that puts energy into the system and thus enables it to maintain a state far away from the thermodynamic equilibrium <sup>4</sup>. The entirety of all forcing mechanisms combined with all internal feedback mechanisms (as exemplarily shown in the previous section)

---

<sup>4</sup> Since the Sun is essentially the Earth's sole source of energy and all variations can be traced back eventually to changes in the radiation balance, it is also often referred to as *radiative forcing*. Geothermal contributions, i.e. heat fluxes mostly stemming from radioactive decay in the Earth's core released at the surface, which is estimated to be  $(46 \pm 3) \times 10^{12}$  W (Lay et al., 2008), are much smaller than the  $341 \text{ W m}^{-2} \times 4\pi \times (6.371 \times 10^6 \text{ m})^2 \approx 1.74 \times 10^{17}$  W received from the Sun and can thus be neglected.

over all timescales causes eventually the *Climate Variability*. A common approach is the distinction between *external* and *internal* forcings (Peixoto and Oort, 1992):

### 1. External Climate Forcings

- *Changes in solar output*: The solar irradiance is only  $341 \text{ W m}^{-2}$  on average. Physical processes within the sun lead to a so-called *solar cycle*, which modulates the irradiance by  $\pm 0.5 \text{ W m}^{-2}$  with a periodicity of 11 years. Of negligible importance on timescales below tens of millions of years is the aging of the sun, which leads to an increase in luminosity of around 1% per  $10^8 \text{ yr}$ .
- *Orbital changes*: The Earth's orbit around the Sun is characterized by three parameters, each of them showing long-term variations that eventually influence how much energy the Earth receives from the Sun: The *axial precession* (periodicities 19 kyr and 23 kyr<sup>5</sup>), the *obliquity of the ecliptic* (periodicity 41 kyr) and the *eccentricity of the orbit* (periodicities 100 kyr and 400 kyr) (Loutre, 2003).

### 2. Internal Climate Forcings

- *Atmospheric composition*: All atmospheric gases consisting of molecules with a electric dipole moment, e.g.  $\text{CO}_2$ ,  $\text{CH}_4$ ,  $\text{H}_2\text{O}$  and  $\text{N}_2\text{O}$ , absorb parts of the outgoing terrestrial long-wave radiation (so-called *greenhouse gases*). The energy is then either partly re-emitted towards Earth or thermalized in the Atmosphere, effectively increasing the temperature (Wallace and Hobbs, 2006). Similarly, atmospheric aerosols, for instance from volcanoes, may absorb long-wave radiation (e.g. soot particles) or scatter incoming short-wave radiation back into space (e.g.  $\text{H}_2\text{SO}_4$  droplets) (Boucher, 2015).
- *Changes in (terrestrial) albedo*: As already discussed in section 2.1.1, the albedo determines which share of the incoming solar radiation is scattered back into space by clouds and land surfaces. Consequently, variations in the vegetation, soil composition or the snow / ice cover modulate the amount of energy that is taken up by the Climate System.
- *Changes in plate tectonics*: The location of the continents plays a crucial role in terms of how much incoming energy the Earth absorbs due to

---

<sup>5</sup> The oscillation of the parameter is not specified by just a single frequency. Instead, it is given by the frequencies of two superimposed oscillations (so-called *beat*).

differences between land and sea albedo. Processes like pole wandering and continental drifts take place on timescales ranging from  $10^7$  yr to  $10^9$  yr (Peixoto and Oort, 1992).

Knowing about the timescales of all forcings and feedback mechanisms is particularly important in order to identify the causes of climate signals, i.e. any trends or patterns which can be observed in time series of climate variables. Since near-global observations have only been available for the very recent past on geological timescales (ca. 150 yr (Masson-Delmotte et al., 2013)), their reconstruction is a central topic in the field of paleoclimatology. To this end, so-called *climate archives* are being used, for instance rocks, sediments, ice cores and tree rings. The knowledge about the formation processes of these archives, along with various dating and other analysis methods, allows to retrieve a time series for a climate variable. The covered timespan as well as the temporal resolution depend on the type of archive. Continental coastal and ocean sediments, for instance, cover a timespan up to  $10^8$  yr with a typical temporal resolution ranging from 10 yr to  $10^3$  yr, depending on the sedimentation rate and other disturbances like stirring by marine organisms (Ruddiman, 2013).

*Ice cores*, i.e. ice drilled in glaciers and ice sheets at various locations, have provided detailed insights on the climate variability of the late Quaternary Period. Parts of the water that evaporates in lower latitudes gets transported to the poles, where it deposits in form of snow and annual layers accumulate over time. The weight of subsequent snow layers leads to a continuous compactification of the snow to firn and finally, it recrystallizes into ice, preserving aerosols and atmospheric gases in tiny air bubbles trapped within the ice (Ruddiman, 2013). The pressure onto the ice increases with depth, which in turn leads to a thinning of the annual layers and might render them unrecognizable. Also other physical effects, e.g. internal deformation and sliding along the glacier bed, requires the determination of a thinning function based on a geophysical ice flow model for an accurate dating. If the net snow accumulation rate is known, the layer thinning with depth can finally be calculated (Steig, 2003).

Apart from trace gases and aerosols, the concentrations of different water isotopes are of particular interest. While most of the water molecules are  $\text{H}_2^{16}\text{O}$ , other frequently occurring isotopes are  $\text{H}_2^{18}\text{O}$  and  $\text{HD}^{16}\text{O}$  (with D being Deuterium, i.e.  ${}^2_1\text{H}$ ). The differences in the molecular weight lead to enhanced evaporation of the lighter isotopes from the oceans compared to the heavier isotopes. In warm climates, there is an equilibrium between the evaporation of lighter isotopes and

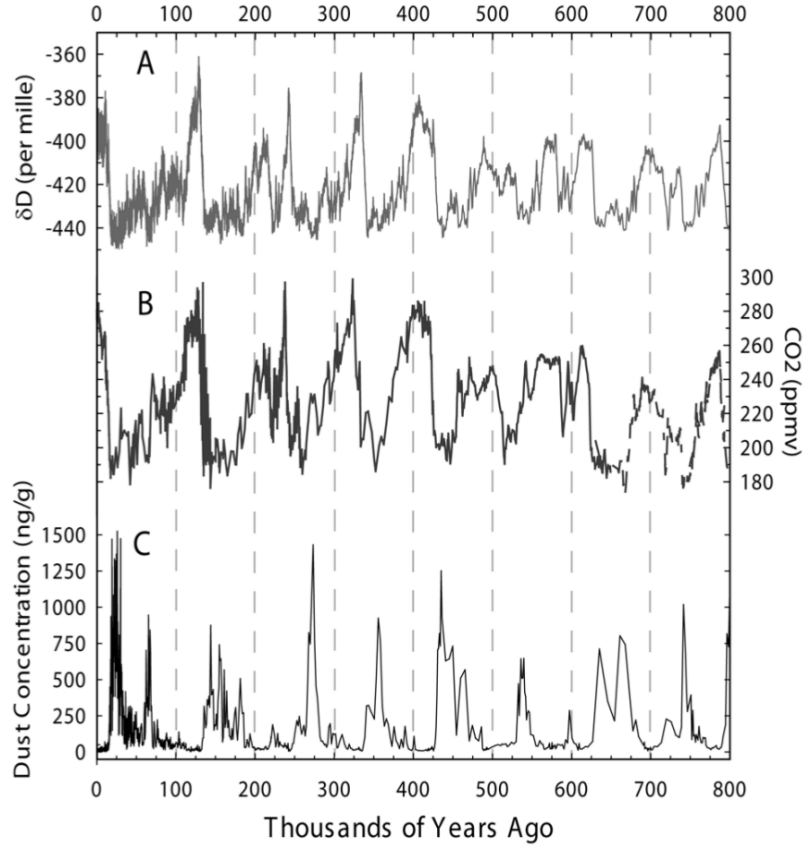


**Figure 2.3.** Time series of  $\delta D$  (a temperature proxy), the atmospheric  $\text{CO}_2$  concentration and the mineral dust concentration retrieved from the EPICA Dome C ice core for the last 800,000 years. A detailed discussion can be found in the text. [Figure taken from Kohfeld and Ridgwell (2009)]

their return into the ocean due to the surface runoff and thus the isotope ratio remains unchanged. However, during cold climates a large amount of the evaporated water is bound in ice sheets, and the isotope ratio in the oceans is increased, respectively, decreased in ice cores. As indicator for the deviation from the standard mean ocean water, the relation

$$\delta(\text{HD}^{16}\text{O}) = \delta D := \left( \frac{\left(\frac{D}{H}\right)_{\text{sample}}}{\left(\frac{D}{H}\right)_{\text{standard}}} - 1 \right) \cdot 1000 \quad (1)$$

has been defined. An empirical (linear) relation, a so-called *transfer function*, can then be used to link the deviation in the isotope concentration to the respective temperature (Steig, 2003; Zhang, 2018).

Applying this technique to ice cores from Greenland and Antarctica has provided climate records over the last 120 kyr and 800 kyr, respectively (Alley and Bender, 1998; Lambert et al., 2008; Wolff et al., 2010). In particular the long records of the Antarctic ice core(s) suggest that the climate exhibited a strong variability, at

least during the covered timespan. The time series for  $\delta D$  retrieved from the EPICA<sup>6</sup> Dome C ice core (75°06'S, 123°21'E) shown in Fig. 2.3 indicates according to Eq. (1), that the temperature oscillated between a warm climate state (low deviation, *interglacial*) and a cold climate state (high deviation, *glacial*) with a periodicity of approximately 100 kyr (time series A). An interglacial was usually followed by a cooling over a period of around 90 kyr until it reached the glacial maximum, just to be followed by a comparably abrupt warming period of around 10 kyr at the end of a glacial-interglacial cycle.

The first interdisciplinary reconstruction of the global climate conditions during one of these glacials, the *Last Glacial Maximum* (LGM, 21 kyr BP), had been done in the 1970s and 1980s in the scope of the project *Climate: Long range Investigation, Mapping and Prediction* (CLIMAP), resulting in global maps of the sea surface temperatures (SST), the extend of continental and sea ice, and the land albedo for modern and LGM climate conditions (McIntyre and Cline, 1981). The most prominent features of the reconstructions are the enormous continental ice sheets during the LGM, covering large parts of North America (Cordilleran ice sheet) and Canada (Laurentide ice sheet) down to 37°N, Scandinavia and Northern Europe (Fennoscandian ice sheet, down to 48°N) as well as the northern margins of Eurasia (Ruddiman, 2013). Initially, the sea level drop due to the water that was bound in the kilometers thick ice sheets was estimated to be in the range of 127 m (CLIMAP min) to 163 m (CLIMAP max), particularly due to uncertainties in the thickness reconstruction of the Laurentide and Fennoscandian ice sheet. More recent projects<sup>7</sup> constrain the sea level decrease to the range between 120 m and 135 m (Clark and Mix, 2002). However, especially the temperature reconstructions remain controversial. The mean global temperature decrease during the LGM had "only" been reconstructed to  $(3.0 \pm 0.6)^\circ\text{C}$  (Hoffert and Covey, 1992), and for parts of the tropics and the Pacific Ocean even a warming in the SSTs (compared to present climate conditions) had been suggested, a feature that could so far neither be explained conceptually nor reproduced by climate models (Yin and Battisti, 2001).

Analyzing the composition of the air trapped in the EPICA Dome C ice core has revealed a striking synchronicity between  $\delta D$  and the atmospheric  $\text{CO}_2$  concentra-

---

<sup>6</sup> *European Project for Ice Coring in Antarctica* (EPICA).

<sup>7</sup> For instance, the program *Environmental Processes of the Ice-Age: Land, Ocean, Glaciers* (EPILOG).

tion <sup>8</sup>, indicating that the temperature was high (low) when the CO<sub>2</sub> level was high (low) (see Fig. 2.3, time series A & B). The obvious correlation between both time series and the knowledge about CO<sub>2</sub> being a greenhouse gas leads naturally to the question whether CO<sub>2</sub> was a driver or "only" an amplifier of the drastic glacial-interglacial climate changes. Milankovitch (1941) suggested that the solar forcing, which is modulated by the superimposed oscillations of three orbital parameters (axial precession, obliquity of the ecliptic and eccentricity of the orbit) was responsible for the observed periodic climate changes over the last 800,000 years. A Fourier analysis of the climate signal reveals indeed peaks at orbital frequencies, and the  $\delta^{18}\text{O}$  signal from the Vostok ice core (78°28'S, 106°48'E) has a strong correlation with the 23 kyr periodicity of the axial precession signal. However, later studies showed that the orbital variations in the irradiance are too small to cause the observed changes in the climate and required amplifying mechanisms, of which at least 50% are attributed to the changes in the atmospheric CO<sub>2</sub> concentration (Steig, 2003).

Another remarkable coherence with the signals of temperature ( $\delta D$ ) and atmospheric CO<sub>2</sub> concentration can be found in the (mineral) dust concentration retrieved from the EPICA Dome C ice core (Fig. 2.3, time series C). The fact that it is antiphased to the other two signals indicates that the dust deposition at the drilling location was high when the temperatures were low, and vice versa. The implications of this observation will be discussed in section 2.2.4 because their understanding requires general background knowledge about the *mineral dust cycle* in the climate system, i.e. the process of dust emission, transport and deposition.

Regardless of whether CO<sub>2</sub> was a driver or an amplifier of the observed climate changes, an equally important question is which sphere contributed to the draw-down from 280 ppm during interglacials to well below 200 ppm during glacials. A first constraint can be made by looking at the according timescales. The inorganic part of the carbon cycle, which describes the process of atmospheric carbon getting bound in form of carbonate rocks, i.e. in the lithosphere, acts too slow to be responsible for substantial changes on glacial-interglacial timescales (Berner et al., 1983). The carbon exchange between atmosphere and (terrestrial) biosphere would take place on relevant timescales. However, studies investigating the amount

---

<sup>8</sup> Since atmospheric gases can be assumed to be well-mixed globally on timescales of one year or longer, the gas composition in the air bubbles trapped in the ice are representative not only locally, but for the whole Earth.

of dissolved inorganic carbon in the oceans and other reconstructions of the vegetation during the LGM suggest rather a considerably reduced global vegetation as a consequence of the lower temperatures and the reduced hydrologic cycle, i.e. the terrestrial biosphere might even have *released* carbon towards the LGM (Shackleton, 1977; Adams and Faure, 1998). This leaves only the hydrosphere and the marine biosphere as potential carbon reservoirs during the LGM, and the discussion on their role during the LGM as well as how both might be intertwined with the mineral dust cycle will be resumed in section 2.2.3.

## 2.2. MINERAL DUST IN THE CLIMATE SYSTEM

### 2.2.1. A BRIEF OVERVIEW ON ATMOSPHERIC AEROSOLS

As mentioned in section 2.1.1, the atmosphere does not only consist of various (trace) gases, but also contains solid and liquid particulate matter suspended in air, so-called aerosols. A common way of categorizing the different aerosol species is to distinguish between *primary* and (*precursors of*) *secondary* aerosols<sup>9</sup>. The following listing based on Boucher (2015) provides an overview on the most abundant aerosol species:

1. **Primary Aerosols**, i.e. aerosols that have been emitted into the atmosphere in form of particles
  - *Marine aerosol* or *sea spray*, which is emitted in form of hydrated sea salt particles, along with impurities like organic matter, when bubbles burst at the sea surface. The particle sizes range from 100 nm up to tens of micrometer, and an estimated 1000 Tg to 6000 Tg are emitted each year.
  - *Mineral aerosol* or *mineral dust*, which is emitted from arid and semi-arid areas. The particle sizes range from 100 nm up to tens of micrometer, and an estimated 1000 Tg to 3000 Tg are emitted each year. More details follow in the next section(s).
  - *Biogenic aerosol*, for instance bacteria, pollen or spores with particle sizes ranging from tens of nanometers to hundreds of micrometers. An esti-

---

<sup>9</sup> An additional common distinction is between *natural* and *anthropogenic* aerosols. However, since anthropogenic aerosols are not of importance in the scope of this thesis, this distinction will not be introduced.

mated amount of 1000 Tg is emitted each year.

- *Biomass burning aerosol*, i.e. burned biological matter that is emitted, for instance, from forest fires in form of organic carbon and black carbon (soot or ash). The annual emissions are estimated to be in the range of 50 Tg to 90 Tg.
- *Volcanic aerosol* or *volcanic ash*, i.e. black carbon.

2. **Secondary Aerosols**, i.e. aerosols whose gaseous precursors have been emitted into the atmosphere and formed particles by gas-phase condensation

- *Dimethylsulphide* (DMS) is a gas that is produced by some phytoplankton species. An estimated amount of 20 Tg to 40 Tg S is released each year from the sea into the atmosphere, where it is then oxidized and forms sulphate aerosols by condensation.
- *Volcanic SO<sub>2</sub>* also forms sulphate aerosols after oxidization; an estimated amount of 6 Tg to 20 Tg S is emitted each year.
- *Terpenes*, i.e. volatile organic compounds which form aerosols after oxidization; an estimated amount of 40 Tg to 400 Tg are emitted each year from the biosphere.

The overview shows clearly that the particle sizes of aerosols vary over several orders of magnitude, ranging from a few nanometers up to hundreds of micrometers. An idealized, typical particle size distribution of atmospheric aerosols is shown in Fig. 2.4, exhibiting four distinctive modes as a result of the underlying physical and chemical formation processes. Aerosol particles in the *nucleation mode* are formed by gas-phase condensation of secondary aerosol precursors. Due to further gas and water vapor condensation, they grow into the *nuclei* or *aitken mode*. Further growth is then caused by coagulation and coalescence, and an equilibrium between sources (growth processes) and sinks (evaporation, sublimation & deposition mechanisms) is reached in the *accumulation modes*. Several primary aerosols, e.g. mineral dust, are directly emitted either into the accumulation or *coarse mode*. They can also grow in size by sulfate condensation on the particle surfaces ("aerosol aging"), a process that increases the water solubility and facilitates coagulation (Heintzenberg, 2003; Boucher, 2015).

Mathematically, a mode can be described by a particle number concentration  $N(D)$  in  $\text{m}^{-3}$  and a particle number density function  $n(D)$ , such that

$$n(D) = \frac{dN(D)}{dD} \quad (2)$$

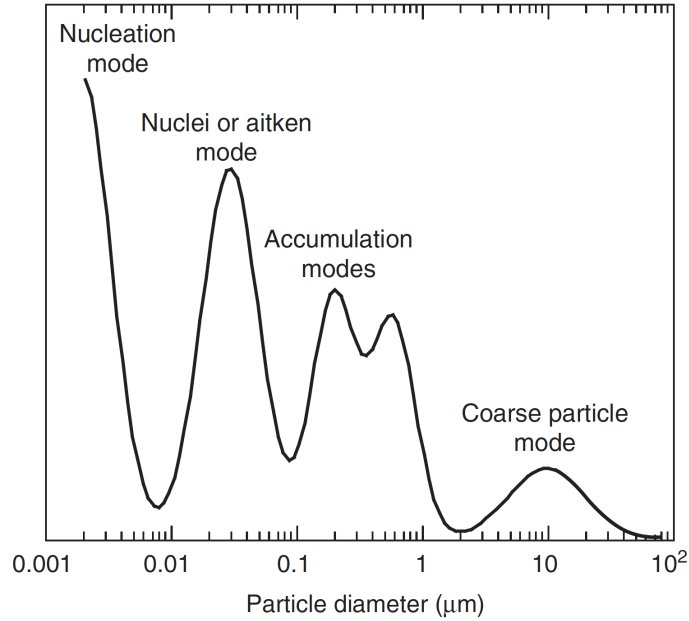


**Figure 2.4.** Idealized particle size distribution of atmospheric aerosols. The particle diameter is plotted on a logarithmic scale due to the huge span they cover, and the vertical axis could represent a particle number density. The four modes are a consequence of different aerosol formation processes, see text for details. [Figure taken from McMurry (2003)]

with the particle diameter  $D$ . The  $k^{\text{th}}$ -order moment of this distribution is then given by <sup>10</sup>

$$m_k = \int_0^{\infty} D^k n(D) dD. \quad (3)$$

However, this still requires the definition of a particle number density function  $n(D)$ . A common choice is a so-called lognormal distribution

$$n(\ln(D)) = \frac{dN(D)}{d(\ln(D))} := \frac{N_0}{\sqrt{2\pi \ln(\sigma)}} \exp\left(-\frac{(\ln(D) - \ln(\bar{D}))^2}{2 \ln(\sigma)^2}\right), \quad (4)$$

which is defined by the *total particle number concentration*  $N_0$ , the *standard deviation*  $\sigma$  and the *number median diameter*  $\bar{D}$ . Apart from the fact that this function is defined by only three parameters, other "conveniences" are that the function is not defined for negative particle diameter and that the moments of the distribution also follow lognormal laws. In general, however, this function cannot be derived from underlying physical principles (Heintzenberg, 2003). An easier readability ac-

<sup>10</sup> Note that the lower integration bound is 0 instead of  $-\infty$  because particle diameter can only have positive values.

According to Eq. (2) is obtained by the transform

$$n(D) = \frac{dN(D)}{d(\ln(D))} \frac{d(\ln(D))}{dD} = \frac{N_0}{\sqrt{2\pi}D \ln(\sigma)} \exp\left(-\frac{(\ln(D) - \ln(\bar{D}))^2}{2 \ln(\sigma)^2}\right). \quad (5)$$

Under the assumption of spherical particles with a constant mass density  $\rho$ , the total mass  $M_0$  contained in the mode is then given by the third-order moment of the distribution:

$$M_0 = \frac{\pi}{6} \rho \int_0^\infty D^3 n(D) dD = \frac{\pi}{6} \rho N_0 \bar{D}^3 \exp\left(\frac{9 \ln(\sigma)^2}{2}\right). \quad (6)$$

Equation (6) shows that, aside from the two predefined parameters of the lognormal distribution  $\sigma$  and  $\bar{D}$ , only the total particle number concentration  $N_0$  is required in order to compute the total mass  $M_0$ , and vice versa. In order to describe a multimodal distribution as shown in Fig. 2.4, several unimodal distribution functions can be superimposed. Both aspects will be of importance in section 3.1.2. In the next section, the focus will be on the various physical processes taking place in the scope of the mineral dust cycle.

### 2.2.2. PHYSICAL PROCESSES IN THE MINERAL DUST CYCLE

*Mineral dust* is the final product of weathering, i.e. the process of dissolving and breaking down rocks contained in the soil, e.g. quartz ( $\text{SiO}_2$ ), feldspar ( $\text{KAlSi}_3\text{O}_8$ ), calcite ( $\text{CaCO}_3$ ) and other minerals (Shao, 2008). Wind tunnel experiments showed that also the mechanical abrasion due to dust-loaded winds contributes to the production of mineral dust (Dietrich, 1977). As already addressed in the previous section, the particle size distribution extends over several orders of magnitude. A soil classification system of intermediate detail is, for instance, provided by the U.S. Department of Agriculture (USDA) (e.g. García-Gaines and Frankenstein (2015)) and illustrated in Fig. 2.5a. Here, particles are at first roughly divided into four different categories according to their grain size (diameter  $D$ ): *clay* ( $D < 0.002$  mm), *silt* ( $0.002$  mm  $< D < 0.05$  mm), *sand* ( $0.05$  mm  $< D < 2$  mm) and *gravel* ( $D > 2$  mm). The sand fraction is then further divided into five groups, ranging from *very fine* to *very coarse*. According to Shao et al. (2011), the term *mineral dust cycle* refers to all formation, emission, transport, transformation, deposition and biogeochemical processes of mineral dust. In the scope of this thesis, however, a particular focus will be put on the atmospheric processes like dust emission, transport and deposition.

Wind tunnel experiments have further shown that once a threshold wind velocity

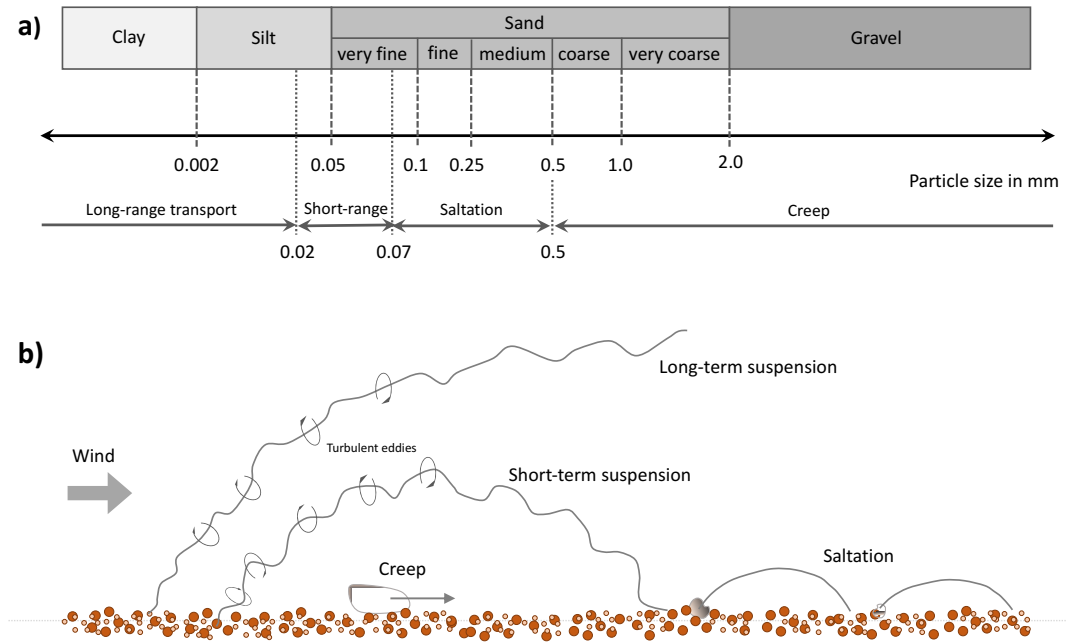


**Figure 2.5.** Soil classification system based on the particle sizes according to the U.S. Department of Agriculture (e.g. García-Gaines and Frankenstein (2015)) (a). The grain size influences the mobilization and transport properties of the particles, ranging from wind-induced creeping and jumping (saltation) of larger particles to short and long-term suspension and transport of smaller particles (a, b). [Figures modified from Shao (2008)]

in the laminar layer of the boundary layer over a flat deposit is exceeded, dust emission occurs due to momentum transfer from the air to the soil particles (Fletcher, 1976), or put more simply, atmospheric mineral dust particles "have their aeolian origin in the eroded crustal surface of the Earth" (Heintzenberg, 2003). The results also suggest that a minimum threshold friction velocity of around  $20 \text{ cm s}^{-1}$  is necessary for particle sizes between  $80 \mu\text{m}$  and  $100 \mu\text{m}$ <sup>11</sup> (Laurent et al., 2009). Larger particles require a higher momentum due to their higher mass, and for smaller particles the cohesive inter-particle forces lead to a strong bond between dust particles. For gravel and the larger fractions of sand, the wind friction is usually just enough to cause a temporary horizontal movement, so-called *creeping* (see Fig. 2.5). Smaller sand particles can exhibit a short, jumping movement on a ballistic trajectory, the so-called *saltation*. The impact of saltating grains might break other particles into smaller pieces. Only clay, silt and the finest sand particles are small enough in order to be lifted by turbulent eddies in the boundary layer,

<sup>11</sup> Only for *dry* soils and without any other surface elements.

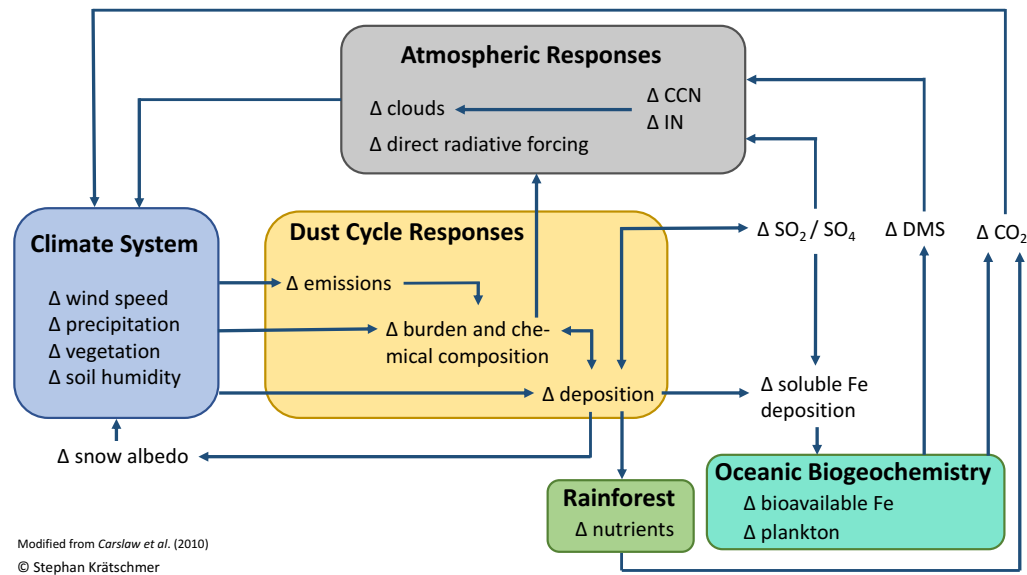


**Figure 2.6.** Aeolian mineral dust influences many processes in the atmosphere, for instance cloud formation and the radiative forcing, and also affects terrestrial and marine ecosystems. The feedbacks on the climate system affect in turn processes like dust emission, transport and deposition, see text for details. [Figure modified from Carslaw et al. (2010)]

and the time they remain suspended generally increases with decreasing particle size (Shao, 2008). This shows also clearly why the estimated amount of annual dust emissions covers such a huge span for present day climate conditions, ranging from 1000 Mt up to 3000 Mt (Gras, 2003; Boucher, 2015) and even as much as 5000 Mt (Shao et al., 2011), because it depends strongly on the upper particle size limit: Large particles contribute substantially to the emitted mass budget, however, they remain only for a very short time in the atmosphere and might even fall out immediately after emission.

The majority of mineral dust is emitted from arid and semi-arid areas, particularly deserts. Consequently, the main dust source regions in the northern hemisphere are located in North Africa, the Middle East and Asia, with minor contributions from the Great Basin in North America. In the Southern Hemisphere (SH), the main dust source regions are located in southern South America (Patagonia), southern Africa and Australia. Marine sediment data indicate that New Zealand also represented a dust source during the LGM (Trudgill et al., 2020).

The wind velocity in the laminar boundary layer, and thus the dust emission, is controlled by several factors. In general, all kinds of non-erodible surface elements like rocks, larger stones, pebbles and any type of vegetation leads to a reduction

of the wind velocity in the laminar boundary layer due to momentum dissipation. Another factor increasing the required threshold wind friction velocity is the soil wetness, because water increases the cohesive forces between particles (Laurent et al., 2009), see Fig. 2.6. Once suspended, the dust particles are transported and distributed by large-scale advection and convection of the atmospheric circulation, which leads globally to a strongly heterogeneous *dust burden* in  $\text{kg m}^{-2}$  with substantially higher dust concentrations above the source areas and along atmospheric transport pathways. Since the atmospheric circulation is characterized by geostrophic winds on a synoptic scale and above, which leads predominantly to a zonal transport of dust, the meridional transport is mainly caused by eddies (Li et al., 2010).

During transport, the dust particles directly influence Earth’s radiation budget by scattering and absorbing shortwave and longwave radiation depending on particle size and mineralogical composition (Dufresne et al., 2002; Balkanski et al., 2007), which in turn affects the atmospheric stability by altering the vertical temperature profile and relative humidity (Boucher, 2015). Besides these direct effects on the energy budget, mineral dust particles act as cloud condensation and ice nuclei and thus affect optical and other microphysical properties of clouds, which again influences the radiation budget (Spracklen et al., 2008).<sup>12</sup>

At some point dust particles are removed from the atmosphere due to deposition. The predominant deposition mechanisms close to the ground, for instance in the source regions, are passive gravitational settling (*sedimentation*) as well as molecular and turbulent diffusion fluxes. All previously mentioned mechanisms are usually summarized by the term *dry deposition*. Typical dry deposition velocities for comparably large atmospheric mineral dust particles in the size range from  $1\ \mu\text{m}$  to  $5\ \mu\text{m}$  are between  $0.01\ \text{m s}^{-1}$  and  $0.05\ \text{m s}^{-1}$ , and for finer particles between  $0.003\ \text{m s}^{-1}$  and  $0.03\ \text{m s}^{-1}$  (Duce et al., 1991). Alternatively, particles are removed by *wet deposition* (i.e. precipitation), either because they serve as cloud condensation nuclei and are incorporated in raindrops (in-cloud scavenging), or less efficiently, they are hit and removed by falling raindrops (below-cloud scavenging) (Boucher, 2015).

Depending on the mineralogical composition of the dust particles, they may constitute a very important source of micronutrients for some ecosystems. By acting as a fertilizer for the vegetation and the biosphere in general, mineral dust also

---

<sup>12</sup> This paragraph has been quoted verbatim from Krättschmer et al. (2022).

plays a crucial role in the carbon cycle and its impact on the global climate. Saharan dust, for instance, has been identified to represent an important source of phosphorus for the Amazon rainforest, where the soil shows a general depletion (Reichholf, 1986).<sup>13</sup>

In the next section, a focus will be put on another ecosystem depending on the fertilizing effects of mineral dust: the *Southern Ocean* (SO).

### 2.2.3. THE IRON HYPOTHESIS

The substantial atmospheric CO<sub>2</sub> reduction from 280 ppm during interglacials to well below 200 ppm during glacial maxima indicated by time series data retrieved from Antarctic ice cores (see Fig. 2.3, time series B) is thought to be either a cause or at least an amplifier of the observed climate change in terms of atmospheric temperature (Fig. 2.3, time series A). As discussed in Sec. 2.1.3, a consideration of the according timescales suggests that the ocean played a major role during those transitions. In the late 1980s, several iron (Fe) fertilization experiments were performed in remote surface waters of the Antarctic and Pacific subarctic Oceans (Martin and Fitzwater, 1988; Martin et al., 1990). This region is enriched in major plant nutrients like nitrate (NO<sub>3</sub>) and phosphate (PO<sub>4</sub>), however, without showing the expected phytoplankton blooms, a circumstance due to which the SO is referred to as the largest high nutrient-low chlorophyll (HNLC) region in the world (Pitchford, 1999; Martínez-García et al., 2014). The results of these experiments showed that the available nutrients were used up whenever Fe was added to the water and the amount of build up phytoplankton increased proportionally to the amount of added iron, leading the authors to the conclusion that iron deficiency is the limiting factor for phytoplankton growth in the SO.

Based on the results of those studies, Martin (1990) proposed the so-called *Iron Hypothesis* (see Fig. 2.7), which states that increased mineral dust deposition onto the SO during cold periods provided large amounts of bioavailable iron, which in turn caused phytoplankton blooms binding vast amounts of carbon (which was formerly bound in CO<sub>2</sub> dissolved in ocean water due to atmosphere-ocean gas exchange). After death, large parts of the organic matter sunk down to the ocean floor, effectively removing carbon from the atmosphere and thus contributing to the

---

<sup>13</sup> This paragraph has been quoted verbatim from Krätschmer et al. (2022).

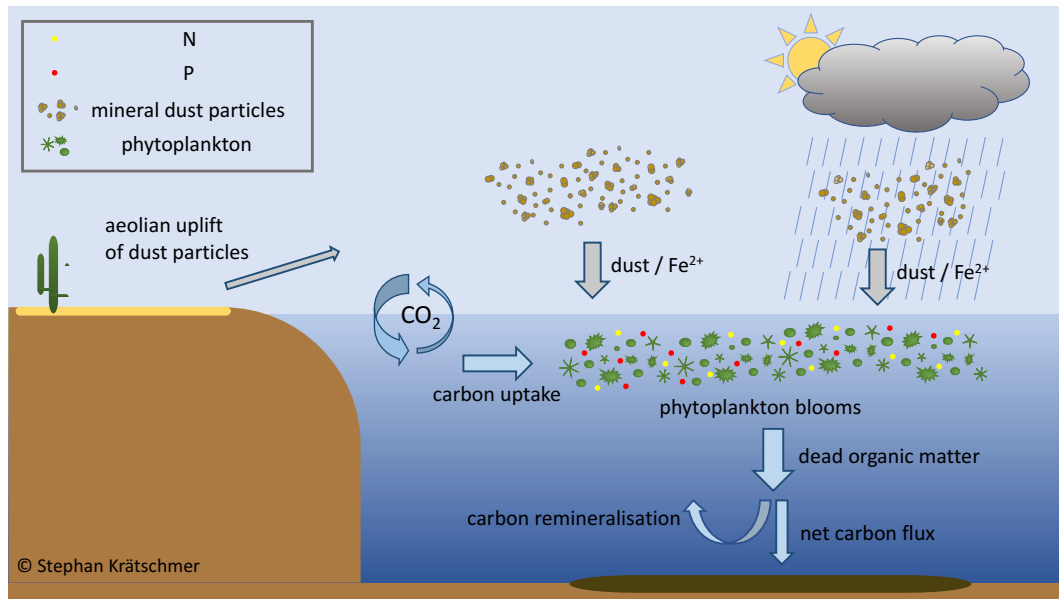


**Figure 2.7.** A simplified, schematic illustration of the *Iron Hypothesis* (Martin, 1990): Increased mineral dust fluxes during cold periods delivered large amounts of bioavailable iron ( $\text{Fe}^{2+}$ ) to the SO, a region that is enriched in plant nutrients like nitrate and phosphate. The resulting phytoplankton blooms bound vast amounts of carbon. After death, large parts of the organic matter sunk down to the ocean floor, effectively removing carbon from the atmosphere and thus contributing to the observed atmospheric  $\text{CO}_2$  reduction.

observed reduction in atmospheric  $\text{CO}_2$  concentration. Paleoceanographic data indicate that increased aeolian dust fluxes were only observed once the atmospheric  $\text{CO}_2$  concentration had already decreased by 40 to 50 ppm, and consequently, the upper limit of this effect has been constrained to 40 ppm (Martínez-García et al., 2011).

Ice core data from Antarctica suggest indeed regionally a  $\sim 25$ -fold dust deposition flux raise during the LGM (Lambert et al., 2008), and the globally-averaged increase in atmospheric dust load is estimated based on data to be around 2- to 5-fold (Kohfeld and Harrison, 2001). Additionally, marine sediment data from the Pacific SO indicate that the dust deposition flux here was likewise enhanced by a factor of two to three during glacials (Lamy et al., 2014). However, dust itself is just the carrier of the key nutrient Fe required for phytoplankton growth, and the main question is how much iron had been delivered to the glacial SO, a region that has been suggested to be primarily responsible for the observed atmospheric glacial-interglacial  $\text{CO}_2$  changes (Schmittner and Galbraith, 2008). Although strongly regionally varying, the globally-averaged iron content in the Earth's crust is 3.5% (Shao et al., 2011). Phytoplankton requires a form of soluble (i.e. bioavailable) iron,

and the according oxidation state  $\text{Fe}^{2+}$ , respectively, Fe(II) only makes up 0.5 % of the total iron content in soil (Hand et al., 2004). Additionally, when dissolved in water, Fe(II) is oxidized to the rather insoluble form Fe(III) within a few seconds to hours (Sarmiento and Gruber, 2006). However, several biochemical and photochemical reactions which reduce Fe(III) to its bioavailable form Fe(II) have been proposed, either taking place during atmospheric transport (e.g. in clouds) (Zhuang et al., 1992) or when already dissolved in seawater (Rue and Bruland, 1997). Marine sediment core analysis showed that the iron flux to the subantarctic regions of the Pacific increased proportionally to the dust deposition by a factor of 3 to 5, but the fraction of bioavailable Fe(II) might actually have been increased by a factor of 15 to 20 during glacial periods compared to present day (Shoenfelt et al., 2018). However, the sediment analysis also suggests that increased iron fertilization in the SO during the LGM was regionally strongly heterogeneous, and some regions like the subantarctic Pacific showed no or only a 2 to 3-fold increase in bioproductivity (Lamy et al., 2014; Trudgill et al., 2020). This leads to the idea that the estimated 40 ppm concentration reduction in atmospheric  $\text{CO}_2$  due to iron fertilization towards the LGM is too high, and other processes might have played a (even more important) role.

In order to investigate the iron hypothesis properly by a modelling approach, the atmospheric modelling needs to represent correctly ...

- the strength of individual dust sources and transport pathways,
- the particle size distribution, because it affects transport and chemical properties,
- the atmospheric particle lifetime, because it affects aerosol aging and the transport range,
- and the spatially-varying deposition.

Based on the dust deposition fields, the biogeochemical modelling then needs to adequately represent the spatially-varying abundance of various forms of iron (free or ligand-bound) and other nutrients, chemical reactions, transport by advection and the iron uptake and utilization by biological matter as well as other factors necessary for metabolism, for instance light availability.

#### 2.2.4. MINERAL DUST AS CLIMATE PROXY

The many factors involved in controlling the processes of mineral dust emission, transport and deposition (see sec. 2.2.2) enable the utilization of mineral dust records, e.g. ice cores, deep sea sediments or loess, as climate proxies (Shao et al., 2011). These records contain informations on the temporal variation of grain sizes, isotopic composition and mass fluxes of dust deposited in the past. For instance, the increased dust deposition during glacials found in ice cores from Greenland, along with larger grain sizes, might have been caused by stronger winds in the source regions (Steffensen, 1997). The characteristic ratios of strontium and neodymium isotopes in dust retrieved from Antarctic ice cores suggest southern South America as the predominant source of dust deposited during the LGM (Basile et al., 1997; Delmonte et al., 2008), and the 2- to 5-fold globally-averaged dust load increase during the LGM suggested by observational data (Kohfeld and Harrison, 2001) is being interpreted as a consequence of the generally drier climate, extended source regions, reduced vegetation and increased near-surface wind speeds (Lunt and Valdes, 2002), i.e. mineral dust records allow for conclusions on the climatic conditions in the source regions.

However, the interpretation of the data provided by dust records is not always unambiguous. The coarser dust particles found in Greenland ice cores delivered during glacials, for instance, could also have been caused by a dust source in closer geographic proximity to the deposition region, which is not active in warmer climates (Steffensen, 1997; Mahowald et al., 2014). Identifying the dust provenance has also turned out to be challenging because the characteristic isotope ratio of dust contained in Antarctic ice cores does not only match the ratio of southern South American soil samples, but also the ratio that has been found in soil samples from central and southeastern Australia (De Deckker et al., 2010). The 25-fold increase in dust deposition in some regions in Antarctica during the LGM (Lambert et al., 2008) could either be caused by

- a substantial source strength increase due to climatic changes in those regions,
- *or* a higher meridional transport efficiency due to reduced precipitation,
- *or* a change in the atmospheric circulation patterns resulting in shorter transport pathways,
- *or* by changes in local atmospheric conditions and deposition patterns,

or a combination of all aforementioned factors (Delmonte et al., 2004; Kohfeld and Ridgwell, 2009; Wolff et al., 2010). In order to get further insights on the matter, climate models provide, in combination with observational data to verify the simulation results, a very useful tool.



"However, what is cause and what effect, only the future will unveil."

---

(Alfred Wegener, *The Origin of Continents and Oceans*)

## 3. MODEL AND METHODS

**Summary.** The aerosol-climate model ECHAM6.3-HAM2.3 is the latest release of a state-of-the-art atmospheric general circulation model. It utilizes a mixed spectral transform / finite differences approach to solve the primitive equations for the variables vorticity, divergence, temperature, logarithmic surface pressure and geopotential. The model includes parameterizations for various subgrid scale processes, including vertical mixing, gravity waves, cloudiness and radiative transfer. The included land surface and vegetation model allows for the representation of dynamic vegetation, considering several plant functional types as well as various types of bare soil. The aerosol submodel calculates explicitly particle number concentrations of the five aerosol species sulfate, black and organic carbon, mineral dust and sea spray. It represents the particle sizes by superimposed log-normal distributions and accounts for inter- and intramodal particle interactions, radiative effects and cloud interactions. Mineral dust emissions are fully coupled to the vegetation model and depend on several meteorological and topographic factors.

### 3.1. ECHAM6.3-HAM2.3

The model used to perform simulations in the scope of this thesis consists of the atmospheric general circulation model ECHAM6.3 coupled to the aerosol model HAM2.3. It is developed by a consortium composed of the ETH Zurich, the Max Planck Institute for Meteorology in Hamburg, the Forschungszentrum Jülich, the University of Oxford, the Finnish Meteorological Institute and the Leibniz Institute for Tropospheric Research. The full model version also includes the model of atmospheric chemistry MOZ1.0 (ECHAM6-HAMMOZ; Schultz et al. (2018)). However, MOZ1.0 has been switched off in all simulations and is therefore not of further importance in the scope of this thesis and has simply been mentioned for the sake of completeness. The ECHAM6-HAMMOZ model code, including all required input files to run simulations, is being hosted by the Center for Climate Systems Modeling (C2SM) at the ETH Zurich and is accessible at <https://redmine.hammoz.ethz.ch> after signing a license agreement. A detailed evaluation of the ECHAM6.3-HAM2.3 model performance for present-day climate can be found in Tegen et al. (2019) and

Neubauer et al. (2019).

### 3.1.1. ATMOSPHERIC GENERAL CIRCULATION MODEL ECHAM6.3

ECHAM6 (subversion 6.3.02) is the latest release of an atmospheric general circulation model. It was branched in the late 1980s from a model developed at the European Center for Medium Range Weather Forecasts (ECMWF) and has since been further developed by the Max Planck Institute for Meteorology in Hamburg. The model can be divided into two parts: The *adiabatic core*, which solves the primitive equations via a spectral method for horizontal differences and a finite-differences scheme on a Lorenz grid in the vertical up to a model top of 0.01 hPa ( $\approx 80$  km), and a set of parameterizations for physical processes on a sub-grid scale. The implemented model equations are (Giorgetta et al., 2013):

$$\frac{d\mathbf{v}_h}{dt} = -\frac{1}{\rho}\nabla_h p - 2(\boldsymbol{\Omega} \times \mathbf{v}_h) - \frac{1}{\rho}\frac{\partial J_{\mathbf{v}_h}}{\partial z} + K_{\mathbf{v}_h} \quad (7a)$$

$$\frac{\partial p}{\partial z} = -g\rho \quad (7b)$$

$$\frac{dT}{dt} = \frac{R_d T_v}{\rho C_p} \frac{dp}{dt} - \frac{1}{C_p} \left( Q_R + Q_L + Q_D - \frac{1}{\rho} \left[ \frac{\partial J_s}{\partial z} - C_{pd} T (\delta - 1) \frac{\partial J_{q_v}}{\partial z} \right] \right) + K_T \quad (7c)$$

$$p = \rho R_d T_v \quad (7d)$$

$$\frac{dq_i}{dt} = S_{q_i} - \frac{1}{\rho} \frac{\partial J_{q_i}}{\partial z} \quad (7e)$$

with the *total* or *advective* derivative

$$\frac{d}{dt} = \frac{\partial}{\partial t} + \mathbf{v}_h \cdot \nabla_h. \quad (8)$$

Equation (7a) expresses the horizontal momentum conservation in a co-rotating reference system. The right-handed side (RHS) of eq. (7a) contains sources and sinks for horizontal linear momentum, such as pressure gradients ( $\nabla_h p$ ), the Coriolis force ( $\boldsymbol{\Omega} \times \mathbf{v}_h$ ), the parameterized vertical flux of horizontal momentum ( $\partial_z J_{\mathbf{v}_h}$ ) and a scale-selective diffusion term ( $K_{\mathbf{v}_h}$ ). Since the vertical height of the atmosphere is much smaller than the horizontal extend, the model is assumed to be in hydrostatic equilibrium (eq. (7b)) (Stocker, 2011). The energy conservation equation (7c) is based on the first law of thermodynamics. Changes in internal energy ( $d_t T$ ) are caused by adiabatic processes ( $d_t p$ ) and several parameterized diabatic processes, including heating due to radiation ( $Q_R$ ), phase transitions ( $Q_L$ ), dissipation ( $Q_D$ ), vertical fluxes of dry static energy ( $\partial_z J_s$ ) and water vapour ( $\partial_z J_{q_v}$ ) and other sub-grid scale processes ( $K_T$ ). The equation of state (7d) puts pressure in relation to temperature. The set of equations is closed by mass conservation

equations (7e) for dry air, water vapour, liquid water and ice, each denoted by the subscript  $i$ . Changes in the specific mass of each component ( $d_i q_i$ ) are caused by phase transitions, respectively, precipitation formation ( $S_{q_i}$ ) and vertical fluxes of moisture and cloud species ( $\partial_z J_{q_i}$ ).

In order to be able to apply the spectral transform method to represent horizontal differences, the divergence ( $\nabla \cdot$ ) and curl ( $\nabla \times$ ) operator are applied to eq. (7a) (Bourke, 1972; Simmons et al., 1989). The spectral method is then applied to the variables vorticity, divergence, temperature, logarithmic surface pressure and surface geopotential. Taking advantage of the Earth's spherical symmetry, each variable  $X$  (depending on azimuth, polar angle, a general pressure-based terrain-following vertical coordinate and the time  $(\lambda, \mu, \eta, t)$ ) is expressed by a truncated series of spherical harmonics, i.e. eigenfunctions of the Laplace operator in spherical coordinates:

$$X(\lambda, \mu, \eta, t) = \sum_{m=-M}^M \sum_{n=m}^{N(M)} X_n^m(\eta, t) P_n^m(\mu) e^{im\lambda}, \quad (9)$$

with a height- and time-dependent factor  $X_n^m(\eta, t)$  and the Associated Legendre Functions of the first kind  $P_n^m(\mu)$ . In ECHAM6, a *triangular* truncation scheme with typically  $M = 63$  wavenumbers is used, usually denoted as T63. The highest wavenumber determines the spatial resolution (Stocker, 2011), and T63 corresponds to a horizontal resolution of  $1.875^\circ \times 1.875^\circ$ . In the vertical, the model is typically discretized by 47 model layers, denoted as L47. The numerical methods to solve the governing equations are conservative in terms of specific quantities, for instance kinetic and potential energy during vertical advection and angular momentum for calculating pressure gradients (Simmons and Jiabin, 1991). Tracer transport is calculated based on a inherently conservative flux-form semi-Lagrangian scheme on a Gaussian grid introduced by Lin and Rood (1996).

The suite of parameterizations for diabatic sub-grid scale processes includes approximations for the following processes (Stevens et al., 2013):

- *Vertical mixing*: Vertical mixing occurs due to turbulent motions in the boundary layer and the free atmosphere as well as convection. The boundary layer and turbulence are parameterized based on an eddy diffusivity, respectively, viscosity approach (Brinkop and Roeckner, 1995). The model accounts for shallow, midlevel and deep convection using the mass-flux framework by Tiedtke (1989). However, only one type of convection per grid cell is allowed, with a preference for deep convection.
- *Gravity waves*: The transport of momentum in form of gravity waves caused

by boundary effects is calculated following a scheme by Palmer et al. (1986) and Miller et al. (1989), taking effects of the sub-grid orography into account, for instance blocking (Lott, 1999; Baines and Palmer, 1990).

- *Stratiform clouds*: The subgrid scale cloud fraction is parameterized based on the relative humidity once a specific threshold value is exceeded (Sundqvist et al., 1989). Transport of cloud water and ice is prognostically calculated, accounting for adiabatic circulations, phase transitions, and the conversion to large-scale precipitation (Lohmann and Roeckner, 1996). The coupling to the aerosol model HAM2.3 enables an explicit calculation of several microphysical processes in clouds, e.g. aerosol activation.
- *Radiative transfer*: Radiative transfer is parameterized by dividing the relevant part of the electromagnetic spectrum into 14 shortwave and 16 long-wave bands, and absorption is calculated over all bands depending on trace gas concentrations and ambient pressure using look-up tables. The optical properties of clouds for each band are calculated based on Mie theory.
- *Land surface and vegetation*: ECHAM6 also contains a comprehensive sub-model for the land surface and vegetation called JSBACH (Reick et al., 2013). Therein, each grid cell is assumed to be tiled allowing various shares of bare soil and 12 different plant functional types, whereas the soil hydrology is represented by a five-layer scheme (Hagemann and Stacke, 2015). The sub-model allows for the calculation of dynamic vegetation and provides physical parameters like evaporation and surface albedo.

### 3.1.2. AEROSOL MODEL HAM2.3

HAM2.3 constitutes a comprehensive microphysics package for the five aerosol species sulfate, black and organic carbon, sea spray and mineral dust. Similar to ECHAM6.3, it can also be roughly split up into two parts, with one mainly treating large-scale processes like emission, transport, and deposition of aerosol particles, while the other deals with the microphysical processes, such as nucleation, condensation, coagulation, and hydration. For the latter, the default sub-model in HAM2.3 is the modal M7 aerosol model (Vignati et al., 2004), which represents the particle size distribution via seven superimposed log-normal modes (see sec. 2.2.1):

$$n(\ln(r)) = \sum_{i=1}^7 \frac{N_i}{\sqrt{2\pi} \ln(\sigma_i)} \exp \left\{ -\frac{(\ln(r) - \ln(\bar{r}_i))^2}{2 \ln^2(\sigma_i)} \right\} \quad (10)$$

The seven log-normal modes in M7 consist of four soluble and three insoluble modes, representing the nucleation mode (number median radius  $\bar{r} < 5$  nm, only soluble mode), Aitken mode ( $5 \text{ nm} < \bar{r} < 50$  nm), accumulation mode ( $50 \text{ nm} < \bar{r} < 500$  nm), and coarse mode ( $\bar{r} > 500$  nm). Hereby, the soluble modes are assumed to be perfectly internally mixed. Each mode is mathematically defined by three moments of the distribution, namely the aerosol number concentration  $N_0$ , the number median radius  $\bar{r}$ , and the standard deviation  $\sigma$ . The latter is set to  $\sigma = 1.59$  for the nucleation, Aitken, and accumulation modes and  $\sigma = 2.00$  for the coarse modes (Wilson et al., 2001; Stier et al., 2005).

In each time step, HAM2.3 calculates the transport of the tracer aerosol mass and aerosol number. As shown by eq. (6), the number median radius  $\bar{r}$  can be determined for each mode and grid cell based on the given information. Each mode is consequently confined by the boundaries given above, though the number median radius changes over time due to various processes transferring particles between modes, respectively, removing or adding particles from or to modes. All further size-dependent processes are calculated based on this number median radius for all particles of a specific mode. Aerosol particles devolve from insoluble to soluble modes either due to condensation of sulfate on their surface or due to coagulation with particles of soluble modes. The aerosol dynamics, i.e. temporal changes in particle number concentration per mode, is based on a general coagulation equation (Smoluchowski, 1918; Stier et al., 2005). For the soluble modes, the equation reads

$$\frac{dN_i}{dt} = -\frac{1}{2}K_{ii}N_i^2 - N_i \left[ \sum_{j=i+1}^{ns} K_{ij}N_j + \sum_{j=i+ns}^{ns+ni} K_{ij}N_j \right] + \delta_{i1}c. \quad (11)$$

The terms on the RHS represent sinks, like intramodal and intermodal coagulation, and sources, i.e. nucleation, with the coagulation kernel  $K$  containing the coagulation coefficients, the Kronecker delta  $\delta$  and the nucleation rate  $c$ . For particles in the insoluble modes, intermodal coagulation with insoluble particles is considered too inefficient, and eq. (11) simplifies to

$$\frac{dN_i}{dt} = -\frac{1}{2}K_{ii}N_i^2 - N_i \left[ \sum_{j=1}^{ns} K_{ij}N_j \right]. \quad (12)$$

Since dry mineral dust particles essentially do not stick together, there is no intramodal coagulation, and consequently the first term on the RHS of eq. (12) vanishes for mineral dust.

Interactions between aerosol particles and clouds are parameterized by an ex-

explicit activation scheme based on Köhler theory (Abdul-Razzak and Ghan, 2000). As mentioned above, HAM2.3 enables the explicit calculation of cloud droplet and ice crystal number concentrations, which is done via a two-moment cloud microphysics scheme (Lohmann et al., 2007; Lohmann and Hoose, 2009). The optical properties of the aerosols are not calculated online in order to save computational costs. Instead, a look-up table provides pre-calculated values based on Mie theory and contains the Mie size parameter and the real and imaginary part of the refractive index. Aerosols and aerosol precursor are emitted from various natural (biosphere, ocean, etc.) and anthropogenic sectors (industry, ships, power plants, etc.), where natural emissions are calculated online while emissions from anthropogenic sectors are provided in form of external input fields (see 4.2). Considered particle removal processes include dry deposition, sedimentation based on a Stokes settling velocity approach, and particle-size-dependent in- and belowcloud scavenging (Croft et al., 2009, 2010).

Of particular importance in the scope of this study is the treatment of mineral dust aerosol in HAM2.3. Since dust is only emitted from arid and semi-arid areas without vegetation or covered only by low vegetation, the determination of those regions is a crucial point in order to attain a suitable parameterization of the dust emission process. In all simulations, a scheme introduced by Stanelle et al. (2014) is used, which enables a fully interactive coupling between JSBACH and ECHAM6 with respect to dust emissions and was developed in order to investigate the impact of anthropogenic land use change on the global dust cycle. Hereby, terrestrial tiles not covered by any vegetation represent potential dust source areas, whereas tiles covered by snow or vegetation block dust emissions. While gaps in low-stature vegetation such as shrubs and crops allow for dust emissions, gaps in forests prevent them. The direct coupling of the dust emissions to the land surface and vegetation model automatically accounts for any changes, for instance in the land-sea distribution as a consequence of past climate changes. The dust emission process is parameterized based on the wind speed at 10 m elevation. In order to determine the total emission flux, particles of all soil types are divided into 192 dust size bins ranging from 0.2  $\mu\text{m}$  to 1300  $\mu\text{m}$ , and a threshold friction velocity is calculated individually for each bin (Marticorena et al., 1997). The calculation of the saltation process is based on an explicit formulation of Marticorena and Bergametti (1995), and the horizontal dust flux  $G_{\text{tot}}$  is given by

$$G_{\text{tot}} = E C \frac{\rho_a}{g} U^3 \int_{D_p} (1 + R)(1 - R^2) dS_{\text{rel}}(D_p) dD_p, \quad (13)$$

with the ratio of erodible to total surface  $E$ , an experimentally derived constant  $C = 2.61$  [White (1979)], the air density  $\rho_a$ , the wind friction velocity  $U$ , the particle diameter  $D_p$ , the ratio of threshold wind friction velocity to wind friction velocity  $R$  and the relative distribution of basal surfaces  $dS_{\text{rel}}(D_p)$ . The vertical dust flux is then calculated based on a formulation by White (1979) (Tegen et al., 2002), taking into account the soil moisture (because water increases the cohesive forces among dust particles) and the effective surface for dust emission.

In all dust source regions, a constant surface roughness length of 0.001 cm is prescribed. The vertical dust emission flux is finally calculated based on the horizontal dust flux according to White (1979), whereas the particles are emitted either into the insoluble accumulation mode (mass median radius (mmr) = 0.37  $\mu\text{m}$ ,  $\sigma = 1.59$ ) or the insoluble coarse mode (mmr = 1.75  $\mu\text{m}$ ,  $\sigma = 2.00$ ). Due to their short lifetimes, emissions into the super-coarse mode are neglected (Stier et al., 2005; Cheng et al., 2008). Since the surface orography is not taken into account in ECHAM6.3 in order to determine the aerodynamic surface roughness length, so-called regional correction factors are applied on the threshold friction velocity to account for “subsequent changes in surface wind distributions over dust source areas” (Tegen et al., 2019). They can be set for each dust source region individually and are chosen such that the simulated emissions match best with values by Huneus et al. (2011). These factors are also used in simulations to switch specific dust source areas on and off individually for the respective experiments.

### 3.2. HPC ENVIRONMENT & DATA ANALYSIS

ECHAM6.3-HAM2.3 is a massively parallelized model code mostly implemented in FORTRAN. All simulations were performed on AWI’s High Performance Computer (HPC) *Ollie*, a Cray CS400 AS System. The typical amount of resources used for running a simulation consists of 12 nodes, each made up of 36 Intel Xeon Broadwell (2.3 GHz) CPUs and 64 GB of RAM. The program consists essentially of the module files containing the code, the external input files (e. g., anthropogenic aerosol emissions, sea surface temperatures) and the namelist, which enables the user to change model parameters for a new simulation without having to recompile the code. For the analysis and visualization of the simulation data in the Network Common Data Format (netCDF), the softwares *Climate Data Operators* (CDO) and *Python* (standard packages *xarray*, *numpy*, *scipy*, *pandas*, *matplotlib*) are used.



## PART II

STUDIES - DISCUSSION - CONCLUSIONS



"How many times did the sun shine, how many times did the wind howl over the desolate tundras, over the bleak immensity of the Siberian taigas, over the brown deserts where the Earth's salt shines, over the high peaks capped with silver, over the shivering jungles, over the undulating forests of the tropics!"

---

(Émile Argand, *Tectonics of Asia*)

## 4. SIMULATING GLACIAL DUST CHANGES IN THE SOUTHERN HEMISPHERE USING ECHAM6.3-HAM2.3

### 4.1. THE ROLE OF MINERAL DUST DURING THE LAST GLACIAL MAXIMUM

In the last few decades, mineral dust has been identified as playing an important role in the climate system due to its various interactions in atmospheric processes (e.g. Maher et al. (2010)). The emission of dust particles takes place in arid and semi-arid areas and is controlled by several meteorological factors and surface properties in the source areas, for instance, wind speed, soil moisture, the type and amount of vegetation, soil composition, and the occurrence of other non-erodible elements (Goudie, 2008). Once suspended, especially smaller dust particles can get transported over large distances and distributed by the global atmospheric circulation before they are removed from the atmosphere by sedimentation, turbulent deposition, or scavenging. During transport, the dust particles directly influence Earth's radiation budget by scattering and absorbing shortwave and longwave radiation depending on particle size and mineralogical composition (Dufresne et al., 2002; Balkanski et al., 2007), which in turn affects the atmospheric stability by altering the vertical temperature profile and relative humidity (Boucher, 2015). Besides these direct effects on the energy budget, mineral dust particles act as cloud condensation and ice nuclei and thus affect optical and other microphysical properties of clouds, which again influences the radiation budget (Spracklen et al., 2008). However, the role of mineral dust in the Earth system is by no means limited solely to the radiative energy balance. Depending on the mineralogical

composition of the dust particles, they may constitute a very important source of micronutrients for some ecosystems. By acting as a fertilizer for the vegetation and the biosphere in general, mineral dust also plays a crucial role in the carbon cycle and its impact on the global climate. Saharan dust, for instance, has been identified to represent an important source of phosphorus for the Amazon rainforest, where the soil shows a general depletion (Reichholf, 1986). Another example for an ecosystem depending on the fertilizing effects of dust is the Southern Ocean (SO). Onboard incubation experiments showed that the bioproductivity in this region is strictly limited by iron availability (Martin et al., 1990). Based on the results of these experiments, Martin (1990) proposed the so-called iron hypothesis, which states that increased amounts of bioavailable iron were supplied during glacials in that region by enhanced mineral dust deposition. As a consequence of the atmospheric iron input, phytoplankton blooms emerged, binding huge amounts of CO<sub>2</sub>. After death, large parts of the organic matter sunk down into the deep sea, effectively removing the bound CO<sub>2</sub> from the atmosphere and thus contributing significantly to the observed reduction from 280 ppm to well below 200 ppm CO<sub>2</sub> during the last glacial period. Estimates based on paleoceanographic data constrain the upper limit of this effect to 40 ppm, since increased aeolian dust fluxes are only observed once the atmospheric CO<sub>2</sub> concentration had already decreased by 40 to 50 ppm (Martínez-García et al., 2014).

The analysis of ice cores and marine sediments from both hemispheres has provided detailed data on the spatial and temporal variability of dust deposition fluxes, both in total amount and particle size distribution, over the last million years on a global scale and has enabled the utilization of mineral dust as a climate proxy. However, the interpretation of these data turns out to be quite challenging due to their multifactorial causes. For instance, it has not yet been finally resolved whether climatic changes in the source regions (e.g. soil moisture, wind speed, vegetation cover) or changes in the atmosphere (e.g. wind speed, circulation patterns, particle lifetime) were the primary driver causing up to 20 times higher dust fluxes to Antarctica during glacials (Kohfeld and Ridgwell, 2009; Wolff et al., 2010). The situation is similar with the data on particle sizes. Ice core data from Greenland, for instance, show the deposition of significantly coarser dust during cold climates (Steffensen, 1997), which has been interpreted as a consequence of stronger winds transporting coarser particles over larger distances or as a result of the appearance of a closer dust source not active during warmer climates (Mahowald et al., 2014). Contrastingly, ice core data from Antarctica indicate the

deposition of generally finer particles during glacials, although a regional analysis reveals the deposition of slightly coarser particles in parts of central East Antarctica (Delmonte et al., 2002, 2004). The regional difference is explained by changes in the atmospheric circulation leading to dust transport pathways of different lengths from the sources to the deposition areas. On longer trajectories, a larger proportion of coarser particles gets removed during transport, and the observed particle size distribution in the deposition area is consequently shifted to finer particles. In order to support or reject such a hypothesis, the unambiguous identification of the dust's provenance is indispensable. Based on measurements of strontium (Sr) and neodymium (Nd) isotope ratios, southern South America has been identified as the most likely source of dust found in Antarctic ice cores that has been delivered during the last glacial (Basile et al., 1997). This finding has been supported by the study of Lunt and Valdes (2002), who found via a back-trajectory modeling approach that “[mineral dust] transport from Patagonia [to Antarctica] is much more efficient than transport from both Australia and South Africa”, which the authors explain by the southward extension of Patagonia well into “the strong winds over the SO”. However, it is still challenging to identify minor source contributions in the presence of a predominant dust source (Vallelonga, 2014). For instance, the characteristic isotope ratios of  $^{87}\text{Sr}/^{86}\text{Sr}$  and  $^{143}\text{Nd}/^{144}\text{Nd}$  of mineral dust found in Antarctic ice cores and delivered during interglacials match not only those of southern South American soil samples but also the ratio of soil samples from central and southeastern Australia (De Deckker et al., 2010). This finding suggests that transport of Australian dust to Antarctica is generally possible and raises the question if and to what degree Australian dust sources might also have contributed to the total amount of dust found in ice cores during glacials and which climate elements caused the according changes.

In this study, a state-of-the-art atmospheric general circulation model coupled to an aerosol model is used in order to provide new global simulations of the dust cycle for different climate conditions. The present-day simulation results are compared to results obtained in the scope of the global dust model intercomparison in AeroCom phase I in order to assess the performance of the model. The main focus of this study is, however, a comprehensive and quantitative characterization of the global dust cycle during the last glacial maximum (LGM, 21 ka), in particular compared to the pre-industrial (PI, 1850–1879 CE) dust cycle. In order to verify the simulation results, observational data are being used for a detailed comparison. The provenance studies focus on the Southern Hemisphere (SH) and give

new insights on the respective contribution of the three major dust source regions, Australia, South Africa, and Patagonia, to the total dust deposition in the SH. Finally, the combined global and local information on particle sizes and lifetimes, as well as precipitation and wind patterns, is used to draw conclusions concerning the atmospheric circulation in the SH during the LGM.

## 4.2. SIMULATION SETUP AND EXPERIMENTS

Global simulations are performed for present-day (PD, 1996-2005 CE), pre-industrial (PI, 1850–1880 CE) and last glacial maximum (LGM, 21 ka) climate conditions using the spatial resolution T63 ( $1.875^\circ \times 1.875^\circ$ ) with 47 vertical layers. While an initial run (“cold start”) is performed for PD and PI, the model is initialized by restart files for the LGM, which represent a dynamic equilibrium of the model obtained after several hundred simulation years for the according topographic, vegetation, and climate conditions. The spin-up time is 10 years for PD and PI and 20 years for the LGM, and the total simulation period is 20 years for PD, 40 years for PI, and 50 years for LGM. Except for PD, the final 30 simulation years are evaluated in order to calculate mean values. The simulation setup consists of an atmosphere-only model, i.e. the model is not coupled to an ocean model. Instead, the boundary conditions for the sea surface temperature and the sea ice concentration are provided in form of monthly resolved input files. For PD, monthly resolved 30-year means for the years 1979–2008 based on the Atmospheric Model Intercomparison Project – Phase II (AMIP II) dataset (Taylor et al., 2000) are used, for PI monthly resolved 30-year means for the years 1870–1899 created in the scope of the Program for Climate Model Diagnosis and Intercomparison (PCMDI) based on the latest AMIP II dataset (Durack and Taylor, 2019) are prescribed. For the LGM, monthly resolved 30-year means based on reconstructions in the scope of the Glacial Atlantic Ocean Mapping (GLAMAP, Paul and Schäfer-Neth (2003)) are used. The emission of aerosols and aerosol precursor from various anthropogenic sectors (see Schultz et al. (2018)) for PI and PD are prescribed in form of monthly resolved input files based on the Atmospheric Chemistry and Climate Model Intercomparison Project (ACCMIP) dataset (Lamarque et al., 2010). For LGM runs, greenhouse gas concentrations, orbital parameters and the glacier mask (GLAC-1D) have been set in accordance with the Paleoclimate Model Intercomparison Project – Phase 4 (PMIP4) experimental setup (Kageyama et al., 2017). Since a large amount of water was bound in ice sheets covering large parts of North America and northern Europe during the LGM, the land–sea mask has also been updated accordingly in order to

account for a 125 m lower sea level compared to present-day conditions (e.g. Clark et al. (2009)). In all simulations, dynamic vegetation is calculated online by JSBACH. It should be mentioned that the JSBACH restart files used for the LGM run initialize a desert in a small region on the northeastern coast of South America. Although efforts to reconstruct the vegetation in the Amazon region indeed show a patch-like retreat of the rainforest during the LGM, the surrounding vegetation is instead suggested to have consisted of tropical grassland instead of a desert (e.g. Ray and Adams (2001)). Consequently, dust emissions are prohibited in this region and accept this small shortcoming of the land surface and vegetation model.

### 4.3. RESULTS AND DISCUSSION

#### 4.3.1. MODEL PERFORMANCE FOR PRESENT-DAY CLIMATE CONDITIONS

The present-day simulation is intended to evaluate the model's performance concerning the representation of the global dust cycle. Table 4.1 shows a comparison of several key values used to characterize the global dust cycle budget of the modeling results in relation to the global dust model intercomparison in AeroCom phase I for present-day climate conditions (Huneeus et al., 2011). In terms of total annual dust emissions, the model simulates  $1221 \text{ Tg yr}^{-1}$ , which is close to the AeroCom median values of  $1123 \text{ Tg yr}^{-1}$ . Generally, the model performs at the lower end of the  $1000$  to  $4000 \text{ Tg yr}^{-1}$  range of dust emissions estimated by the IPCC (Intergovernmental Panel on Climate Change, 2014), which is caused by the neglect of a super-coarse particle mode (Stanelle et al., 2014). As a consequence of the comparably small particle sizes, the simulated atmospheric dust burden of  $19.8 \text{ Tg}$  is slightly higher than the AeroCom median of  $15.8 \text{ Tg}$ , which also leads to a higher averaged particle lifetime of  $5.96 \text{ d}$  compared to the  $4.59 \text{ d}$  for the AeroCom median. A noticeable difference is also the respective contribution of the three different deposition mechanisms, wet deposition, dry deposition, and sedimentation. While the AeroCom median suggests an almost equal proportion of  $357$ ,  $396$ , and  $314 \text{ Tg yr}^{-1}$ , respectively, the most dominant deposition mechanism in the model is wet deposition, with  $708 \text{ Tg yr}^{-1}$ , followed by sedimentation ( $412 \text{ Tg yr}^{-1}$ ), and finally dry deposition ( $93 \text{ Tg yr}^{-1}$ ). Again, this can be explained with the comparably small particle sizes: dry deposition and sedimentation apply first and foremost to larger particles close to the source regions, while rain scavenging is the predominant deposition mechanism in remote areas after long-range transport, which mostly applies to smaller particles in particular. Based on this intercomparison it is con-

#### 4. Glacial Dust Changes in the Southern Hemisphere

| Model / experiment                      | Emission<br>[Tg yr <sup>-1</sup> ] | Burden<br>[Tg]     | Deposition<br>[Tg yr <sup>-1</sup> ] | Wet deposition<br>[Tg yr <sup>-1</sup> ] | Dry deposition<br>[Tg yr <sup>-1</sup> ] | Sedimentation<br>[Tg yr <sup>-1</sup> ] |
|---|------------------------------------|--------------------|--------------------------------------|--|--|---|
| ECHAM6.3-HAM2.3<br>mean 1996-2005       | 1221                               | 19.8               | 1213                                 | 708                                      | 93                                       | 412                                     |
| AeroCom median for<br>year 2000 (range) | 1123<br>(514-4313)                 | 15.8<br>(6.8-29.5) | 1257<br>(676-4359)                   | 357<br>(295-1382)                        | 396<br>(37-2791)                         | 314<br>(22-2475)                        |

**Table 4.1.** Comparison of key values characterizing the global dust cycle budget between the model used in this study, ECHAM6.3-HAM2.3, and the AeroCom median resulting from an intercomparison of 14 different atmosphere models for present-day climate conditions (Huneus et al., 2011). [Table taken from Krättschmer et al. (2022)]

cluded that the model setup used in this study represents the global dust cycle adequately for the following investigations. A comparison of the simulated total dust deposition with observational data from 84 sites provided by Huneus et al. (2011) can be found in the appendix A (Figs. A.1 and A.2).

#### 4.3.2. THE DUST CYCLE UNDER PRE-INDUSTRIAL AND LAST GLACIAL MAXIMUM CLIMATE CONDITIONS

##### 4.3.2.1 OVERVIEW

Figure 4.1 shows the results concerning the global dust cycle for PI and the LGM. An annual global dust emission of 923 and 5159 Tg yr<sup>-1</sup> is found for PI and the LGM, respectively. The model identifies northern Africa and Asia as major dust source regions in the Northern Hemisphere and southern South America, southern Africa, and Australia as major dust source regions in the SH (Fig. 4.1a and b). The zonally averaged dust emissions shown in Fig. 4.1c reveal that while all sources emit noticeably more dust during the LGM compared to PI, the increase is most significant for Asia, northern Africa, and Australia. As a consequence of the higher dust emissions during the LGM, the dust burden also increases from 16 to 99 Tg. Once emitted, the dust is distributed by the atmospheric circulation (Fig. 4.1d and e). The northeasterly and southeasterly trade winds transport in particular northern and southern African dust along the Equator over the Atlantic Ocean, while dust emitted in Asia and southern South America (and Australia) gets transported by the westerlies over the Pacific Ocean and the SO, respectively. Finally, the dust deposition patterns naturally follow the dust burden patterns (Fig. 4.1g and h).

#### 4. Glacial Dust Changes in the Southern Hemisphere

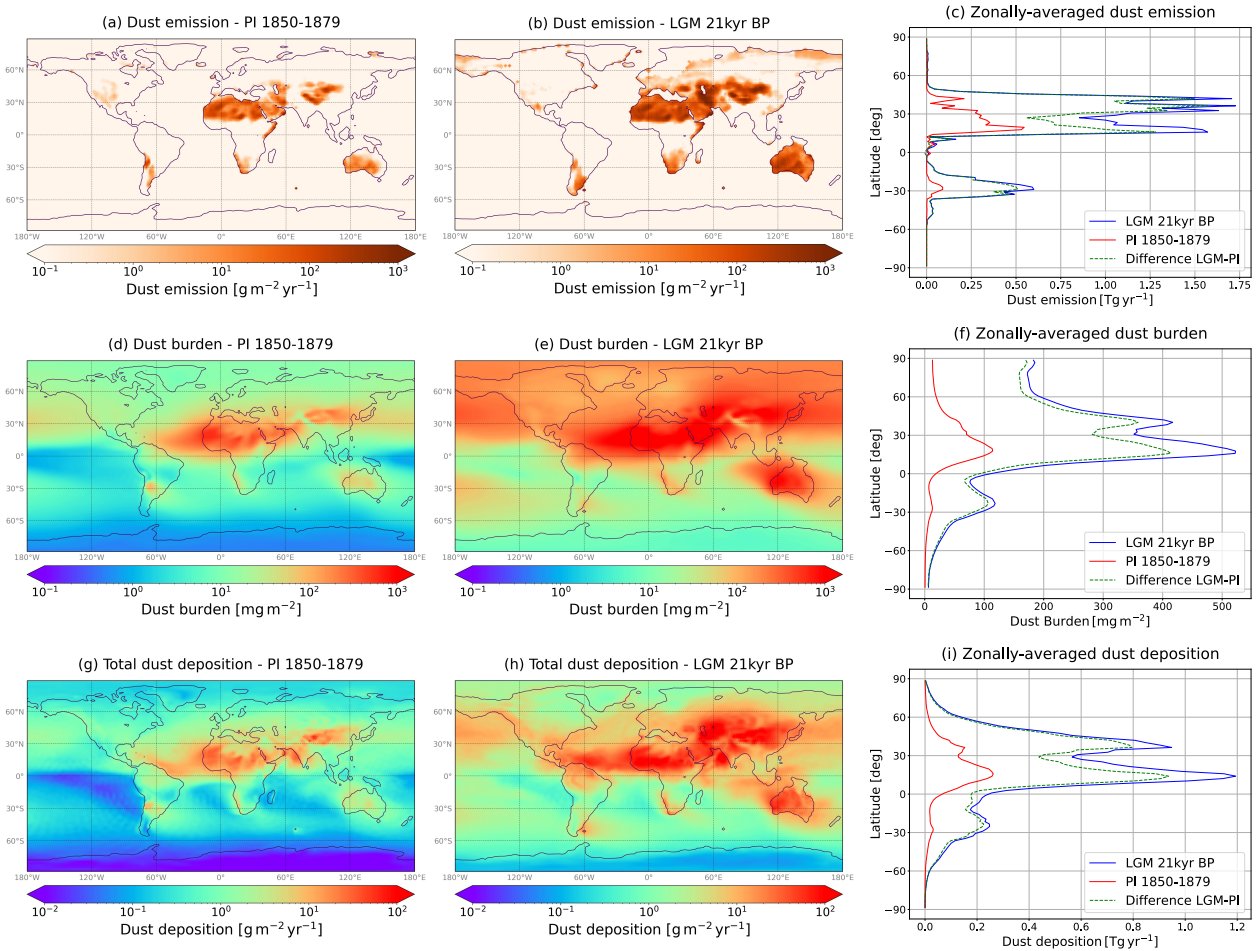


**Figure 4.1.** Global maps showing the dust emission, burden and deposition for PI (a, d, g) and LGM climate conditions (b, e, h). Additionally, zonally averaged graphs are shown for all quantities (c, f, i). [Figure taken from Krättschmer et al. (2022)]

As expected, the depositions in midlatitudes close to the source regions are higher during the LGM (Fig. 4.1i). However, it should be noted that in remote regions in both hemispheres more dust deposition also occurs, particularly in the high latitudes. The model simulates a deposition of 423 Tg yr<sup>-1</sup> (45 %) and 2122 Tg yr<sup>-1</sup> (41 %) onto the oceans globally for PI and the LGM.

With respect to dust emissions, the obtained values are lower than the simulated 2785 Tg yr<sup>-1</sup> for PI and 6294 Tg yr<sup>-1</sup> for the LGM of the Community Earth System Model (CESM) [Albani and Mahowald (2019)], whereas the differences are more significant for PI (Table 4.2). The major dust source regions identified for both the Northern Hemisphere and the SH are in accordance with other studies [e.g. Takemura et al. (2009)], suggesting that the interactive coupling of dust emissions to the land surface and vegetation model JSBACH in the model yields reliable results (see Table 4.3 for detailed regional values). As a consequence of the atmospheric

#### 4. Glacial Dust Changes in the Southern Hemisphere

| Model / experiment                   | Emission<br>[Tg yr <sup>-1</sup> ] | Burden<br>[Tg] | Deposition<br>[Tg yr <sup>-1</sup> ] | Wet deposition<br>[Tg yr <sup>-1</sup> ] | Dry deposition<br>[Tg yr <sup>-1</sup> ] | Sedimentation<br>[Tg yr <sup>-1</sup> ] |
|--------------------------------------|------------------------------------|----------------|--------------------------------------|--|--|---|
| ECHAM6.3-HAM2.3<br>mean PI 1850-1879 | 923                                | 16             | 929                                  | 547                                      | 57                                       | 325                                     |
| CESM<br>PI year 1850                 | 2785                               | 20             | -                                    | -  | -  | -                                       |
| ECHAM6.3-HAM2.3<br>mean LGM 21ka     | 5159                               | 99             | 5171                                 | 3096                                     | 473                                      | 1602                                    |
| CESM<br>LGM 21ka                     | 6294                               | 37             | -                                    | -  | -  | -                                       |

**Table 4.2.** Key values for dust emission, burden, and deposition characterizing the global dust cycle budget as simulated by ECHAM6.3-HAM2.3 compared to results obtained with CESM (Albani and Mahowald, 2019). [Table taken from Krättschmer et al. (2022)]

circulation pattern, the increased zonally averaged dust burden in the high northern latitudes during the LGM (Fig. 4.1f) can at least partly be attributed to the markedly higher dust emissions in Asia compared to PI, which is in accordance with results by Werner et al. (2002). With respect to dust deposition, the model simulates a higher relative proportion of dust deposited over the oceans than the 440 Tg yr<sup>-1</sup> (16 %) for PI and the 826 Tg yr<sup>-1</sup> (13 %) for LGM found by Albani et al. (2016) using CESM. Shao et al. (2011) evaluated results of several modeling studies and found on average a dust emission of 2000 Tg yr<sup>-1</sup>, of which 25 % deposit over the oceans. Regardless of the differences in absolute numbers it is worth noting that both models indicate a decreased deposition proportion for LGM climate conditions. However, it is possible that the prescribed SSTs are too warm (Tierney et al., 2020). While this study does not indicate a suggested equatorward shift of the westerlies, other studies have shown an influence of prescribed SSTs and SIC on the westerlies (e.g. Sime et al. (2013)).

Based on the previous findings, it can be concluded that the differences of ECHAM6.3-HAM2.3 in comparison to CESM in terms of dust modeling can be traced back to the modeled particle size distribution. The atmospheric component of CESM, CAM4, utilizes a sectional approach in order to represent the particle size distribution, grouping the particles into four size bins ranging from 0.1 to 10  $\mu\text{m}$  in diameter (Mahowald et al., 2006). The higher dust emission fluxes in CESM, in particular for PI climate conditions, are consequently caused by larger particles,

#### 4. Glacial Dust Changes in the Southern Hemisphere

| Emission [ $\text{Tg yr}^{-1}$ ] | PI 1850-1879 | LGM 21 ka     | LGM/PI ratio |
|----------------------------------|--------------|---------------|--------------|
| Globally                         | 923          | 5159          | 5.6          |
| Northern Hemisphere              | 835 (90.6 %) | 4300 (83.3 %) | 5.3          |
| Southern Hemisphere              | 88 (9.4 %)   | 859 (16.7 %)  | 9.8          |
| Sahara                           | 535          | 1626          | 3            |
| Arabian Peninsula                | 70           | 430           | 6.1          |
| Asia                             | 204          | 1803          | 8.8          |
| Australia                        | 47           | 748           | 15.9         |
| Southern Africa                  | 12           | 63            | 5.3          |
| Patagonia                        | 2.3          | 36            | 15.6         |

**Table 4.3.** Global and regional dust emissions during the PI and LGM in  $\text{Tg yr}^{-1}$  and the LGM/PI ratio. [Table taken from Krättschmer et al. (2022)]

which add to the mass budget significantly, and their rapid sedimentation close to the source regions lowers the average particle lifetime (Albani et al., 2014). The smaller particle sizes modeled by ECHAM6.3-HAM2.3, however, enable long-range transport to remote regions for a large proportion of the emitted dust and consequently causes wet scavenging to become the predominant deposition mechanism. The importance of an adequate modeling of finer dust in order to achieve a proper representation of long-range transport and subsequent deposition over the oceans has already been pointed out by Mahowald et al. (2014). In the end, the question as to how well the model performs in absolute values can only be evaluated by comparing the results to measurement data, which is done in Section 4.3.2.2.

On average 5.6 times higher dust emissions are simulated for LGM compared to PI climate conditions (Table 4.3). While the increase is only 5.3-fold in the Northern Hemisphere, the ratio is even 9.8 for the SH. This raises a question concerning the causes of this significant increase. One obvious reason is the difference in the land–sea distribution, as can be seen in Fig. 4.1. Globally, the extended drylands during the LGM in the coastal regions as a consequence of the lower sea level, for instance in South America and Australia (Fig. 4.1a and b), emit  $229 \text{ Tg yr}^{-1}$  of mineral dust and thus contribute only around 5 % to the total increase. On a regional scale, the extended drylands contribute around 13 % in Australia and 10 % in southern Africa to the increased dust emissions. Only in southern South America, does more than 80 % of the increased dust emissions during the LGM come from the extended drylands (see Table 4.4). However, dust emissions also depend on

#### 4. Glacial Dust Changes in the Southern Hemisphere

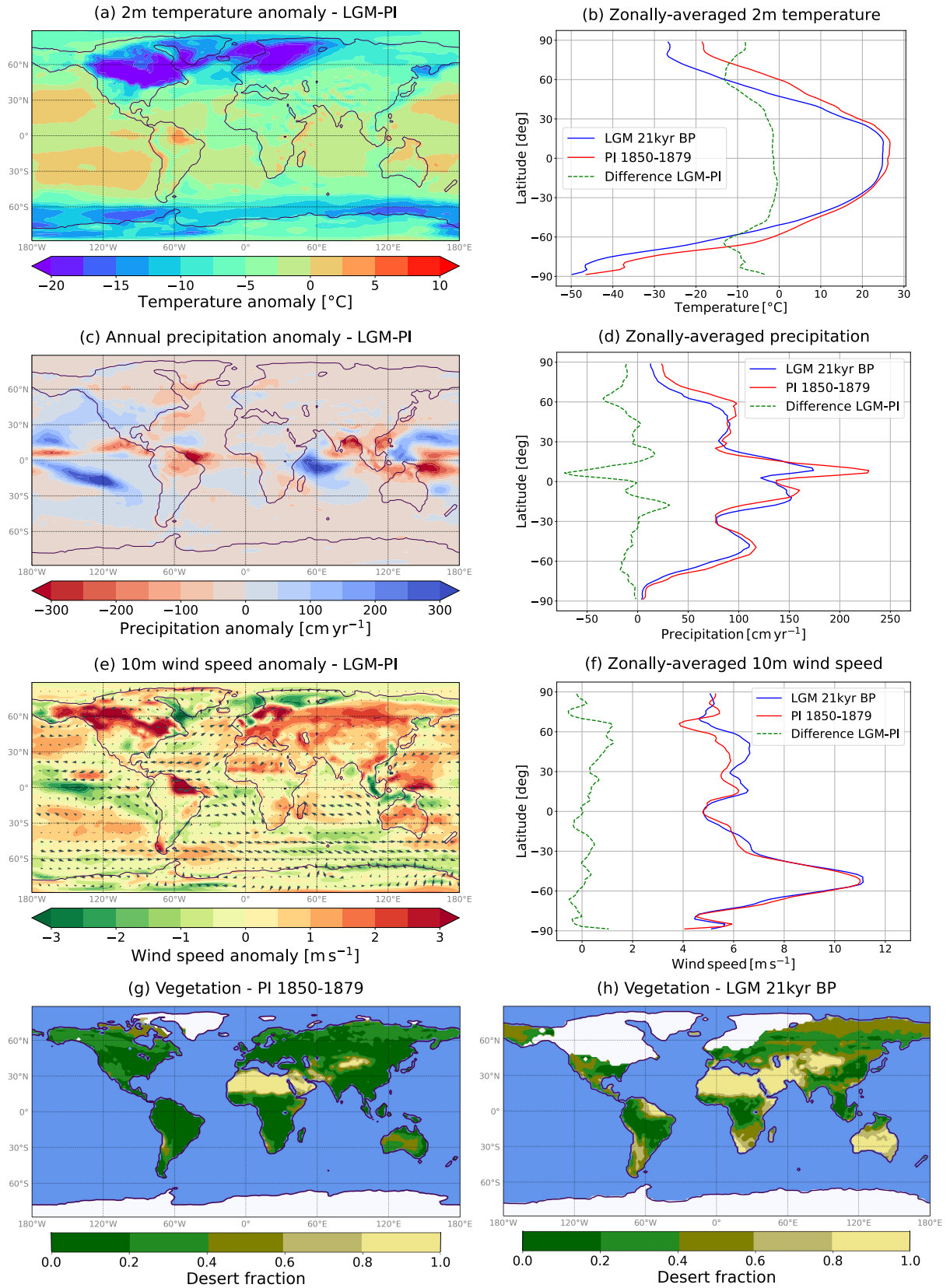


**Figure 4.2.** Global maps and zonally averaged graphs of anomalies (LGM-PI) in the 2 m temperature (a, b), annual precipitation (c, d), 10 m wind speed (e, f), and desert fraction for each grid box for both PI and LGM (g, h). Please note that glaciers (white) and the ocean (blue) have been colored in (g) and (h) for improved readability. [Figure taken from Krättschmer et al. (2022)]

meteorological factors like wind speed and soil moisture. Figure 4.2 shows anomalies (LGM - PI) with respect to the 2 m temperature, annual precipitation, and 10 m wind speed. The ice sheet over North America and northern Europe caused a significant temperature drop in the corresponding regions during the LGM (Fig. 4.2a), while the decrease around the Equator was less pronounced, which resulted in a globally averaged lower temperature of  $-4.1^{\circ}\text{C}$ . The steeper temperature gradient between high latitudes and the Equator during the LGM (Fig. 4.2b) caused noticeably stronger winds in the Northern Hemisphere (Fig. 4.2e and f), and the generally colder climate resulted in a precipitation decline at the Equator and close to the poles (Fig. 4.2c and d), averaging to a global anomaly of  $-6.8\text{ cm yr}^{-1}$ . Since precipitation acts as an effective deposition mechanism, the drier climate north of  $45^{\circ}\text{ N}$  also contributes to the higher dust burden towards the North Pole as a result of the increased particle lifetime in addition to the higher dust emissions in Asia (Fig. 4.1f). In the Northern Hemisphere the wind speed anomaly averages to  $0.49\text{ m s}^{-1}$ , and Fig. 4.2e reveals that there was an increase over the major dust source regions of Asia and northern Africa. Although the zonally averaged wind speed in Fig. 4.2f suggests no significant differences between LGM and the PI in the SH ( $0.04\text{ m s}^{-1}$ ), the map shown in Fig. 4.2e indicates considerable differences over the major SH dust source regions. A regional analysis yields a 10 m wind speed anomaly of  $0.77\text{ m s}^{-1}$  over Australia,  $0.44\text{ m s}^{-1}$  over southern Africa, and  $0.52\text{ m s}^{-1}$  over Patagonia. With respect to precipitation, the model simulates a decrease of  $-31.7\text{ cm yr}^{-1}$  for Australia and  $-28.2\text{ cm yr}^{-1}$  for southern Africa and a slight increase of  $7.1\text{ cm yr}^{-1}$  for Patagonia (Fig. 4.2c). These findings are in agreement with results by Rojas et al. (2009), who found in the scope of the PMIP2 simulations a generally colder, drier climate south of  $40^{\circ}\text{ S}$  but slightly more precipitation over Patagonia during the LGM. Finally, the dust emissions also depend on the vegetation cover. As can be seen in Fig. 4.2g and h, arid and semi-arid areas were substantially further extended during the LGM compared to PI, particularly in Asia, Australia, southern Africa, and Patagonia.

Based on the findings, it is concluded that the increase in dust emissions during the LGM compared to the PI was caused by extended drylands in the source regions and at the coasts due to a lower sea level, reduced vegetation cover, regionally increased wind speeds, and less precipitation over the source regions, which is also in agreement with findings by Lunt and Valdes (2002).

##### 4.3.2.2 COMPARISON TO OBSERVATIONAL DATA

The compilation of dust deposition data from Kohfeld et al. (2013) is used for a comparison between the simulated dust deposition in the SH and data based on marine sediment and ice core analysis.

Figure 4.3 shows dust deposition maps including observations and scatter plots comparing simulated and measured dust deposition for the PI, LGM, and the LGM/PI ratio. For a more differentiated analysis, the data points have been categorized into five groups according to their geographical region. For both PI and the LGM, the simulated values are mostly in accordance with the observed values for the Atlantic Ocean (Fig. 4.3b and d, blue diamonds). Due to the atmospheric circulation, dust deposited in the region close to the Equator originates mainly from the Sahara and southern Africa, whereas dust deposited in the southern Atlantic Ocean is mainly of southern South American origin. The model reveals a tendency to underestimate the depositions over the Pacific Ocean and Pacific SO, particularly in the PI simulation (Fig. 4.3b and d, green circles and triangles), as well as a systematic overestimation of the dust depositions onto Antarctica (Fig. 4.3b and d, orange pentagons) by an order of magnitude. At least for the Pacific region, Australia can be assumed to be the major source, which indicates that the model simulates too low dust emissions. However, the dust deposited over the Tasman Sea is also very likely of Australian origin (Fig. 4.3b and d, red crosses). While the simulation values are in good accordance with the observations in that region for PI, the model overestimates the dust deposition during the LGM. Figure 4.3e and f show a comparison between the simulated dust deposition ratios LGM/PI and the measurement values, suggesting that this ratio varies strongly on a regional scale. For instance, the simulation results indicate a 5-fold to 40-fold increase in dust deposition over Antarctica, whereas a 1-fold to 4-fold increase has been simulated over the Atlantic (Fig. 4.3f).

As the analyses of dust provenance (Sect. 3.2.3) reveal, the dust deposition over Antarctica is dominated by the Australian contribution during the LGM. Thus, the comparison of the model results with the observational data showing lower simulated values in the Pacific Ocean and Pacific SO gives no clear hint as to whether Australia's source strength is overestimated or underestimated in the model. A possible factor contributing to this inconsistency could be a too high transport efficiency of dust towards the South Pole. However, considering the difference in absolute values between dust deposition over the Pacific Ocean and Antarctica, which is almost 3 orders of magnitude, a too high transport efficiency can be ex-

#### 4. Glacial Dust Changes in the Southern Hemisphere

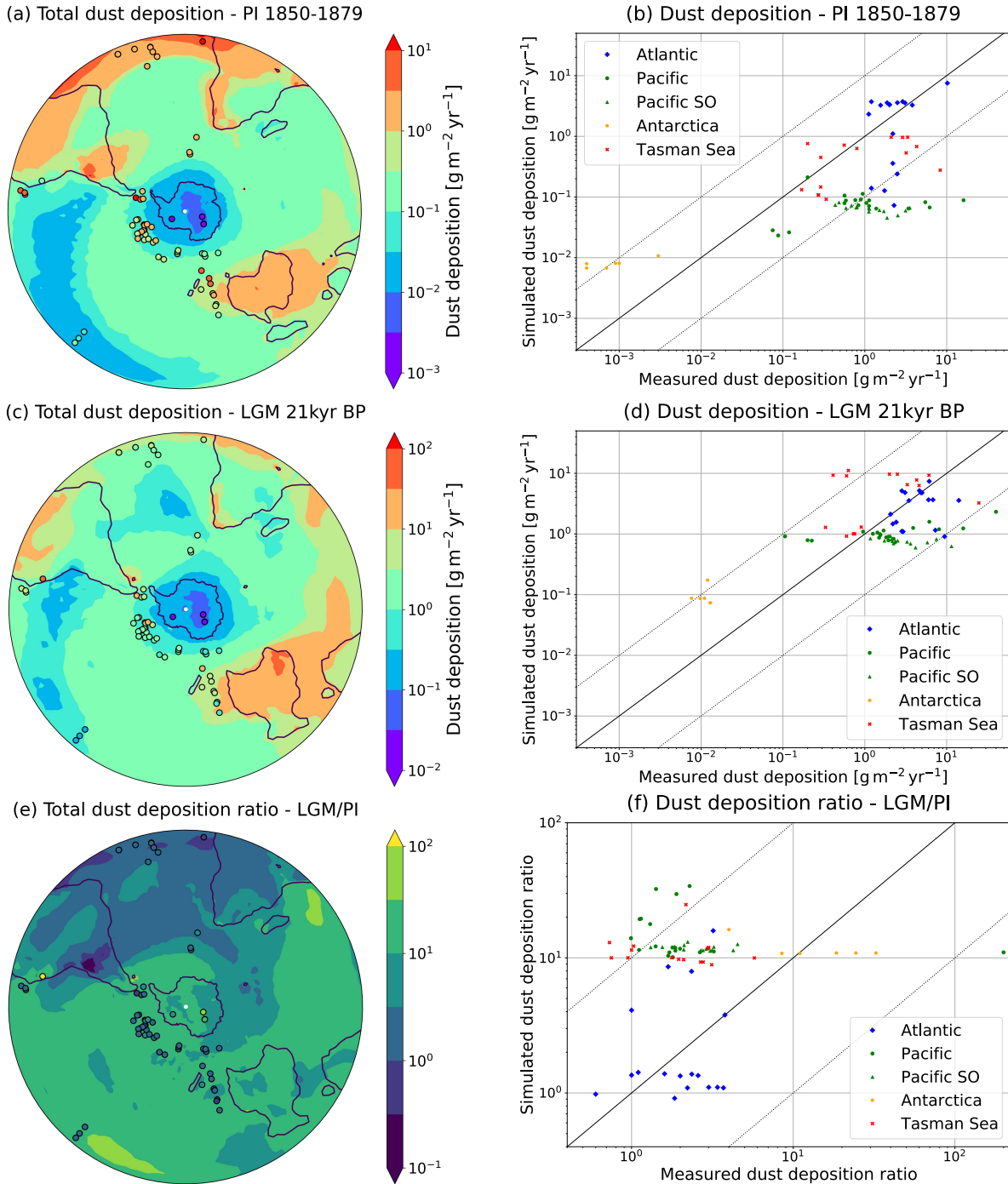


**Figure 4.3.** Comparison between the simulated total dust deposition and observational data [Kohfeld et al. (2013)] (in  $\text{g m}^{-2} \text{yr}^{-1}$ ) from several regions in the SH and the according scatter plots for the PI (a, b) and LGM (c, d). Panels (e) and (f) show the according simulated and measured dust deposition ratio LGM/PI. Please note the different value ranges in (a) and (c). [Figure taken from Krättschmer et al. (2022)]

cluded as the sole reason for the discrepancies. Another factor that needs to be considered are non-aeolian contributions. Although data from “marine sites that

have been flagged because they are located within zones of thick nepheloid layers and ice-rafted detritus, which can contaminate aeolian signals” had already been excluded from the dataset used for comparison (Kohfeld et al., 2013), the reconstructed detrital flux estimates might still contain contributions from glacier erosion and riverine input, which are not considered in the model. The dust flux reconstructions are based on the assumption of relatively constant proportions of  $^{232}\text{Th}$  in continental lithogenic materials and might thus be overestimated by 30 %–40 % in regions receiving fine-grained dust from Patagonia and Australia since fine sediments have “a reduced proportion of low- $^{232}\text{Th}$  phases such as quartz and feldspar” (McGee et al., 2015). The lack of non-aeolian contributions in the model might also contribute to the fact that the simulated dust deposition fluxes appear so stratified in the Pacific Ocean and appear so stratified in the Pacific Ocean and the Pacific SO region compared region compared to the observational data (Fig. 4.3b and d) but could also indicate a model shortcoming in the representation of the dust deposition process on small scales. Finally, it should be taken into account that (simulated) aeolian dust deposition fluxes onto the ocean surface are compared to marine sediment data, i.e. any horizontal transport processes of the sediments deposited in the ocean are not also considered.

Sediment core analysis suggests that the total dust deposition flux during glacials over the Pacific SO is about 50 % of that over the Atlantic (Lamy et al., 2014), which can also be observed in the simulation results (Fig. 4.3d), revealing that the average dust deposition flux is around  $1\text{ g m}^{-2}\text{ yr}^{-1}$  in the Pacific SO and around  $2\text{ g m}^{-2}\text{ yr}^{-1}$  in the Atlantic Ocean. The globally averaged LGM-to-PI ratio of 5.6 found with ECHAM6.3-HAM2.3 (see Table 4.3) is slightly above the assumed 2- to 5-fold increase found in the literature (e. g., Kohfeld and Harrison (2001)). However, the 25-fold increase in dust deposition over Antarctica suggested by ice core data (Lambert et al., 2008) is in good accordance with the simulation results. Additionally, the observed 1- to 4-fold increase in dust depositions over the Atlantic is captured well by the model. As a consequence of the underestimation in the PI simulation, the dust deposition ratio is systematically too high for the Tasman Sea and the Pacific Ocean (Fig. 4.3f). Despite this, the model yields acceptable results in terms of absolute values for LGM climate conditions.

#### 4.3.2.3 DUST PROVENANCE STUDIES

In order to identify the relative contribution of the major dust source regions southern South America, southern Africa, and Australia to the total dust deposition in

#### 4. Glacial Dust Changes in the Southern Hemisphere

(a) Dust deposition contribution [%] - PI 1850-1879 (b) Dust deposition contribution [%] - LGM 21kyr BP

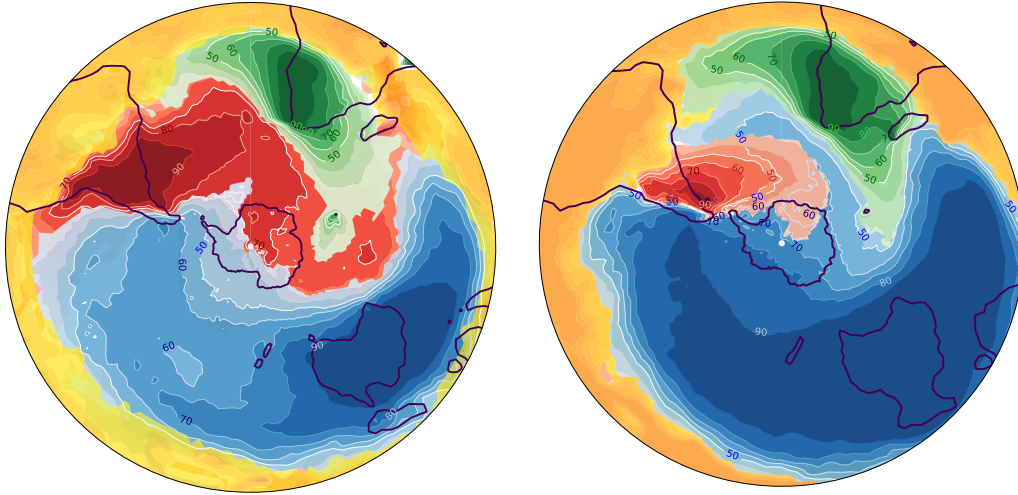


**Figure 4.4.** Results of the provenance studies showing the respective contribution of the major dust source regions South America (red), southern Africa (green), Australia (blue), and the Northern Hemisphere (yellow) to the total dust deposition in the SH as a percentage (white and blue numbers; different colors were merely chosen for improved readability) for PI **(a)** and LGM **(b)**. Note that the Kerguelen Islands have been considered a dust source in the SAFonly experiment and thus appear in the same color style applied for southern Africa. [Figure taken from Krätschmer et al. (2022)]

the SH, four additional simulations for both PI and LGM were performed. In each of them, source regions in the SH were independently switched on and off, while in all experiments all dust source regions in the Northern Hemisphere are still considered. The four simulations consist of a South America-only run (SAMonly, southern Africa and Australia switched off), a southern Africaonly run (SAFonly, South America and Australia switched off), an Australia-only run (AUSonly, South America and southern Africa switched off), and a Northern Hemisphere-only run (NORTHonly, all sources in the SH switched off) in order to identify the contribution of interhemispheric dust. Although New Zealand is discussed as a potential additional dust source during the LGM (Lamy et al., 2014; Koffman et al., 2021), the model only simulates dust emissions of less than  $1 \text{ Gg yr}^{-1}$  from this region, which is effectively negligible compared to the simulated emissions of  $748 \text{ Gg yr}^{-1}$  from Australia and  $36 \text{ Gg yr}^{-1}$  from Patagonia. Since the model runs at the rather coarse spatial resolution T63 (horizontal grid size of approx.  $1.8^\circ \times 1.8^\circ$ ), New Zealand's geographical expanse might only be marginally captured in the model, and thus the source strength could be underestimated.

Figure 4.4 reveals the relative contribution of the four major source regions South

America (red), southern Africa (green), Australia (blue), and the Northern Hemisphere (yellow) to the total dust deposition in the SH. For both PI and LGM, the maps reveal the typical dust transport patterns in the SH, which are the southeasterly trade winds for regions close to the Equator and the westerly wind belt for regions in the high latitudes. Along the Equator, dust deposition is dominated by interhemispheric dust originating from the Northern Hemisphere. For Antarctica, the experiments reveal for PI (Fig. 4.4a) that the deposited dust is coming from Australia and South America, of which the latter is predominant and contributes between 60 % and 80 % of the dust deposition over West Antarctica. Despite a significant increase in dust source strength of South America (Fig. 4.1b, Table 4.3) during the LGM that is similar to Australia, its relative contribution to the total dust deposition over the SO and Antarctica decreases (Fig. 4.4b). It is found that dust deposited over the SO in the eastern half of the SH originates mainly from southern South America, while dust deposited over the Pacific Ocean and Pacific SO is mainly of Australian origin. Those two sources generally contribute in sum slightly more than 90 % to the total dust deposition over the SO and Antarctica (60–90° S) for both PI and LGM conditions (Table 4.5).

Due to the interactive coupling of mineral dust in the model, it is checked whether the reduced dust load in the SH resulted in a shift in the zonally averaged precipitation and found no shifts regardless of the switched-off sources. The procedure and the findings are in agreement with results by Evans et al. (2020), who performed similar experiments in order to investigate the influence of the dust load asymmetry between the Northern Hemisphere and SH on the location of the Intertropical Convergence Zone (ITCZ) as a consequence of the resulting asymmetric radiative forcing. They likewise found that the influence of the SH is almost negligible compared to the Northern Hemisphere due to the much smaller contribution to the total global atmospheric dust load. Those findings raise the confidence that the experiments yield meaningful results. The model results for PI agree well with those found by Li et al. (2008) for current climate conditions using the GFDL Atmospheric General Circulation Model AM2, particularly the dominance of southern South American dust deposited over West Antarctica and the equal contributions of Australian and South American dust deposited over East Antarctica. The discussed combined contribution of Australia and South America of more than 90 % to the total dust deposition over the SO and Antarctica is again in accordance with results by Li et al. (2008), who found a combined contribution of more than 85 %. However, the identification of Australia as the predominant source for dust

#### 4. Glacial Dust Changes in the Southern Hemisphere

|                 | Additional land area<br>LGM [ $10^6$ km $^2$ ] | Dust emission PI<br>1850-1879 [ $\text{Tg yr}^{-1}$ ] | Dust emission LGM<br>21 ka [ $\text{Tg yr}^{-1}$ ] | Dust emission [ $\text{Tg yr}^{-1}$ ]<br>from additional land areas |
|-----------------|--|---|--|---|
| Globally        | 19.5   | 923   | 5159   | 229   |
| Australia       | 1.8  | 47  | 748  | 92  |
| Southern Africa | 0.04   | 12  | 63   | 5   |
| Patagonia       | 0.8  | 2.3   | 36   | 29  |

**Table 4.4.** Additional land areas in Australia, southern Africa, Patagonia, and globally during the LGM compared to the PI due to the lower sea level in  $10^6$  km $^2$  and the dust emissions from those extended drylands (in  $\text{Tg yr}^{-1}$ ). [Table taken from Krättschmer et al. (2022)]

| Deposition region |              | All sources<br>[ $\text{Tg yr}^{-1}$ ] | Australia<br>[ $\text{Tg yr}^{-1}$ ] | South America<br>[ $\text{Tg yr}^{-1}$ ] | South. Africa<br>[ $\text{Tg yr}^{-1}$ ] | North. Hem.<br>[ $\text{Tg yr}^{-1}$ ] |
|-------------------|--------------|--|--------------------------------------|--|--|--|
| Southern Ocean    | PI 1850-1879 | 1.04                                   | 0.38 (37 %)                          | 0.59 (54 %)                              | 0.09 (8 %)                               | 0.01 (1 %)                             |
|                   | LGM 21 ka    | 13.48                                  | 9.25 (69 %)                          | 3.07 (23 %)                              | 0.96 (7 %)                               | 0.2 (1 %)                              |
| Antarctica        | PI 1850-1879 | 0.21                                   | 0.06 (29 %)                          | 0.13 (62 %)                              | 0.02 (9 %)                               | 0.00 (0 %)                             |
|                   | LGM 21 ka    | 2.88                                   | 1.96 (68 %)                          | 0.69 (24 %)                              | 0.19 (7 %)                               | 0.03 (1 %)                             |

**Table 4.5.** Dust deposition onto Antarctica during the PI and LGM depending on the dust provenance (in  $\text{Tg yr}^{-1}$  and percent). [Table taken from Krättschmer et al. (2022)]

deposited over Antarctica during the LGM is inconsistent with observational data from Antarctic ice cores. The characteristic ratios of Sr and Nd isotopes suggest southern South America to be the most likely dust source, possibly with minor contributions up to 15 % from Australian or southern African dust sources (Basile et al., 1997; Delmonte et al., 2008). The contradicting results clearly indicate a shortcoming on the modeling side, and the further analysis is intended to uncover the mechanism causing this discrepancy.

Although both Australian and South American dust sources increase by a factor of around 15 in the model during the LGM compared to the PI (Table 4.3), the absolute amount of dust coming from Australia clearly dominates the SH. Only in a smaller region of East Antarctica does dust of South American origin contribute up to 40 % of the total deposition. The deposition pattern of Australian dust shown in Fig. 4.4b suggests an increased long-range transport, which can likely be attributed to the higher particle lifetime during the LGM as a consequence of the generally drier climate in the SH (Fig. 4.2c and d). At first glance, it seems

that this should apply to dust coming from both Australian and southern South American sources and might consequently not provide a possible explanation for the decrease in the relative contribution of southern South American dust to the total deposition. However, as discussed in Sect. 3.2.1, it is found that the regional climate over Patagonia and parts of the Atlantic area of the SO turned out to be slightly wetter during the LGM (Fig. 4.2c). Since the westerly wind belt is responsible for the dust transport at these latitudes, this suggests that dust of South American origin was removed by scavenging with a higher efficiency, while dust coming from Australia might have had higher particle lifetimes due to the drier climate simulated over the Pacific Ocean and Pacific SO.

##### 4.3.2.4 PARTICLE LIFETIME AND RADIUS ANOMALIES IN THE SH DURING THE LGM

In order to test this hypothesis of changed glacial particle lifetimes, the particle lifetime anomaly is investigated (Fig. 4.5a). The correlation between the particle lifetime anomaly and the precipitation anomaly (Fig. 4.5b) can easily be recognized, which is not surprising considering the fact that in Sect. 3.1 wet scavenging was identified as the predominant deposition mechanism in the model. Especially in regions close to the Equator, for instance in the Pacific Ocean and the Indian Ocean but also more southwards in the Atlantic Ocean and SO around 60° S, the pattern of increased precipitation causing shorter particle lifetimes can be clearly seen. To get more insights into the decrease of the relative importance of southern South American dust concerning the total dust deposition onto the SO and Antarctica, the particle lifetime southwards of the horse latitudes (30° S) were analyzed, since dust closer to the Equator is essentially transported northeastwards by the trade winds. On average, the drier climate south of 30° S during the LGM leads to an increased particle lifetime of 0.52 d. However, using the results of the provenance studies, it is found that the average particle lifetime of Australian dust increases by 1.12 d, whereas it decreases by -1.69 d for dust particles of southern South American origin. Since the particle lifetime eventually influences the transport range, the over-proportional importance of Australian dust in the SH during the LGM compared to PI conditions (Fig. 4.4a and b), particularly south of 60° S, can thus be explained by changes in the regional precipitation patterns.

Combining the results concerning changes in particle lifetime with the provenance studies, the ongoing debate whether changes in source strength or atmospheric particle lifetime were mainly responsible for the increased dust concentration during the LGM found in Antarctic ice cores shall be taken up on. Figure

#### 4. Glacial Dust Changes in the Southern Hemisphere

| Deposition region |              | Wet deposition [%] | Dry deposition [%] | Sedimentation [%] |
|-------------------|--------------|--------------------|--------------------|-------------------|
| 30-60° S          | PI 1850-1879 | 79                 | 8                  | 13                |
|                   | LGM 21 ka    | 68                 | 13                 | 19                |
| 60-90° S          | PI 1850-1879 | 91                 | 1                  | 8                 |
|                   | LGM 21 ka    | 92                 | 0                  | 8                 |

**Table 4.6.** Contribution of dust deposition mechanisms to the total dust deposition between 30 and 90° S during the PI and LGM in percent. [Table taken from Krätschmer et al. (2022)]

4.5c and d and Table 4.6 clearly show that wet scavenging is the main deposition mechanism for mineral dust between 60 and 90° S in the model, particularly over the SO, which is in agreement with the study of Markle et al. (2018), who found that precipitation is the “principal barrier to aerosols reaching the poles”. However, while the authors suggest that changes in particle lifetime are the main reason for the increased dust transport to Antarctica during glacials, the generally drier climate during the LGM simulated by the model only leads to a slightly higher particle lifetime on average. Of bigger importance in the scope of the simulations are the regional changes in precipitation, and thus in particle lifetime, because they eventually lead to Australia becoming the predominant source of dust deposited over Antarctica. Although the model overestimates the dust deposition over Antarctica for both PI and LGM by an order of magnitude (Fig. 4.3b and d), the simulated LGM-to-PI ratio of 14 (Table 4.5) is generally in good agreement with observations (Fig. 4.3e and f). Apparently, the almost 16-fold increase in dust source strength during the LGM compared to PI for both southern South America and Australia (Table 4.3) is necessary to achieve this accordance. Furthermore, the simulated increase in source activity during the LGM can be traced back to increases in wind speed over the source areas, reduced vegetation, a generally drier climate, and extended source regions due to a lower sea level. In particular, in southern South America extended source regions contribute more than 80 % to the dust emissions during the LGM (Table 4.4). The findings are in agreement with results by Wolff et al. (2010), who suggested that the variability in the non-sea-salt calcium flux (as an elemental marker for terrestrial dust most likely originating from South America) on glacial–interglacial timescales found in Antarctic ice cores was caused by changes in the source region rather than by changes in atmospheric particle lifetime.

#### 4. Glacial Dust Changes in the Southern Hemisphere

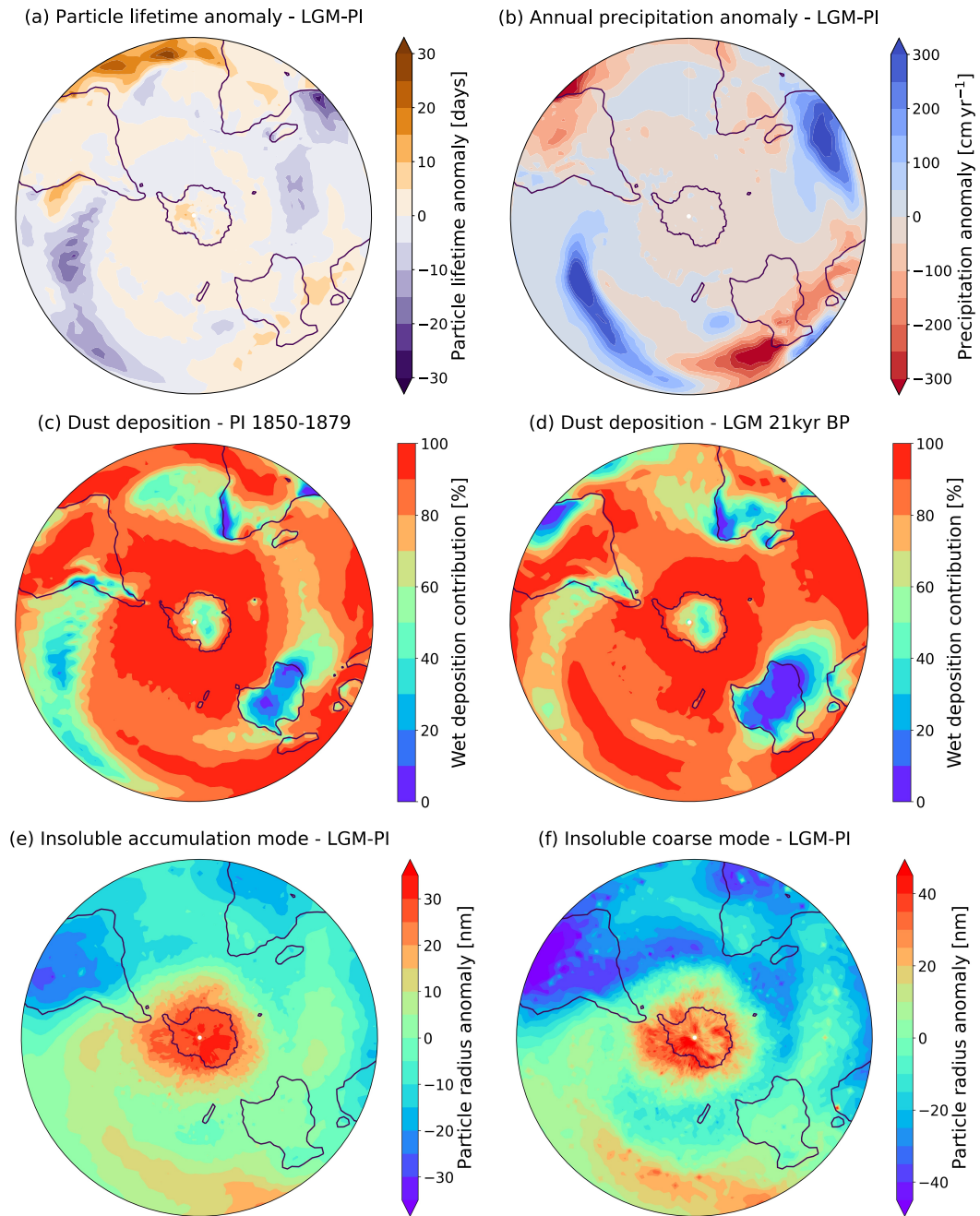


**Figure 4.5.** Particle lifetime anomalies (LGM-PI) (in d) **(a)**, annual precipitation anomalies (in  $\text{cm yr}^{-1}$ ) **(b)**, and the contribution of wet deposition to the total deposition (in percent) for both the PI **(c)** and LGM **(d)** in the SH. Additionally, particle radius anomalies (in nm) are shown for the insoluble accumulation **(e)** and insoluble coarse mode **(f)**. [Figure taken from Krättschmer et al. (2022)]

Finally, particle size anomalies between the LGM and the PI in the SH are investigated. Here, the focus is only on the insoluble modes, since the model assumes perfectly internally mixed soluble modes, and thus the according particles do not consist of only mineral dust. The simulations show a clear trend of increasingly

coarser particles for both the accumulation and the coarse mode in the SH between the source areas and the South Pole (Fig. 4.5e and f). Additionally, the results suggest a correlation between coarser particles and increased particle lifetimes and reduced precipitation (Fig. 4.5a and b).

The observed size variability between cold and warm climate states has been used to draw conclusions about meteorological conditions. On the one hand, the analysis of mineral dust retrieved from marine sediments (Hovan et al., 1991) and Greenland ice cores (Steffensen, 1997) consistently showed the deposition of coarser dust particles during glacials, which has been interpreted as either being consequence of stronger winds or the result of decreased weathering (Mahowald et al., 2014). On the other hand, dust retrieved from Antarctic ice cores shows spatially varying and opposing trends with respect to particle sizes during cold climates. For instance, a particle size analysis of mineral dust retrieved from the EPICA-Dome C (EDC) ice core (75°06' S, 123°21' E) indicates the deposition of finer particles during the LGM compared to deposition occurring during the warmer climate of the Holocene (10 ka), while the same analysis for an ice core drilled at the Dome B (DB) location (77°05' S, 106°48' E) yields the deposition of coarser particles during the LGM compared to the Holocene (Delmonte et al., 2004). Since the mineralogical analysis of the dust particles clearly shows that the isotopic ratios match southern South American sources for both locations, it can be concluded that the deposited dust was of the same geographical provenance. Consequently, the observed differences are assumed to be caused by changes in the atmospheric circulation. As coarser particles tendentially have a shorter particle lifetime, those found at DB during the LGM are likely the result of shorter trajectories, while the finer particles and the increased sorting of the particles, expressed by a comparably small  $\sigma$  found for the LGM (Delmonte et al., 2002), indicate longer pathways from the source to the deposition area. The relative increase of finer particles in the EDC region during the LGM has also been confirmed by modeling studies (e.g. Mahowald et al. (2006)). The model used by Albani et al. (2012) also showed the deposition of slightly coarser particles in regions of East Antarctica and a shift to generally finer particles in most other regions of Antarctica during the LGM, as indicated by ice core data (Delmonte et al., 2002, 2004). The authors explain the regional variation in particle size, on the one hand, by reduced wet deposition during transport, which leads to the general shift to finer particles, and suggest, on the other hand, that size-selective dry deposition dominates in the interior of Antarctica, which in turn leads to the regional deposition of slightly coarser particles. The model results

support the suggested spatial variation in the respective predominant deposition mechanisms (Fig. 4.5e and f). Similar opposing dust grain size trends over glacial-interglacial timescales have also been found in marine sediments retrieved from the South Pacific and South Atlantic (van der Does et al., 2021).

The findings of generally coarser particles for both the accumulation and the coarse mode in the SH between the source areas and the South Pole without any remarkable regional differences contradict the previous discussion. For technical reasons, the mass median radius and the standard deviation of the particle size distribution in the scope of the dust emission process are both fixed parameters in the model for both the insoluble accumulation and the insoluble coarse mode (see Sect. 3.2.1 and Stier et al. (2005)). Consequently, the emission of coarser particles during the LGM due to stronger winds in the source regions must be excluded. Since the standard deviation of the particle size distributions are kept constant for all modes, HAM2.3 also does not account for features like a more efficient particle sorting due to longer particle lifetimes as discussed above. The only mechanism in the model leading to increased particle sizes is the coagulation of insoluble dust particles with sulfuric acid particles of much smaller size (Vignati et al., 2004). Consequently, the observed particle size anomalies in the SH during the LGM compared to the PI shown in Fig. 4.5e and f can be attributed to an increased sulfur coating of the insoluble dust particles as a consequence of the longer particle lifetimes (Fig. 4.5a) due to reduced precipitation (Fig. 4.5b). These findings were tested by running the same simulation while switching off all sulfate sources, and the observed particle radius anomalies did indeed vanish.

##### 4.3.2.5 MERIDIONAL DUST TRANSPORT IN THE SH DURING PI AND LGM

Although the particle size distribution implemented in HAM2.3 does not allow for the investigation of sizedependent processes within a given mode during transport, general transport patterns on larger scales can still be studied. Here, the meridional transport from the source areas in the SH towards the South Pole is of particular interest. As a consequence of the Coriolis force, southward-moving air parcels carrying mineral dust are generally deviated eastwards, leading predominantly to a zonal transport and distribution of dust by the westerlies, whereas the meridional transport is caused by eddies (Li et al., 2010). Figure 4.6 shows the zonally averaged dust mass concentration depending on the altitude south of 30° S for both the PI (Fig. 4.6a and b) and the LGM (Fig. 4.6c and d), as well as the mean dust transport height for all modes and times (Fig. 4.6e). The general meridional

#### 4. Glacial Dust Changes in the Southern Hemisphere

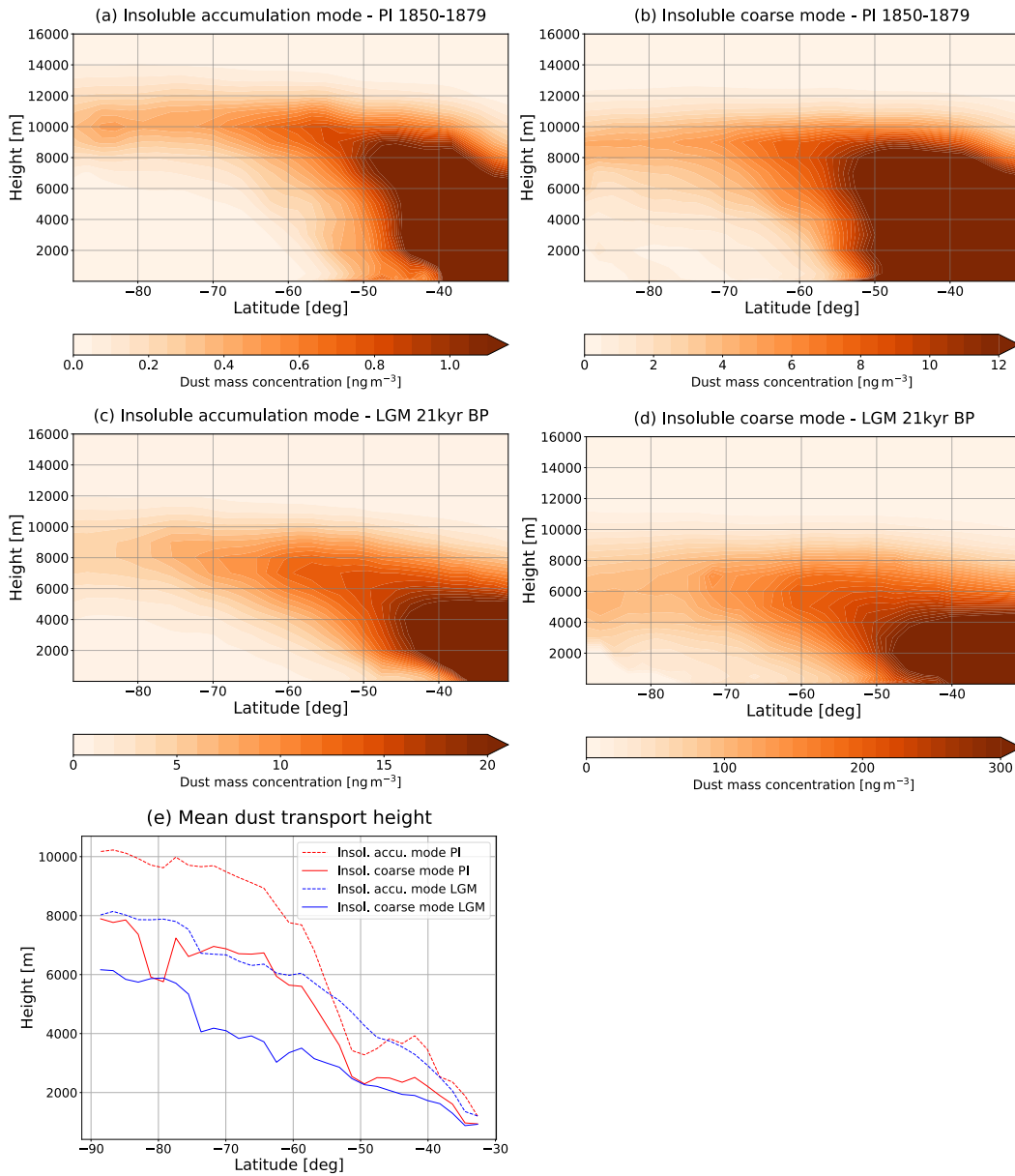


**Figure 4.6.** Zonally averaged dust concentration depending on the altitude for the insoluble accumulation and coarse mode between 30 and 90° S during the PI **(a, b)** and LGM **(c, d)**. The mean transport height for all modes and simulation periods **(e)**. [Figure taken from Krätschmer et al. (2022)]

dust transport pathway can be understood as a result of prevailing convective cells. After their emission in the mid-latitudes and low latitudes, dust particles are transported to the mid-troposphere and high troposphere (and potentially even higher to the tropopause; see below) along the polar front, i.e. the boundary between the Ferrel and the polar cell, by convection. While removal processes like sedimentation and dry deposition take place close to the ground, dust particles transported in the troposphere are mostly removed by wet scavenging. Dust particles trans-

ported at higher altitudes, however, remain significantly longer in the atmosphere and can only get removed once they reach lower altitudes as a consequence of the convergence and subsequent sinking of cold air masses (so-called subsidence) close to the South Pole (James, 1989). As can be clearly recognized in Fig. 4.6 for both the PI and the LGM, the finer particles of the accumulation mode are transported at higher altitudes compared to particles in the coarse mode. This effect is caused by the higher sedimentation velocities of larger particles and has also been found in other studies (Tegen and Fung, 1994). Delmonte et al. (2004) used this insight in order to explain the differences in dust grain size at DB and EDC during the LGM (see above) despite their geographical proximity and same dust provenance. The authors suggest that the measured difference in particle size and grading (i.e. low  $\sigma$ ) are caused by finer particles being transported on longer trajectories in the upper atmosphere and deposited in regions of air subsidence, whereas coarse particles were transported to the respective deposition areas by comparably short trajectories in the troposphere. This opposing temporal trend with respect to the measured particle size of dust deposited at DB and EDC during the LGM–Holocene transition is proposed to be the result of vortex migration, i.e. the southwards movement of an area of preferential upper-air subsidence on the corresponding timescale (Delmonte et al., 2004).

While differences in transport height between particles of the accumulation and the coarse mode can be observed for a given time period, obvious differences also exist with respect to transport height between the PI and the LGM for a given mode. During the PI, the majority of dust particles in the accumulation (Fig. 4.6a) and the coarse mode (Fig. 4.6b) seem to get transported quickly by convection from the source regions to a typical altitude of 11 and 9 km, respectively, at around 50° S and then follow a rather meridional pathway southward mostly at the same altitude. The southwards-directed meridional transport of mineral dust during the LGM, however, does not exhibit such clear vertical and horizontal patterns. Instead, the altitude seems to increase continuously during the southward transport, reaching a maximum of around 8 and 6 km for the accumulation (Fig. 4.6c) and the coarse mode (Fig. 4.6d), respectively. The obtained difference in mean transport height (Fig. 4.6e) between the PI and the LGM can be attributed to reduced vertical mixing and advection as a consequence of colder surfaces (Fig. 4.2a and b), leading to a higher dust concentration at lower levels (Albani et al., 2012). These results suggest that the polar cell was vertically less extended during the LGM compared to the warmer PI climate.

#### 4.4. CONCLUSIONS

ECHAM6.3-HAM2.3 constitutes a state-of-the-art model providing an interactive coupling of mineral dust emissions to the atmospheric model depending on surface properties and meteorological factors. For present-day conditions, the model yields reasonable results for dust emission, burden, and deposition close to the median of other studies performed in the scope of the global dust model intercomparison in AeroCom phase I. Generally, the model performs at the lower end of the 1000 Tg yr<sup>-1</sup> to 4000 Tg yr<sup>-1</sup> range of dust emissions estimated by the IPCC, which is caused by the neglect of a super-coarse particle mode. The predominant representation of fine and coarse particles leads to slightly higher particle lifetimes, which in turn enables the long-range transport of mineral dust to remote regions and causes wet scavenging to become the most dominant deposition mechanism in the model.

For pre-industrial climate conditions, a comparison to other modeling studies and measurement data suggests that in absolute numbers, the simulated dust emissions and depositions are too low, particularly in the SH. The discrepancy is greatest in the South Pacific, suggesting that the dust source strength of Australia is underestimated in the model. However, since the simulated dust deposition in the Tasman Sea and over Antarctica are in good agreement with and slightly higher than the observational data, respectively, this model–data mismatch cannot be easily explained by a sole model source strength deficit, and non-aeolian contributions not considered in the model might play a crucial role. For LGM climate conditions, the simulated dust deposition fluxes agree well with measurement data. As a consequence of the underestimation of the dust cycle during PI, the corresponding simulated globally averaged LGM to PI ratio with respect to dust depositions of 5.6 is slightly above the 2 to 5 suggested based on measurement data. A regional analysis in the SH shows that the increase in dust emissions of the major sources of southern South America, southern Africa, and Australia during the LGM can be attributed to a generally drier climate causing less precipitation (except over Patagonia), extended source regions due to a lower sea level, and significantly stronger winds in the source regions combined with reduced vegetation.

The dust provenance studies indicate that over 90 % of the dust deposited between 30 and 90° S is either of Australian or South American origin for both the PI and LGM climate conditions. However, the model suggests that Australia constituted the predominant source of dust deposited over Antarctica during the LGM. This result is inconsistent with several data studies suggesting based on isotope analysis that most of the dust deposited over Antarctica during the LGM is most

likely of southern South American origin and clearly indicates a shortcoming on the modeling side. Although both the South American and Australian sources show an almost equal increase in strength during the LGM compared to the PI in the model, the relative contribution of South America decreases. This can be traced back to an average increase in particle lifetime of Australian dust during the LGM, whereas the average particle lifetime of South American dust decreases due to changes in regional precipitation pattern. Despite a slight increase in particle lifetime in the SH during the LGM due to the generally drier climate, the almost 16-fold source strength increase of the contributions of southern South America and Australia during the LGM compared to the PI seems to be necessary in order to achieve a on average 14-fold increase in dust deposition over Antarctica in the simulations, which is in good accordance with observational data.

For both the PI and LGM, the finer particles in the accumulation mode are transported at greater altitudes than coarse mode particles within the Southern Hemispheric troposphere due to lower sedimentation velocities. Additionally, both modes exhibit a clear trend of being transported at lower altitudes during the LGM, which can be explained by reduced convection due to colder surfaces and indicate that the Polar cell was vertically less extended during the LGM.

This study clearly showed the capabilities and limitations of ECHAM6.3-HAM2.3. Specifically, microphysical effects can only be studied to some degree since all particles within a given mode are assumed to have the same physical and chemical properties. Since SSTs influence precipitation patterns and other climate elements like wind speed, which in turn affect the dust emission process, prescribing different boundary conditions based on reconstructions suggesting cooler SSTs might turn out to be a useful approach to reduce the data-model discrepancy, particularly in regard to the provenance of dust deposited over Antarctica during the LGM. Future sensitivity studies might yield new insights into this matter.



"The long summer was over. For ages a tropical climate had prevailed over a great part of the Earth, and animals whose home is now beneath the Equator roamed over the world from the far South to the very borders of the Arctics ... But their reign was over. A sudden intense winter, that was also to last for ages, fell upon our globe."

---

(Louis Agassiz, *Geological Sketches*)

## 5. GLACIAL SST CONUNDRUM NOT RESOLVED: A MODELING PERSPECTIVE

### 5.1. THE IMPORTANCE OF A PROPER SST RECONSTRUCTION FOR THE LGM

The LGM was characterized by a climate much colder than at present, mainly due to a strong reduction in atmospheric greenhouse gas concentrations and a increased albedo as a consequence of enlarged ice cover in high latitudes (Schneider von Deimling et al., 2006). Since the surface temperature differ between the LGM and the pre-industrial period (PI), the LGM offers a opportunity to derive independent estimates of Earth's equilibrium climate sensitivity, i.e. the long-term increase in global mean temperature after a doubling of the atmospheric CO<sub>2</sub> concentration (Hoffert and Covey, 1992; Schmittner et al., 2011). This effort requires proper data-model comparisons and correct reconstructions of surface temperatures. The first global reconstruction of glacial sea surface temperatures (SST) was performed in the late 1970s in the scope of the Climate: Long range Investigation, Mapping, and Prediction (CLIMAP) project (CLIMAP PROJECT MEMBERS, 1976), and the question concerning the glacial temperature drop remains controversial. The CLIMAP reconstructions suggest globally a comparably weak cooling by  $(3.0 \pm 0.6)^\circ\text{C}$  during the LGM, which results in a climate sensitivity of  $(2.0 \pm 0.5)^\circ\text{C}$  (Hoffert and Covey, 1992). This value is at the lower end of the 1.8 to 5.6 $^\circ\text{C}$  interval (mean  $(3.7 \pm 1.1)^\circ\text{C}$ ) derived from the latest-generation climate model ensemble used in the scope of the sixth Coupled Model Intercomparison Project (CMIP6) (Meehl et al., 2020). Based on the transfer function method using data from three planktonic groups preserved in deep sea sediments, the average cooling of the tropical SST are proposed to be only around 1-2 $^\circ\text{C}$ , with even a warming in

some subtropical gyres. While climate models are generally able to reproduce the changes in SST during the LGM averaged over the tropical ocean basin suggested by data (Braconnot et al., 2007), several complex models were not able to reproduce this particular feature (Waelbroeck et al., 2009). This indicates that either models are not yet able to capture important processes in the climate system, or that some of the applied methods to reconstruct the temperature have a systematic bias. However, the importance of a proper reconstruction of tropical SST during the LGM is emphasized by studies showing that the tropics have a substantial influence on the temperature and precipitation in the mid-latitudes (Lohmann and Lorenz, 2000), and that the climate sensitivity depends statistically significant on the tropical temperatures, resulting in a higher sensitivity in case of cooler LGM SSTs (Hargreaves et al., 2012; Yin and Battisti, 2001). Mix et al. (1999) suggested that the problem on the data side might be caused by the utilization of so-called no-analogue assemblages, i.e. species that do not exist today anymore and therefore are hard to interpret, for instance certain tropical Pacific foraminifera found in marine sediment cores.

A recent global SST reconstruction for the LGM is provided by Tierney et al. (2020). The authors use a data assimilation technique and cross-validate their results by simulations with an isotope-enabled climate model. Their data consist solely of geochemical proxies ( $U_{37}^{K'}$  from alkenones,  $TEX_{86}$  based on arachaeal isoprenoid tetraethers, Mg/Ca of planktic foraminifera and the water isotope  $\delta 18O$ ), taking into account seasonal bias and general proxy uncertainties. The approach excludes marine as well as terrestrial microfossils completely to avoid the no-analogues problem and the lack of Bayesian proxy-system models required in the scope of the data assimilation process. The final reconstruction suggests a mean global surface temperature reduction of  $-6.1^{\circ}C$ , with a 95 % probability for the interval from  $-5.7^{\circ}C$  to  $-6.5^{\circ}C$ . However, the authors emphasize that their result has no overlap with some other reconstructions, for instance the Glacial Ocean Map (GLOMAP), a global climatology of the ocean surface during the LGM mapped on a regular grid provided by Paul et al. (2021). Their study is based upon floral and faunal assemblages and several sea-ice reconstructions from the Multiproxy Approach for the Reconstruction of the Glacial Ocean Surface (MARGO, Waelbroeck et al. (2009)) project because those have the best spatial coverage available and enable potentially a seasonal reconstruction. The GLOMAP results suggest a global ocean cooling by  $(-1.7 \pm 0.1)^{\circ}C$  and a tropical ocean cooling by  $(-1.2 \pm 0.3)^{\circ}C$  for the LGM, but the authors state that their values might be too warm by  $0.5^{\circ}C$  to  $1.0^{\circ}C$

due to the effects of a heterogenous spatial sampling and uncertainties concerning the response of fossil foraminifera to changes in seasonality and the thermal structure of the upper ocean layer.

In this study, two SST reconstructions provided by Tierney et al. (2020) and Paul et al. (2021) are used to force an Atmospheric General Circulation Model (AGCM) including an aerosol model. The obtained results are assessed by comparing the simulated land surface temperature difference between LGM and PI to reconstructed data based on noble gases in groundwater provided by Seltzer et al. (2021), who suggest that the low-to-mid latitude land surface during the LGM cooled by  $(5.8 \pm 0.6)^\circ\text{C}$  and stated that their land temperatures are consistent with the SSTs of Tierney et al. (2020).

## 5.2. EXPERIMENTS AND EXPERIMENTAL SETUP

Simulations are performed for PI (1850-1879 CE) and LGM climate conditions with the horizontal spatial resolution T63, corresponding to  $1.875^\circ \times 1.875^\circ$ , and 47 vertical layers. For PI, a cold start is initialized with a spin-up time of 10 years, and for the LGM the simulations are initialized by restart files, which represent a dynamic equilibrium of the model obtained after several hundred simulation years, with a spin-up time of 20 years. More details on the setup can be found in Krättschmer et al. (2022). Each simulation is run for 50 years, and the assessment period covers the final 30 years of each simulation. The SST and sea ice boundary conditions prescribed in the atmosphere-only setup for PI are monthly-resolved values averaged for the years 1870-1899 and stem from the Program for Climate Model Diagnosis and Intercomparison (PCMDI) based on the latest AMIP II dataset [Durrack and Taylor (2019)]. For the LGM, the according reconstructions are used from Tierney et al. (2020) and GLOMAP (Paul et al., 2021). Since Tierney et al. (2020) do not provide a sea ice reconstruction, the one from GLOMAP is used to keep the LGM experiment setup as similar as possible in order to investigate the influence of the SST, only. Anthropogenic emissions of aerosols and aerosol precursor are only of importance for PI, and here monthly-resolved input files based on the Atmospheric Chemistry and Climate Model Intercomparison Project (ACCMIP) dataset (Lamarque et al., 2010) are prescribed. The orbital parameters, greenhouse gas concentrations and a glacier mask (GLAC-1D) for the LGM runs are set in accordance with the Paleoclimate Model Intercomparison Project – Phase 4 (PMIP4) experimental design (Kageyama et al., 2017). A glacial land-sea mask accounting for the approx. 125 m lower sea level is prescribed.

### 5.3. RESULTS AND DISCUSSION

The results focus solely on the simulated surface temperature difference  $\Delta T$  between LGM and PI for both prescribed sea surface temperature reconstructions.

#### 5.3.1. GLOBALLY AND ZONALLY SIMULATED SURFACE TEMPERATURE DIFFERENCE FOR GLOMAP AND TIERNEY SST

Figure 5.1 shows the zonally-averaged surface temperature (sea and land surface) for Tierney et al. (2020) (a) and GLOMAP SST (b). Since in both experiments the same glacier mask and sea ice reconstruction are prescribed, there is only little difference for the mid/high-latitudes. The most remarkable differences occur particularly in the latitudes  $45^{\circ}\text{N} - 45^{\circ}\text{S}$ . Globally, the experiments result in a cooling of  $-4.08^{\circ}\text{C}$  (GLOMAP SST), respectively,  $-6.12^{\circ}\text{C}$  (Tierney et al., 2020) of the surface temperature. Using GLOMAP SST, the total cooling in the low latitudes ( $30^{\circ}\text{N} - 30^{\circ}\text{S}$ ) averages to  $-1.28^{\circ}\text{C}$ , with a more pronounced cooling of the land surface ( $-2.07^{\circ}\text{C}$ ) than the sea surface ( $-0.98^{\circ}\text{C}$ ). A similar anomaly is also found if one focuses on the tropics ( $23.5^{\circ}\text{N} - 23.5^{\circ}\text{S}$ ), with a total cooling of  $-1.22^{\circ}\text{C}$ . However, even though the considered tropics region has less influence from the mid/high-latitudes, the sea surface temperature cooling is even slightly stronger ( $-1.0^{\circ}\text{C}$ ) than the average over the low latitudes between  $30^{\circ}\text{N}$  and  $30^{\circ}\text{S}$ . This difference is caused by the warm pools in the subtropical gyres, which are less extensive closer to the equator (see Fig. 5.2a). The use of Tierney et al. SST, on the other hand, results in a much stronger total cooling than the GLOMAP experiment, both in the low latitudes ( $-3.80^{\circ}\text{C}$ ) and also in the tropics ( $-3.71^{\circ}\text{C}$ ). Likewise, the land surface cooling by  $-4.59^{\circ}\text{C}$  ( $-4.43^{\circ}\text{C}$ ) at low latitudes (tropics) is more pronounced than the sea surface cooling of  $-3.50^{\circ}\text{C}$  ( $-3.46^{\circ}\text{C}$ ). All values are summarized in Table 5.1.

Both reconstructions, GLOMAP and Tierney et al. SST, suggest a stronger cooling during the LGM than the  $(3.0 \pm 0.6)^{\circ}\text{C}$  proposed by the CLIMAP reconstruction. The mean cooling simulated in the high northern latitudes by approx.  $10^{\circ}\text{C}$ , which is caused by the ice sheets covering large parts of northern Europe and North America, is in good accordance with other modeling studies (Cao et al., 2019; Romanova et al., 2006). Similarly, a comparably lower cooling simulated over Antarctica is supported by reconstructions (e.g. Buizert et al. (2019)). The zonal and regional differences are discussed in more detail section 3.2 with regard to the available data.

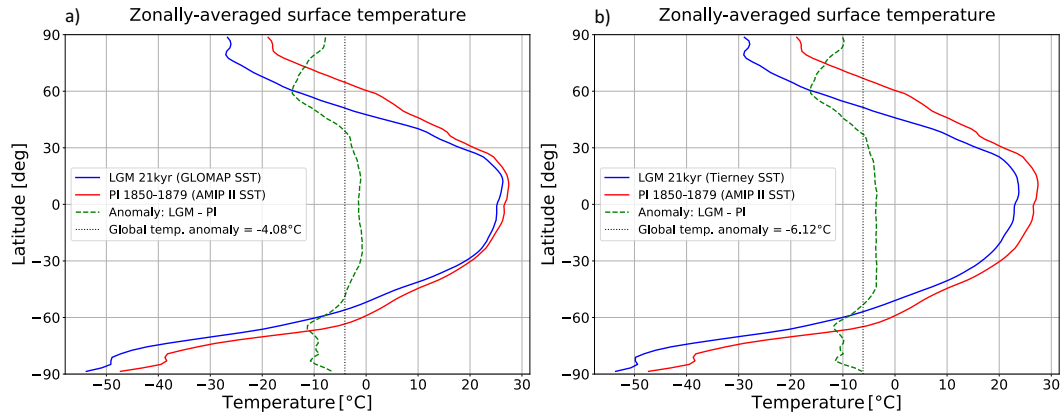


**Figure 5.1.** Zonally-averaged surface temperatures during the LGM for both GLOMAP (a) and Tierney SST (b) compared to PI (AMIP II SST). [Figure taken from Krätschmer et al. (2022b) (submitted)]

### 5.3.2. COMPARISON OF SIMULATED LAND SURFACE TEMPERATURE ANOMALY TO RECONSTRUCTED DATA

Figure 5.2 shows the comparison between the reconstructed land-surface temperatures by Seltzer et al. (2021) and the simulation results for GLOMAP and Tierney et al. SST in form of global maps (a, b) and scatterplots (c, d). The mean absolute deviation between simulated and observed temperature anomalies is 2.84 °C for GLOMAP, and 2.82 °C for Tierney et al..

The most remarkable differences in the simulated surface temperature anomaly occur in the low latitudes (Fig. 5.2a, b). GLOMAP SST show a comparably weak cooling in basically all low-latitude regions of the Pacific Ocean of less than -1°C, and also exhibit the controversial warming in subtropical gyres in the Pacific and the Atlantic Ocean. The weak low-latitude sea surface cooling leads to simulated land surface temperatures in the same range that are all too warm as compared to the reconstructions by Seltzer et al. (Fig. 5.2c). In this study, locations in regions within or very close to the low latitudes, i.e. South America, Africa and Australia / New Zealand, are grouped and compared to regions that are rather located in the mid-latitudes, like North America, Europe and Asia. The entire neotropical realm is only covered by one observation in the north-eastern part of South America. In contrast to simulation results using Tierney et al., the GLOMAP SST clearly underestimate the cooling here. This is not surprising considering that a previous study (Krätschmer et al., 2022), in which the comparably warm GLAMAP SST (a predecessor of GLOMAP, Paul and Schäfer-Neth (2003)) have been prescribed, it has been found that the JSBACH vegetation model simulates a desert in this region

## 5. Modelling Perspective on the Glacial SST Conundrum

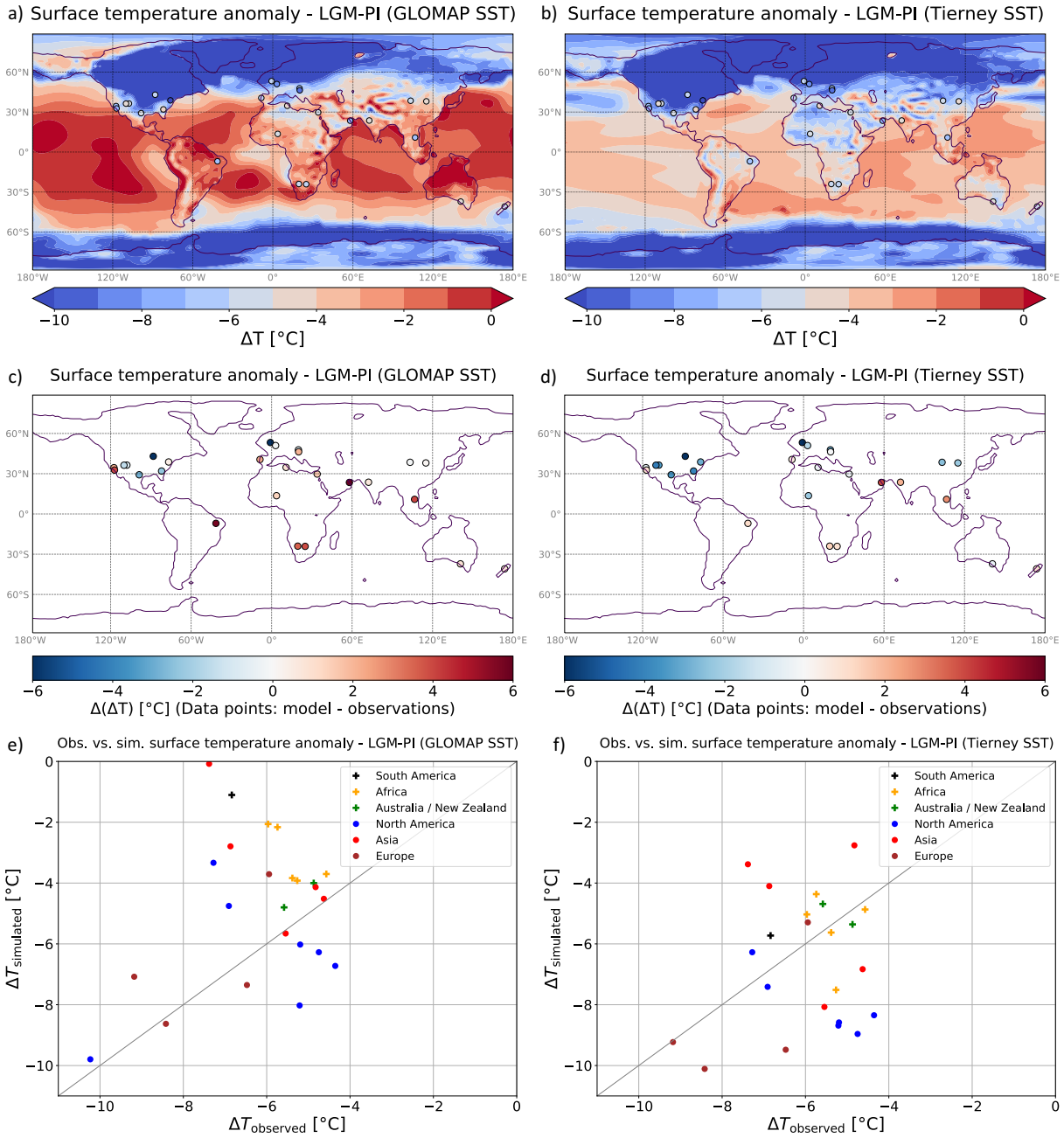


**Figure 5.2.** Comparison between the simulated surface temperature anomaly (LGM - PI) for GLOMAP (a, c, e) and Tierney SST (b, d, f) and reconstructed values based on noble gas concentrations in groundwater provided by Seltzer et al. (2021). For an easier readability, the difference between simulated and measured surface temperature anomaly  $\Delta(\Delta T)$  is additionally shown for the data points in c and d, indicating that the simulated temperature anomaly is higher ( $\Delta(\Delta T) > 0$ ) or lower ( $\Delta(\Delta T) < 0$ ) than suggested by the reconstructions. The data points in the scatterplots e and f are grouped into regions at low latitudes (pluses, South America, Africa, Australia / New Zealand) and regions predominantly in the mid-latitudes (circles, North America, Europe, Asia). [Figure taken from Krättschmer et al. (2022b) (submitted)]

## 5. Modelling Perspective on the Glacial SST Conundrum

| $\Delta T_{\text{LGM-PI}} [^{\circ}\text{C}]$ |              | GLOMAP SST | Tierney et al. SST |
|---|--------------|------------|--------------------|
| Global  |              | -4.08      | -6.12              |
| Low Latitudes<br>(30°N - 30°S)                | Total        | -1.28      | -3.80              |
|   | Sea Surface  | -0.98      | -3.50              |
|   | Land Surface | -2.07      | -4.59              |
| Tropics<br>(23.5°N - 23.5°S)                  | Total        | -1.22      | -3.71              |
|   | Sea Surface  | -1.00      | -3.46              |
|   | Land Surface | -1.83      | -4.43              |

**Table 5.1.** Globally and regionally simulated cooling between LGM and PI averaged over the total, sea and land surface for GLOMAP and Tierney et al. SSTs. [Table taken from Krätschmer et al. (2022b) (*submitted*)]

due to high temperatures and strongly reduced precipitation. However, the drier climate simulated in this region is also supported by pollen and plant macrofossil data, which show that the plant-available moisture was strongly reduced during the LGM compared to present day (Farrera et al., 1999). The study by Farrera et al. (1999) also proposes a cooling by  $-5^{\circ}\text{C}$  to  $-6^{\circ}\text{C}$  for neotropical sites, which is much stronger than supported by the simulations using GLOMAP SST, but in good agreement with results of the Tierney SST experiment (Fig. 5.2b). Though, the authors state that data from West and South Pacific sites suggest only a reduced LGM sea level cooling by  $-1^{\circ}\text{C}$ . This indicates that the CLIMAP-like SST anomalies, i.e. the warmer pools in the subtropical gyres, might actually be realistic and thus this data also partly support the GLOMAP SST reconstructions. The land surface temperature reconstruction from Vietnam provided by Seltzer et al. (2021) is colder than the simulation results for both SST reconstructions, and closer to Tierney et al. SST.

However, low-elevation records from Indonesia and Papua New Guinea provided by Farrera et al. (1999) suggest again only a weak cooling by  $-1^{\circ}\text{C}$  to  $-2^{\circ}\text{C}$ , supporting both GLOMAP and Tierney et al. SST. Similarly, LGM temperature changes in Australia and New Zealand are in both experiments in accordance with the two observational records, but the low data coverage does not allow for any further insights. The agreement between simulation results and observations for the African continent is generally good for Tierney SST (Fig. 5.2f). GLOMAP SST, on the other hand, simulated systematically too warm land surface temperatures here, espe-

cially in South Africa (Fig. 5.2e). A TEX<sub>86</sub> proxy record from Lake Malawi in East Africa indicates a 3.5°C cooling during the LGM, which is also in better accordance with Tierney et al. SST (Powers et al., 2005). In North America and Europe, along the margins of the Laurentide and Fennoscandian ice sheet, as well as two regions in mid-latitude Asia, Tierney et al. SST result systematically in too cold land surface temperatures (Fig. 5.2b, d, f). The simulation results obtained by using GLOMAP are, on the other hand, in better accordance with the reconstructed data, particularly in some locations in western North America. Here, the simulated lower cooling compared to Tierney et al. might be caused by changes in the atmospheric circulation due to the Laurentide ice sheets. Bartlein et al. (2011) suggested that a potential warming in Alaska during the LGM might have been caused by warm air advectively transported from the south. Romanova et al. (2006) found that the changes of the orography and albedo caused by the Laurentide Ice Sheet induce strong temperature changes of about 16°C north of 30°N, and much smaller changes elsewhere. These temperature changes are found to be non-linearly related to ice sheet height with regional heterogeneities (Meyer et al., 2017; Romanova et al., 2006; Wang et al., 2021).

#### 5.4. CONCLUSIONS

The comparison of the obtained simulation results using both Tierney SST and GLOMAP SST give no clear indication which reconstruction results in better-fitting land surface temperatures. The warmer GLOMAP SST lead to simulated land surface temperatures which are tendentially too warm at low-latitudes, like South America, Africa, Australia / New Zealand and parts of Asia. However, particularly at mid-latitudes close to the margins of the ice sheets over North America and Europe, they lead to consistent results, whereas the colder counterpart, the simulation based on Tierney et al. SSTs, causes tendentially a too pronounced cooling in this region. However, Tierney et al. SST lead to a good accordance between the simulation results and observations in low-latitude regions like South Africa, Africa and Australia / New Zealand, and are also regionally supported by other data studies (Farrera et al., 1999; Powers et al., 2005). From the data side, a higher low-elevation coverage obtained by using the same reconstruction method in some regions, particularly the neotropical realm and Australia / New Zealand, would be desirable.

As a logical next step, systematic analyses on different processes shall be performed in order to elaborate their relative importance for land and ocean surface

temperatures for glacial climates. Even though the LGM is one of the most frequently simulated time slices in paleoclimate modeling and belongs to the standard PMIP paleoclimate model experiments (Braconnot et al., 2012; Kageyama et al., 2021) a consistent view of the marine and terrestrial reconstructions is still lacking. In order to estimate the Earth's climate sensitivity based on simulations, the models have to represent several feedback mechanisms in the climate system correctly. In the tropics, which are particularly important for the global climate due to their large spatial extent, relevant mechanisms include the cloud feedback and the water vapor – lapse rate feedback (Bony et al., 2006). A reconstruction of high elevation temperatures from Mount Kenya, East Africa, indicate that the lapse rate steepened substantially during the LGM compared to present day, and a comparison with simulation results show that this lapse rate change is still underestimated by models (Loomis et al., 2017). As pointed out by Seltzer et al. (2021), the lapse rate is critical for a comparison between simulated and reconstructed SSTs and LSTs, respectively, since the 125 m lower sea level leads might also lead to an additional temperature change. Another source of uncertainty are the model resolution and the parameterization of physical processes on the sub-grid scale. Model results with increased grid resolution demonstrate more realistic climate simulations due to the higher number and improved representation of climate processes and phenomena in the model (Lohmann et al., 2021; Roeckner et al., 2006). While the model used in this study, for instance, accounts for changes in terrestrial albedo due to variations in vegetation type and cover, other studies also indicate a substantial influence of variations in soil albedo on simulated LSTs, which might result in an additional global cooling by 1.07°C during the LGM (Stärz et al., 2016). Since the resulting LSTs could depend on the model (Kageyama et al., 2021), the formulation of land surface parameters for soil (Stärz et al., 2016), or even the resolution of the same model (Dong and Valdes, 2000; Lohmann et al., 2021), other research groups are highly encouraged to also force their AGCMs with the two different SST reconstructions used here, in order to arrive at an improved understanding of glacial surface temperatures.



"This sense of instability is reinforced when we look within the last ice age at shorter-term climate fluctuations. There were repeated, incredibly rapid climate changes that were at least hemispheric in the extent of their impacts. As the last ice age ended, our record of these abrupt climate changes comes into sharper focus, revealing that warming of up to 10°C in Greenland has occurred within less than a decade. This reinforces the idea that the present climate system is unusually unstable - at least on relatively short timescales - providing an important backdrop for thinking about our own planet-changing activities as a species."

---

(Tim Lenton, *Earth System Science: A Very Short Introduction*)

## 6. USING MINERAL DUST TO OBTAIN INSIGHTS ON THE SOUTH.-HEM. ATMOSPHERIC DYNAMICS DURING THE LGM FOR DIFFERENT SSTs

### 6.1. THE ROLE OF THE ATMOSPHERIC CIRCULATION FOR LGM CLIMATE

Ice core records from Greenland and Antarctica indicate an increase in mineral dust deposition during the LGM by a factor of 80, respectively, 15 in these regions compared to the Holocene (Fischer et al., 2007). The isotopic fingerprint, i.e. the isotope ratios  $^{87}\text{Sr}/^{86}\text{Sr}$ ,  $^{143}\text{Nd}/^{144}\text{Nd}$  and  $^{206,207,208}\text{Pb}/^{204}\text{Pb}$ , of dust particles in the Greenland Ice Sheet Project 2 (GISP2) ice core samples retrieved at Summit Station (72°34'N, 38°27'W) suggests eastern Asia as the main source region for dust deposited over Greenland during the LGM (Biscaye et al., 1997). In the Southern Hemisphere (SH), isotope analysis of dust particles contained in ice core samples from the European Project for Ice Coring in Antarctica at Dome C (EDC; 75°06'S, 123°21'E) suggests Patagonia to be the main source region (up to 85 %) of dust deposited over Antarctica during the LGM, possibly with minor contributions from South Africa and Australia (Basile et al., 1997; Delmonte et al., 2008). This finding is also supported by modelling studies (Lunt and Valdes, 2001, 2002; Albani et al., 2012). Since mineral dust is mainly emitted in arid and semi-arid areas and controlled by several factors, including wind speed in the boundary layer, soil

moisture, type and amount of vegetation as well as other non-erodible surface elements (Goudie, 2008), the observed changes in mineral dust deposition during the LGM have mostly been attributed to a source strength increase as a consequence of higher wind speeds, a generally drier climate because of the lower temperatures and more extended source regions due to reduced vegetation cover and a lower sea level (Lunt and Valdes, 2002; McGee et al., 2010; Wolff et al., 2010). However, general atmospheric changes are also being considered to have played a crucial role, for instance shifts in the westerlies or changes in the precipitation patterns, which in turn would affect transport pathways and particle lifetimes (Toggweiler et al., 2006; Fischer et al., 2007). The results are ambiguous though. A data-synthesis by Kohfeld et al. (2013) indicates that paleo-data for terrestrial moisture, dust deposition, ocean productivity and sea surface temperatures (SST) during the LGM would support several hypothesis' concerning the southern-hemispheric westerlies, like a equatorward shift, a strengthening, or no change at all. The rapid changes from high atmospheric dust concentrations during cold periods to low concentrations during Dansgaard-Oeschger events found in the Greenland Ice Core Project (GRIP) ice core have been interpreted to indicate substantial wind speed changes in the source regions and possibly in the atmospheric particle lifetime rather than environmental changes in the source regions (Fuhrer et al., 1999). Modelling studies demonstrate the importance of precipitation patterns due to their influence on particle lifetimes, particularly over the Southern Ocean (SO), where more than 90 % of all dust removal occurs due to wet deposition (Markle et al., 2018; Krätschmer et al., 2022). The prescription of proper LGM boundary conditions in terms of SSTs in atmosphere-only modelling setups has been investigated in several studies, showing that tropical SST patterns have a large influence on the midlatitude circulation and indicating that changes in the SSTs in general, together with changes in the ice sheet topography, were mostly responsible for the according climate changes, and thus precipitation, during the LGM (Yin and Battisti, 2001; Tharammal et al., 2013).

Insights on the strength, shape and position of the westerlies during the LGM are considered crucial in order to understand the role of the air-sea gas exchange and the substantial atmospheric CO<sub>2</sub> reduction from 280 ppm during the last interglacial to around 190 ppm during the LGM. While dust-induced iron fertilization in the SO might have played a crucial role (see Sec. 2.2.3; Martin (1990)), the westerlies during the LGM are also assumed to have been of great importance. However, the persisting uncertainties in terms of correct SSTs and sea ice concentration

(SIC) have led to contrary results concerning their position and strength in modelling studies (Wolff et al., 2010). Simulations with coupled Atmosphere-Ocean models, for instance, have suggested equatorwards shifts (Williams and Bryan, 2006), poleward shifts (Shin et al., 2003) or even no changes at all in strength and latitudinal position (Otto-Bliesner et al., 2006). Toggweiler et al. (2006) suggested a substantial equatorward shift during the LGM, which would result in less upwelling of deep water around Antarctica, since this is mainly forced by the strong westerlies over the Antarctic Circumpolar Current (Wyrski, 1961; Gordon, 1971). This would lead to a substantial accumulation of CO<sub>2</sub> below a ventilation depth of 2500 m (Toggweiler, 1999; Toggweiler et al., 2006), and might explain the important role of the Ocean for LGM climate as discussed in Sec. 2.1.3. Since mineral dust emission and transport depends strongly on atmospheric circulation patterns, its utilization as a climate proxy in simulations might be a useful approach in order to get further insights on atmospheric conditions during the LGM. In turn, this approach might help to tighten the constraints for proper SST and SIC reconstructions for the LGM, and enables the investigation of other important effects of mineral dust. The direct radiative effects of aeolian mineral dust might have also played a crucial role during past climate changes, e.g. during the deglaciation at the LGM-Holocene transition. Modelling studies suggest that the high dust load in the high northern-hemispheric latitudes during the LGM might have had a net-warming effect on surface temperatures. The substantial dust load reduction due to the global warming during the deglaciation and the increasing hydrological cycle might have resulted in a cooling over arctic regions, which in turn would have reduced the warming rate (Albani and Mahowald, 2019).

In this study, ECHAM6.3-HAM2.3 is used in order to investigate the influence of two different SST datasets on the simulated dust cycle during the LGM and the atmospheric circulation in general. As discussed in Chapter 5, both SST datasets suggest a very different global and regional cooling since they were reconstructed based on different methods. The focus is particularly on the SH. The simulated total dust deposition in the SH is compared to observational data and simulated differences in the dust budget are explained, considering the impact of the respective SST dataset on wind speed, vegetation and precipitation. An index for the “waviness” of the zonal circulation yields further insights on circulation patterns and the vertical structure of the atmosphere. Finally, the simulation results are evaluated with regards to the strength, position and meridional shape of the westerlies in the SH and their relation to the prescribed SSTs during the LGM compared

to pre-industrial conditions.

## 6.2. EXPERIMENTS AND EXPERIMENTAL SETUP

Simulations are performed for pre-industrial (PI, 1850-1880 CE) and LGM (21 kyr BP) climate conditions with a horizontal spatial resolution of T63 ( $1.875^\circ \times 1.875^\circ$ ) and 47 vertical layers. All simulations are run for 40 years, but only the final 30 years are used for the evaluation in order to account for the spin-up time. For PI, a cold start is performed, and the LGM simulations are initialized by restart files representing a dynamic equilibrium of the model obtained after several hundred years of simulation. We prescribe boundary conditions in terms of SSTs and SIC. For PI, monthly-resolved means for the years 1870-1899 from the Program for Climate Model Diagnosis and Intercomparison (PCMDI) based on the AMIP II dataset (Durack and Taylor, 2019) are used. For the LGM runs, two different SST datasets are used, one provided by (Tierney et al., 2020) and created based on geochemical proxies and a novel data assimilation technique, and the other based on floral and faunal assemblages from the Multiproxy Approach for the Reconstruction of the Glacial Ocean Surface (MARGO, Waelbroeck et al. (2009)) in form of the Glacial Ocean Map (GLOMAP) provided by Paul et al. (2021). Since the SST dataset by Tierney et al. does not come with a SIC reconstruction, in all LGM experiments the dataset provided by GLOMAP is used. Orbital parameters, greenhouse gas concentrations and the glacier mask (GLAC-1D) for the LGM runs have been set in accordance with the experimental setup of the Paleoclimate Model Intercomparison Project - Phase 4 (PMIP4) (Kageyama et al., 2017). For the PI runs, the monthly-resolved input files for the emission of aerosols and aerosol precursors from anthropogenic sectors originate from the Atmospheric Chemistry and Climate Model Intercomparison Project (ACCMIP) (Lamarque et al., 2010). Simulations including all dust sources provide monthly-resolved output, and the provenance studies (PAT only, AUS only) have been set to daily output in order to capture the short timescales of the atmosphere. A proper land-sea mask accounts for the lower sea level during the LGM.

### 6.3. RESULTS AND DISCUSSION

#### 6.3.1. MINERAL DUST BUDGET FOR GLOMAP AND TIERNEY ET AL. SSTs

The SST anomaly between LGM and PI is shown in Fig. 6.1a (GLOMAP) and b (Tierney et al.). GLOMAP SSTs indicate a warming compared to PI in some subtropical gyres in the Pacific and South Atlantic and suggest generally a weaker global cooling ( $-4.08^{\circ}\text{C}$ , see Chapter 5) than Tierney et al SSTs ( $-6.12^{\circ}\text{C}$ , see Chapter 5). The simulated annual, global dust emissions are 4538 Tg (GLOMAP) and 5197 Tg (Tierney et al.), respectively. Table 6.1 provides global and regional dust emission values, indicating that differences in the dust budget in the SH between GLOMAP and Tierney et al. SST are caused by variations in the increased source strength of Australia and Patagonia during the LGM. The figures 6.1c and d suggest a much stronger contribution of Patagonian dust to the total dust deposition in the SH with Tierney et al. SSTs (d) compared to GLOMAP SSTs (c), particularly over Antarctica. The total dust deposition fluxes in the SH shown in Figs. 6.1e and f exhibit similar patterns, but indicate in accordance with the lower dust emissions shown in Tab. 6.1 also generally lower dust depositions for Tierney et al. SSTs. While the comparison to observational data by Kohfeld et al. (2013) shows a generally good agreement in the Atlantic Ocean, the simulated dust deposition fluxes are overestimated in the Tasman Sea and over Antarctica for both GLOMAP and Tierney et al. SSTs (Fig. 6.1e, f, g and h). Both SST datasets lead to an underestimation of the dust deposition in the Pacific and Pacific SO, respectively. However, it is more pronounced for Tierney et al. SSTs.

Figures 6.2a and b show the desert fraction, i.e. areas not covered by any vegetation and therefore potential dust emission areas, in the SH. GLOMAP SSTs result in more vegetation in Patagonia compared to Tierney et al. SSTs during the LGM, and vice versa in Australia. The precipitation anomaly patterns (LGM-PI) shown in Figs. 6.2c for GLOMAP SSTs exhibit particularly over the Pacific Ocean distinct regions of strongly increased precipitation in comparison to Tierney et al. SSTs (Fig. 6.2d). Additionally, the maps and Tab. 6.2 suggest a wetter climate in Patagonia during the LGM with GLOMAP SSTs than during PI compared to Tierney et al. SSTs. Both SST datasets result in drier conditions in Australia during the LGM compared to PI. The 10 m wind speed anomalies shown in Fig. 6.2e show that GLOMAP SSTs result in higher wind speeds in the mid- and high-latitude regions and reduced wind speeds in the subtropical regions over the Pacific compared to Tierney et al. SSTs (Fig. 6.2f). Particularly over Australia, GLOMAP SSTs lead to

## 6. Southern-Hemispheric Atmospheric Dynamics During the LGM

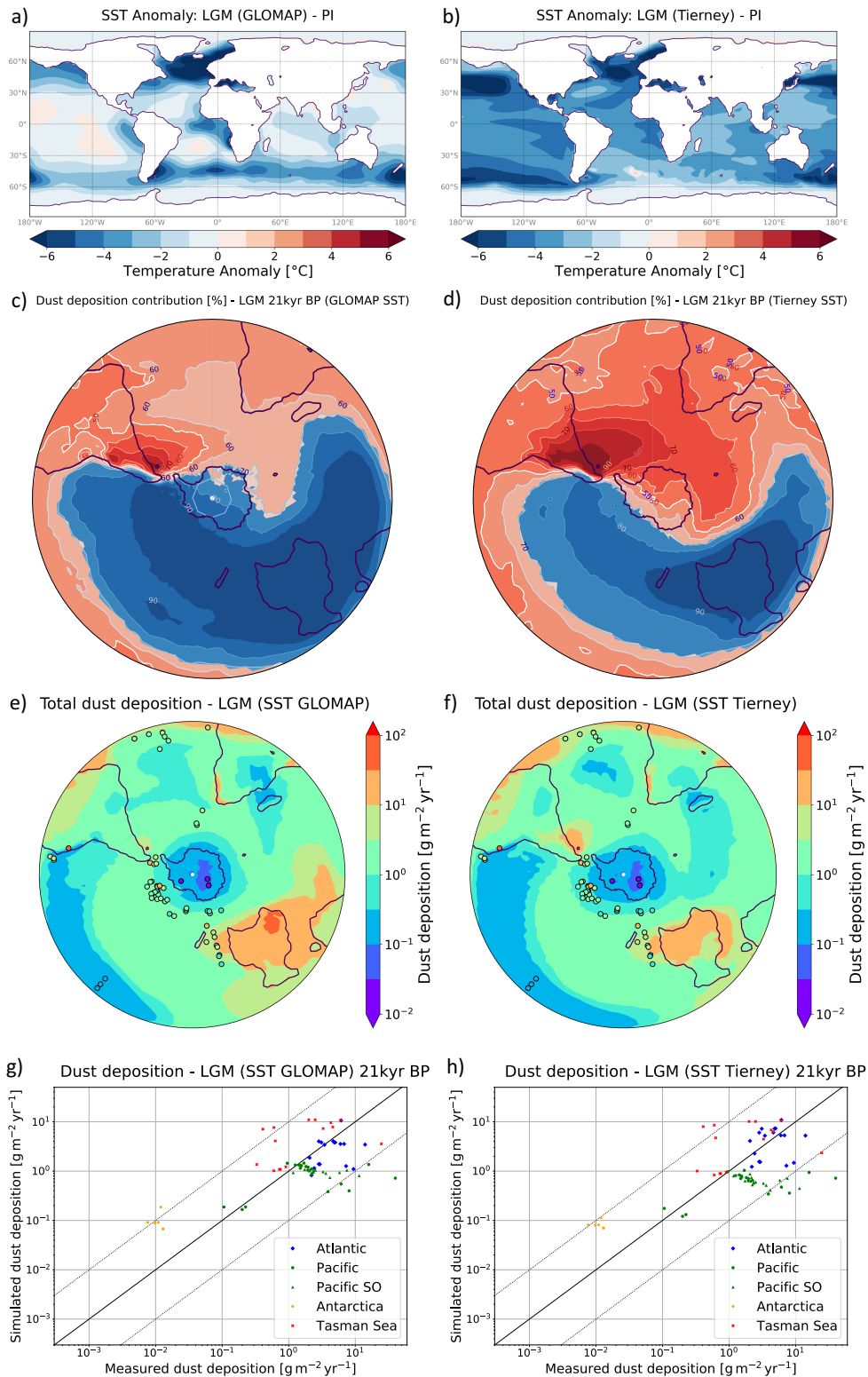


**Figure 6.1.** Overview on the SST anomalies (LGM - PI) for GLOMAP (a) and Tierney et al. SSTs (b) in  $^{\circ}\text{C}$ , the contribution of Patagonian dust (red) and Australian dust (blue) to the total dust deposition in the SH for GLOMAP (c) and Tierney et al. SSTs (d) in percent, the total dust deposition in  $\text{g m}^{-2} \text{yr}^{-1}$  in the SH for GLOMAP (e) and Tierney et al. SSTs (f), and the comparison of the simulated dust deposition fluxes to measured data provided by Kohfeld et al. (2013) at several locations for GLOMAP (g) and Tierney et al. SSTs (h).

substantially higher wind speeds over Australia ( $+0.86 \text{ m s}^{-1}$ ) compared to Tierney SSTs ( $+0.18 \text{ m s}^{-1}$ ), and vice versa over Patagonia ( $+0.11 \text{ m s}^{-1}$  and  $+0.66 \text{ m s}^{-1}$ , see Tab. 6.2)

The warm pools in the subtropical gyres in the Pacific and Atlantic Ocean indicated by GLOMAP SSTs have been discussed in detail in Chapter 5, and it should be kept in mind that the authors state that the globally-averaged cooling might be underestimated by  $0.5^\circ\text{C}$  to  $1.0^\circ\text{C}$  due to the chosen reconstruction method (Paul et al., 2021). The strong increase of dust emissions in Australia from  $47 \text{ Tg yr}^{-1}$  during PI to  $772 \text{ Tg yr}^{-1}$  during the LGM with GLOMAP SSTs explains the strong contribution to the total dust deposition in large parts of the SH, particularly over Antarctica, where regionally between 70 % and 90 % of dust are of Australian origin (Fig. 6.1c). The amount of dust from southern South America, on the other hand, only increased from  $2.3 \text{ Tg yr}^{-1}$  during PI to  $36 \text{ Tg yr}^{-1}$  during the LGM. However, using Tierney et al. SSTs leads to a substantially different source contribution in the SH. Although both SST datasets result in a source strength increase for both regions, the model simulates annual emissions of  $112 \text{ Tg}$  from Patagonia, which is more than three times as much as for GLOMAP SSTs, and  $394 \text{ Tg yr}^{-1}$  from Australia, only around half as much as for GLOMAP SSTs. This results naturally in a much stronger source contribution of Patagonian dust to the total deposition in the SH, particularly over Antarctica, where regionally between 50 % and 70 % of the deposited dust is of southern South American origin (Fig. 6.1d). This simulation result is in better agreement with the isotopic signature of dust retrieved from Antarctic ice cores, which suggest that up to 85 % is of Patagonian origin with minor contributions from Australia or South Africa (Basile et al., 1997; Delmonte et al., 2008). Although this finding is widely accepted, some uncertainty about the contribution of Australian dust sources still remains. De Deckker et al. (2010), for instance, found that the isotope signature also matches the one of soil samples from southeastern Australia, which indicates that Australia also might have been a relevant source of dust deposited over Antarctica during the LGM. However, model results suggest that the transport efficiency from Australia to Antarctica was generally much less efficient than from Patagonia (Lunt and Valdes, 2001).

Since dust is transported by the westerlies on synoptic scales, the strong variation in the Australian dust source strength between GLOMAP and Tierney et al. SSTs also affects the accordance with measured data provided by Kohfeld et al. (2013). Both SST datasets result in an underestimation of dust deposition in the Pacific and Pacific SO (Figs. 6.1g and h). Since dust depositing in that region is

## 6. Southern-Hemispheric Atmospheric Dynamics During the LGM

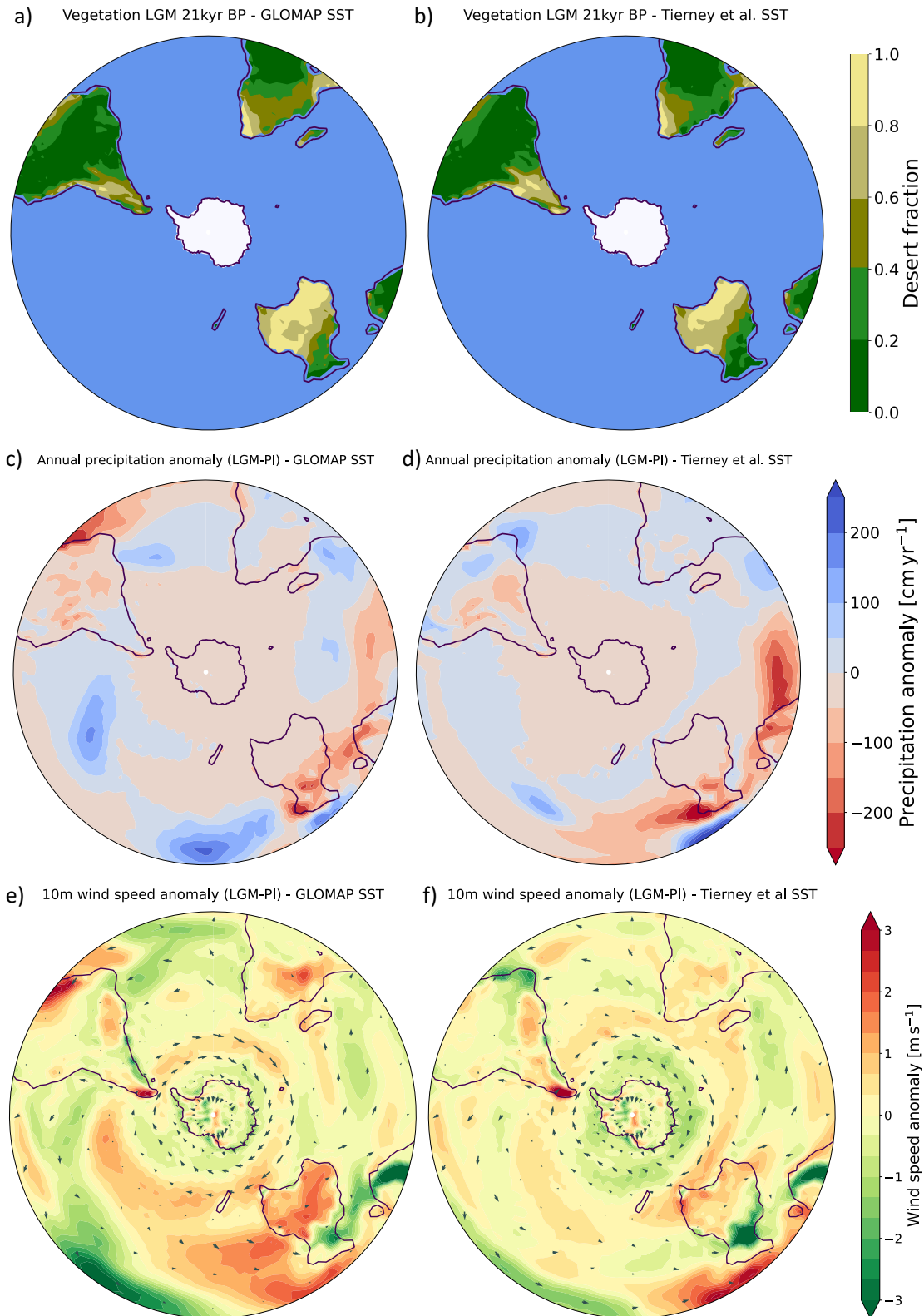


**Figure 6.2.** The figure shows the desert fraction in the SH for GLOMAP (a) and Tierney et al. SSTs (b), the annual precipitation anomaly (LGM-PI) in the SH in  $\text{cm yr}^{-1}$  for GLOMAP (c) and Tierney et al. SSTs (d), and the 10 m wind speed anomaly in the SH with the absolute wind field plotted on top for GLOMAP (e) and Tierney et al. SSTs (f). Note that water and the ice in Antarctica are shown in blue, respectively, white color in a) and b) for improved readability.

| Emission<br>[Tg yr <sup>-1</sup> ] | PI 1850-1879<br>AMIP II SST | LGM 21kyr BP<br>GLOMAP SST | LGM 21kyr BP<br>Tierney et al. SST |
|------------------------------------|-----------------------------|----------------------------|------------------------------------|
| Globally                           | 923                         | 4538                       | 5197                               |
| North. Hemisphere                  | 835                         | 3660                       | 4620                               |
| South. Hemisphere                  | 88                          | 878                        | 577                                |
| Australia                          | 47                          | 772                        | 394                                |
| South Africa                       | 12                          | 38                         | 32                                 |
| Patagonia                          | 2.3                         | 36                         | 112                                |

**Table 6.1.** Comparison between global and regional dust emissions in Tg yr<sup>-1</sup> for pre-industrial and LGM climate conditions for GLOMAP (Paul et al., 2021) and Tierney et al. (2020) SSTs.

mainly of Australian origin (> 80 %, Figs. 6.1c and d), the more pronounced discrepancy for Tierney et al. SSTs can be traced back to the substantially weaker Australian source strength. While the general trend might be caused by shortcomings in the model in terms of representing small-scale processes properly, it also needs to be considered that the measured data might actually overestimate the aeolian dust proportion in the marine sediment cores. As pointed out by McGee et al. (2015), fine sediments have only a reduced amount of phases like quartz or feldspar with low-<sup>232</sup>Th content. Since the measured dust fluxes were reconstructed based on the assumption of a constant <sup>232</sup>Th content (Kohfeld et al., 2013), the dust fluxes from the Pacific and Pacific SO, a region that receives dust mainly from Australia (Fig. 6.1c, d; Lamy et al. (2014)), might be overestimated by 30 to 40 %. However, the model also systematically overestimates dust deposition over Antarctica by a factor of 10 regardless of the used SST dataset, which might be caused by a too high meridional transport efficiency from the source regions to Antarctica. Recent data studies even suggest that fine-grained dust from central South America might have contributed up to 80 % to the dust deposition in the South Pacific Subantarctic Zone due to very efficient circum-Antarctic transport during the LGM (Struve et al., 2020). This finding is not supported by the simulation results for both GLOMAP and Tierney et al. SSTs, allowing at maximum a contribution of 10 % and 20 %, respectively.

The strong variations in the mineral dust cycle indicated by the simulation results, which are solely caused by the usage of two different SST reconstructions, suggest the analysis of the climatic conditions in the SH, particularly in the source

regions. The lower temperatures during the LGM resulted in a weaker hydrologic cycle and a drier climate in general (Lunt and Valdes, 2002), leading globally to a reduction in precipitation of  $-2.93 \text{ cm yr}^{-1}$  (GLOMAP SST) and  $-10.64 \text{ cm yr}^{-1}$  (Tierney et al. SST), respectively, compared to PI. In comparison to Tierney et al. SSTs, the simulations using GLOMAP SSTs suggest more vegetation in southern South America and less vegetation in Australia (Figs. 6.2a, b). This can be traced back to changes in the regional precipitation patterns. The warm gyres in the Pacific Ocean indicated by GLOMAP SST (6.1a) lead to increased evaporation and precipitation in these regions (Fig. 6.2c). The increased moisture is transported by the westerlies to south. South America, resulting in increased precipitation by  $7.52 \text{ cm yr}^{-1}$  (box  $[30-60]^{\circ}\text{S} \times [55-75]^{\circ}\text{W}$ ) compared to PI (Tab. 6.2). The finding of increased precipitation in southern South America is also supported by data studies (e.g. Kohfeld et al. (2013)). With Tierney et al. SSTs, precipitation in south. South America was reduced by  $-4.98 \text{ cm yr}^{-1}$  during the LGM compared to PI. Australia, on the contrary, is for both SST reconstructions suggested to be much drier during the LGM, resulting in a reduction of  $-31.75 \text{ cm yr}^{-1}$  (box  $[12-35]^{\circ}\text{S} \times [112-153]^{\circ}\text{E}$ ) for GLOMAP SST and  $-18.32 \text{ cm yr}^{-1}$  for Tierney et al. SST. The 10 m wind speed anomaly (LGM-PI) is on average higher in the south. South Pacific for GLOMAP SST compared to Tierney et al. SST (Figs. 6.2e, f), which can be traced back to the stronger temperature, and thus pressure, gradient between low and high latitudes in the SH (Fig. 5.1a, b). Regionally, Tierney et al. SST result in a stronger 10 m wind speed anomaly in Patagonia ( $0.11 \text{ m s}^{-1}$ ) compared to GLOMAP SST ( $0.66 \text{ m s}^{-1}$ ). In Australia, however, Tierney et al. SSTs lead to a rather weak increase by  $0.18 \text{ m s}^{-1}$  compared to GLOMAP SSTs, which result in a wind speed anomaly of  $0.86 \text{ m s}^{-1}$  (Tab. 6.2). The substantially stronger wind speed increase over Australia for GLOMAP SSTs can be attributed to the stronger temperature gradient between high and low latitudes compared to Tierney et al. SSTs (Fig. 5.1a, b), and also the reduced vegetation cover might have played a role. The findings of a drier climate and generally increased wind speeds in Australia during the LGM, as suggested by both GLOMAP and Tierney et al. SSTs, is in agreement with several studies indicating reduced precipitation and extended dust source regions (Williams et al., 2009) as well as increased dust emissions (McGowan et al., 2008).

In Chapter 4 it has been shown that particularly in south. South America, the additional land areas due to the reduced sea level contribute substantially to the strongly increased dust emissions during the LGM compared to PI (Tab. 4.4). However, since the identical land-sea mask has been used in the experimental setup,

|   | SST Dataset    | Globally | Australia | South Africa | Patagonia |
|---|----------------|----------|-----------|--------------|-----------|
| Precipitation anomaly<br>[cm yr <sup>-1</sup> ] | GLOMAP         | -2.93    | -31.75    | -11.66       | 7.52      |
|   | Tierney et al. | -10.64   | -18.32    | 5.55         | -4.98     |
| Wind speed anomaly<br>[m s <sup>-1</sup> ]      | GLOMAP         | 0.25     | 0.86      | 0.27         | 0.11      |
|   | Tierney et al. | 0.29     | 0.18      | 0.24         | 0.66      |

**Table 6.2.** Comparison between global and regional precipitation anomalies (LGM-PI) in cm yr<sup>-1</sup> and wind speed anomalies in m s<sup>-1</sup>, respectively, for GLOMAP (Paul et al., 2021) and Tierney et al. (2020) SSTs.

it becomes clear that the vegetation and the climatic conditions in the source regions, in terms of precipitation and 10 m wind speed, have a strong impact on the mineral dust emissions. While the findings in Chapter 4 and the considerations in appendix B indicated that a substantial source strength increase is necessary, rather than increases in particle lifetime, in order to explain the  $\sim 25$ -fold dust flux increase during the LGM found in the EDC ice core (Lambert et al., 2008), this study shows additionally the strong influence of the prescribed SSTs on those regional climatic conditions. The importance of source strength increases, particularly in south. South America, during the LGM in order to explain the strongly increased dust fluxes to Antarctica have already been suggested by other studies (Fischer et al., 2007; Wolff et al., 2010). Although individual effects such as the increased precipitation in southern South America, which is supported by data, suggest GLOMAP SSTs to result in a better representation of the mineral dust budget during the LGM, the individual source contribution of Australia and Patagonia, in terms of both total emissions and contribution to the deposition over Antarctica, as simulated by using Tierney et al. SSTs is in much better agreement with observational data (Fig. 6.1d; Basile et al. (1997); Delmonte et al. (2008)).

### 6.3.2. THE ATMOSPHERIC CIRCULATION DURING THE LGM

#### 6.3.2.1 DUST TRANSPORT IN THE SOUTHERN HEMISPHERE

While mineral dust is transported zonally by the westerlies on a synoptic scale, meridional transport is mainly caused by eddies (Li et al., 2008). One mechanism considered to explain the deposition of coarser dust particles at the Vostok region in Antarctica during the LGM are shorter trajectories (Delmonte et al., 2004). In order

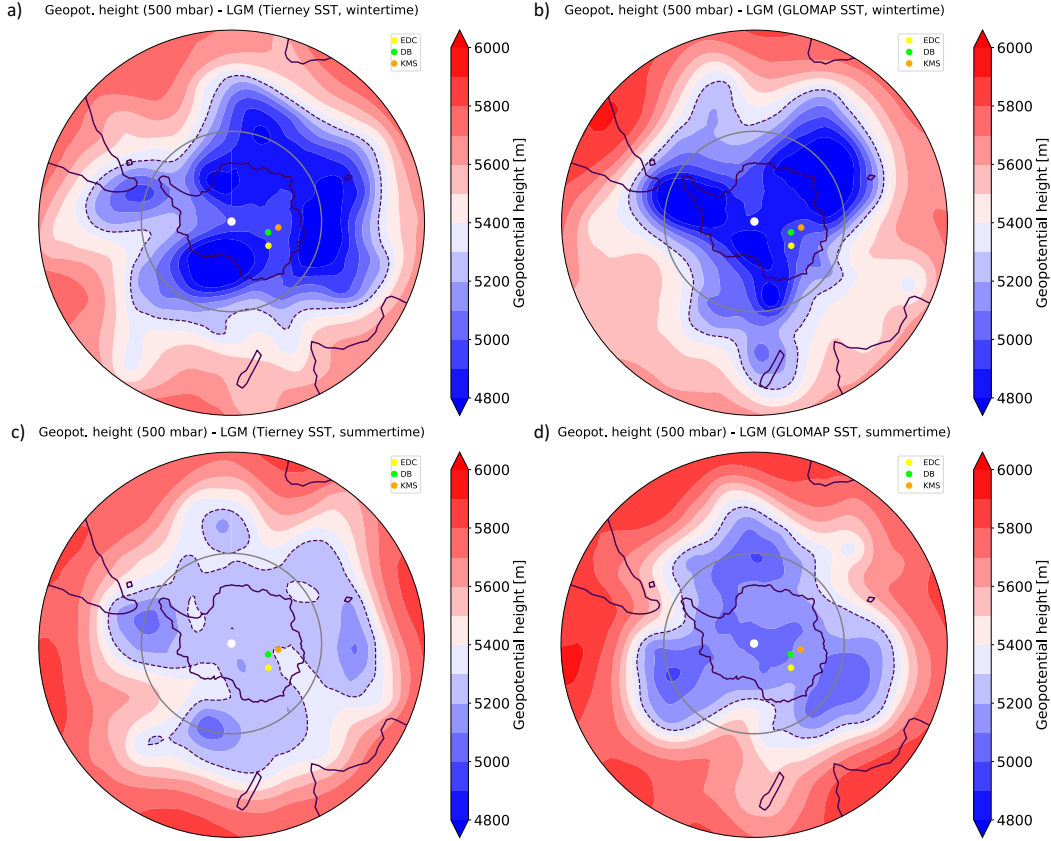


**Figure 6.3.** Contour lines of the geopotential height in m at the 500 mbar level for a randomly chosen day during south.-hem. wintertime (**a, b**) and summertime (**c, d**) for Tierney et al. and GLOMAP SSTs. The dashed lines represents the isohypse at 5300 m. In order to calculate the Meandering Index, the length of the (longest) isohypse is divided by the length of a reference circle at 60° latitude (marked in light gray). Additionally, the three ice core drilling locations EDC, DB and KMS are shown.

to test whether there is increased meridional transport efficiency of dust from the source regions to Antarctica during the LGM, a *Meandering Index* (MI) indicating the *waviness* of the circulation is defined by (Capua and Coumou, 2016)

$$MI = \frac{\text{Arclength}(i)}{2\pi R \cos(\Theta_{\text{ref}})}, \quad (14)$$

with the Earth's radius  $R$ . The index puts the length of a *isohypse*, i.e. the line connecting two points of equal geopotential height, in relation to the Earth's circumference at  $\Theta_{\text{ref}} = 60^\circ$  of latitude. In case there are several isohypses for a given geopotential height, the longest one is chosen. Figure 6.3 shows four isohypses at 500 mbar and 5300 m for a randomly chosen day during south.-hem. winter (a, b) and summer (c, d) for both GLOMAP and Tierney et al. SSTs. Table 6.3 shows the mean of the MI for three levels, namely at 300 hPa and 9000 m, at 500 hPa and

## 6. Southern-Hemispheric Atmospheric Dynamics During the LGM

|                                     | Experiment                 |             |                           |             |                                   |             |
|-------------------------------------|----------------------------|-------------|---------------------------|-------------|-----------------------------------|-------------|
|                                     | PI 1850-1879 - AMIP II SST |             | LGM 21kyr BP - GLOMAP SST |             | LGM 21kyr BP - Tierney et al. SST |             |
| Meandering Index Mean (South. Hem.) | PAT only                   | AUS only    | PAT only                  | AUS only    | PAT only                          | AUS only    |
| 300 hPa (9000 gpm)                  | 1.62 ± 0.17                | 1.62 ± 0.16 | 1.63 ± 0.14               | 1.63 ± 0.14 | 1.72 ± 0.14                       | 1.73 ± 0.14 |
| 500 hPa (5500 gpm)                  | 1.65 ± 0.17                | 1.65 ± 0.17 | 1.64 ± 0.14               | 1.64 ± 0.14 | 1.72 ± 0.15                       | 1.72 ± 0.15 |
| 700 hPa (3000 gpm)                  | 1.74 ± 0.17                | 1.74 ± 0.17 | 1.68 ± 0.15               | 1.68 ± 0.15 | 1.74 ± 0.16                       | 1.75 ± 0.17 |

**Table 6.3.** Annually-averaged MI, a measure for the waviness of the circulation, at three pressure levels for PI and LGM for GLOMAP (Paul et al., 2021) and Tierney et al. (2020) SSTs. The indices for the PAT only and AUS only experiments, respectively, are considered equal in the scope of the roundoff error and indicate that the experimental setup does not influence the atmospheric circulation.

5500 m and at 700 hPa and 3000 m for PI and LGM (GLOMAP and Tierney et al. SST). The index is given for both provenance studies (PAT only, AUS only) in order to demonstrate that the experimental setup does not influence the result and the MI can be considered equal in the scope of the roundoff error. The MI indicates for PI that the circulation decreased in waviness in the vertical from 1.74 at 700 hPa to 1.62 at 300 hPa. The result is similar for LGM (GLOMAP SST), however, the vertical decrease is less pronounced. For Tierney et al. SST, the MI remains vertically almost constant and only varies between 1.74 at 700 hPa and 1.72 at 300 hPa.

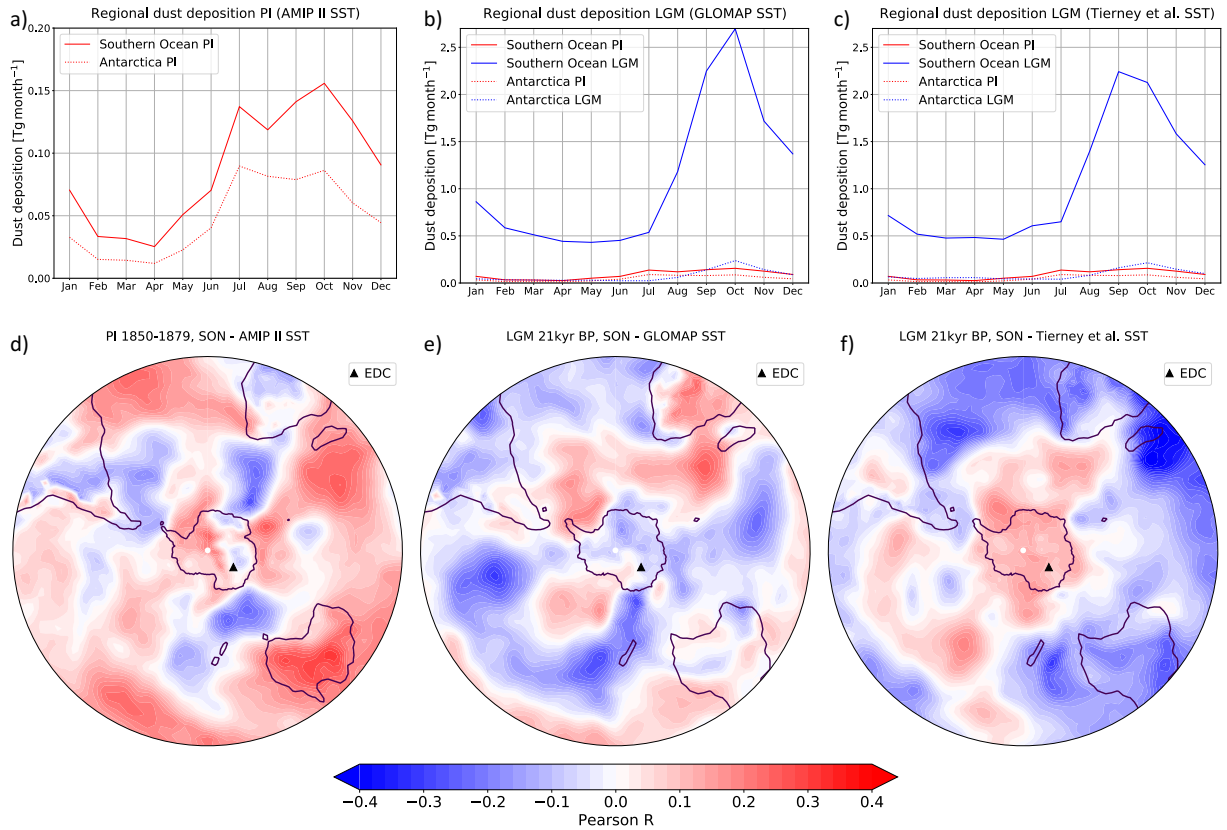
The first approach was a cross-correlation between the daily-resolved MI and the residual of the dust deposition at the EPICA Dome C location, i.e. the signal without any trend or seasonal variation. The time lag for the highest correlation could then have been interpreted as a typical transport time. However, the approach did not turn out successfully because the highest correlations, which were still low in absolute terms (around 0.05) occurred for unrealistically long time lags (>1000 d). This might be caused by the fact that there is no direct transport between the source and the deposition regions and many other factors, e.g. dust emission, precipitation during transport and at the EDC region and local circulation patterns, would need to be considered. The discussion on the meaning of the MI is resumed in section 6.3.2.2.

Figure 6.4 shows the monthly-resolved (averaged over 30 years) regional dust deposition over the SO and Antarctica for PI (a), LGM with GLOMAP SSTs (b) and Tierney et al. SSTs (c). It suggests that most dust is delivered in south.-hem. spring (SON). Figures 6.4d, e and f show the according spatial correlation between the sea level pressure in the SH and the dust deposition at EDC. Red regions indicate a positive correlation, i.e. high (low) sea level pressure coincides with high (low) dust deposition at EDC, and blue regions show a negative correlation, i.e. high (low) sea level pressure coincides with low (high) dust deposition at EDC. Since the typical transport time from the source regions to Antarctica is several weeks up to a month (e.g. Lunt and Valdes (2001)), the correlation is performed without any time lag. Figure 6.4d suggests that high dust deposition at EDC during PI coincides with a high-pressure regions over Australia and low-pressure regions over many parts of south. South America. For LGM with GLOMAP SSTs, a high-pressure region can be observed over south. South America and both regions of high and low pressure over Australia (Fig. 6.4e). With Tierney et al. SSTs, low-pressure areas can be seen over Australia and Patagonia (Fig. 6.4f).

The correlation patterns shown in Figs. 6.4d, e and f correspond to monthly-averaged regions of high (counter-clockwise rotation) and low sea level pressure (clockwise rotation). Consequently, the contour lines represent monthly-averaged transport pathways of air parcels since the flow is geostrophic on synoptic scales. Figure 4.4a shows that south. South America is the predominant source in terms of dust depositing over Antarctica during PI, although the dust source strength of Australia is substantially higher (Tab. 4.3). This is likely caused by the low-pressure region over large parts of south. South America, which allow for an efficient vertical transport of dust from the source regions. Additionally, the spatial pressure pattern over the South Atlantic and Atlantic SO enables a pathway into Antarctica directly to EDC. The high-pressure regions over Australia, however, does not allow for an efficient vertical transport of dust after emission. Furthermore, the pressure pattern over the Tasman Sea and the South Pacific / Pacific SO does not allow for an efficient transport of dust into Antarctica.

For GLOMAP SSTs, Fig. 6.1c indicates that between 70 and 80 % of all dust deposited over Antarctica is of Australian origin. This might be caused by the combined effects of very high dust emissions (Tab. 6.1) and regions of low-pressure over Australia (Fig. 6.4e). Additionally, the pressure pattern in the South Pacific enables a direct transport of dust into Antarctica to EDC. The region of low pressure over the Eastern Pacific coincides well with the pool of warm SSTs by GLOMAP

## 6. Southern-Hemispheric Atmospheric Dynamics During the LGM



**Figure 6.4.** Regional dust deposition over the SO (solid line) and Antarctica (dashed line) during PI (a), LGM for GLOMAP SSTs (b) and LGM for Tierney et al. SSTs (c). For improved comparability, the dust deposition during PI (a) is also shown in the subplots b and c. Since most dust is delivered to the aforementioned regions during south.-hem. spring (SON), the monthly-resolved spatial correlation between sea level pressure and dust deposition at EDC (black triangle) is shown for PI (d), LGM for GLOMAP SSTs (e) and LGM for Tierney et al. SSTs (f).

(Fig. 6.1a), suggesting that the SSTs have a strong influence on shape and position of the obtained high- and low-pressure regions. Southern South America, on the other hand, represents a much weaker source during the LGM with GLOMAP SSTs, and the simulation results also suggest a region of high pressure during SON. Additionally, the pressure patterns in the South Atlantic / Atlantic SO region do not allow for an efficient transport of dust from South America to Antarctica.

For Tierney et al. SSTs (Fig. 6.4f), a low-pressure area can be observed over both regions, south. South America and Australia. The climatic conditions in the source regions result in a high source strength of south. South America and a strongly reduced dust source strength of Australia compared to GLOMAP SSTs (Tab. 6.1). It is rather difficult to identify typical transport pathways of dust from both source regions, Australia and South America. However, the combined effects of reduced

source strength and impeded transport to Antarctica compared to GLOMAP SSTs result in a weaker contribution of Australia to dust deposited over Antarctica. The strongly increased source strength of south. South America, on the other hand, results eventually in the predominant contribution to dust deposited over Antarctica, as indicated by Fig. 6.1d).

### 6.3.2.2 STRENGTH, POSITION AND SHAPE OF THE ZONAL CIRCULATION

Finally, the zonal circulation as simulated by the model is investigated in terms of strength, shape and position for both GLOMAP and Tierney et al. SSTs and compared to PI. Figure 6.5 shows zonally-averaged isotachs together with isolines of potential temperature  $\Theta$  for PI and LGM. The annually-averaged plots (Fig. 6.5a, b, c) indicate a vertical stretching of the isotach cross sections in the Northern Hemisphere for LGM compared to PI. In the SH, the stretching occurs in horizontal direction during the LGM and is more pronounced for Tierney et al. SSTs. For improved readability, the isotachs for LGM and PI are shown within the same plots for the SH in Fig. 6.6 for GLOMAP (a, c, e) and Tierney et al. SSTs (b, d, f). The shift towards the equator along with the horizontal stretching occurs during wintertime, i.e. during DJF in the Northern Hemisphere (Fig. 6.5d, e, f) and JJA in the SH (Fig. 6.5g, h, i). For PI and both LGM experiments, a equatorward shift of the core of the zonal flow during wintertime (DJF for the North. Hemisphere, JJA for the South. Hemisphere) can be observed compared to summertime (Figs. 6.5 and 6.6). For Tierney et al. SSTs (Fig. 6.5c), the cross section of the core of the zonal flow (wind speed  $> 30 \text{ m s}^{-1}$ ) is much smaller compared to GLOMAP SSTs (Fig. 6.5b, 6.6a) and PI (Fig. 6.5a, 6.6b). The annually-averaged  $\Theta$  isotherms in Figs. 6.5a, b and c show particularly in the middle and upper troposphere between 5 km and 15 km and the low- to mid-latitudes a larger spread for both LGM experiments compared to PI.

Before Figs. 6.5 and 6.6 are discussed in detail, important theoretical background information concerning the zonal circulation is concisely recapitulated. Due to its spherical geometry, the Earth has a positive energy balance between  $30^\circ\text{N}$  and  $30^\circ\text{S}$  and a negative energy balance towards the poles. The resulting temperature and pressure gradients between low- and mid-latitudes cause a meridionally-directed flow at altitude, which is deflected to the west by the Coriolis force. This results in a zonally-directed geostrophic wind (*midlatitude westerlies*). Since the zonal flow does not allow for a meridional compensation of the energy imbalance, the temperature gradient and therefore the flow velocity increase. At

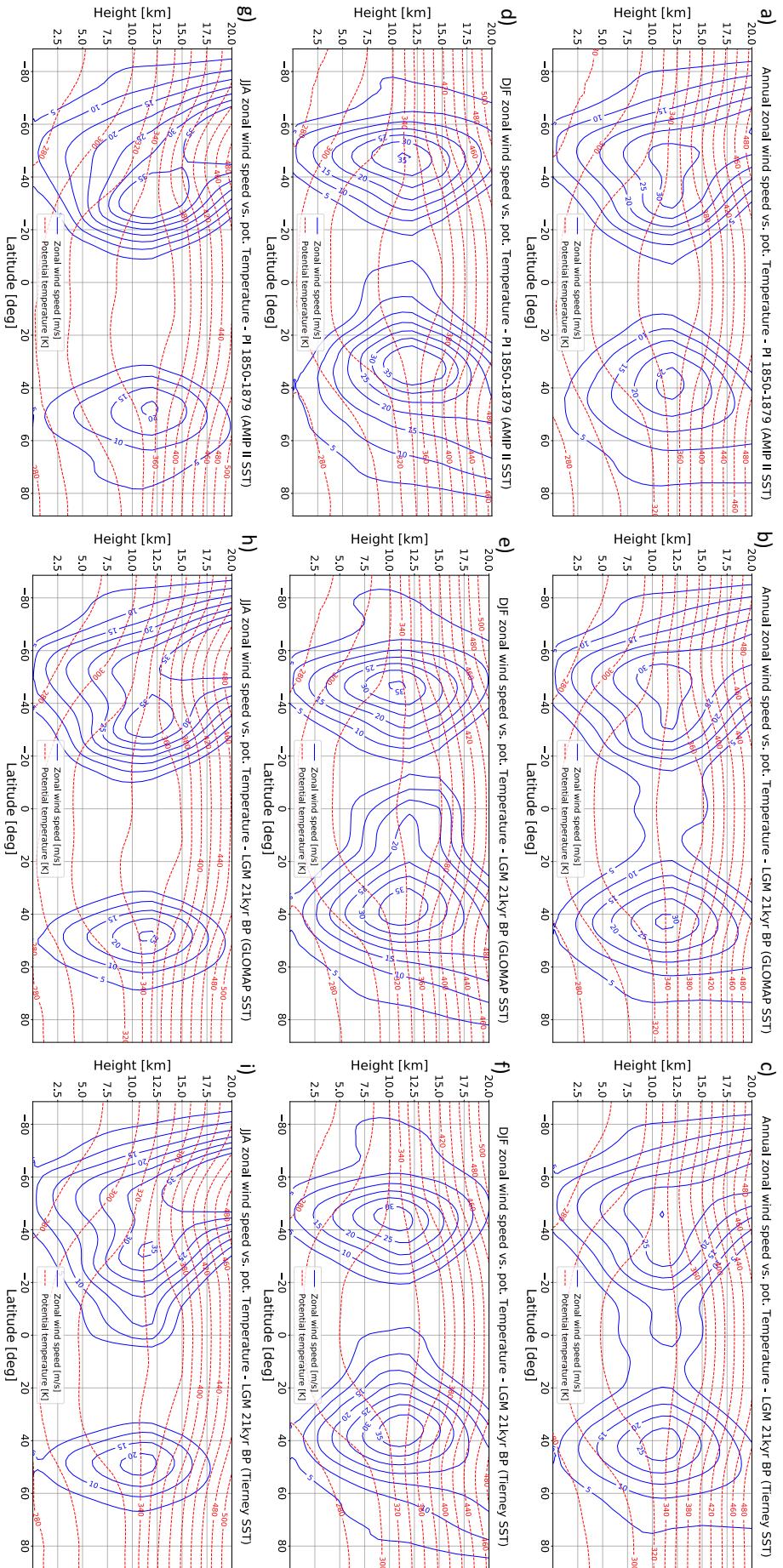


**Figure 6.5.** Zonally-averaged isotachs in  $\text{m s}^{-1}$  (blue) and isolines of potential temperature in K (red) for PI (a, d, g), LGM using GLOMAP SSTs (b, e, h) and LGM using Tierney et al. SSTs (c, f, i). The subfigures show annually-averaged (a, b, c) as well as seasonally-averaged conditions for DJF (d, e, f) and JJA (g, h, i).

## 6. Southern-Hemispheric Atmospheric Dynamics During the LGM

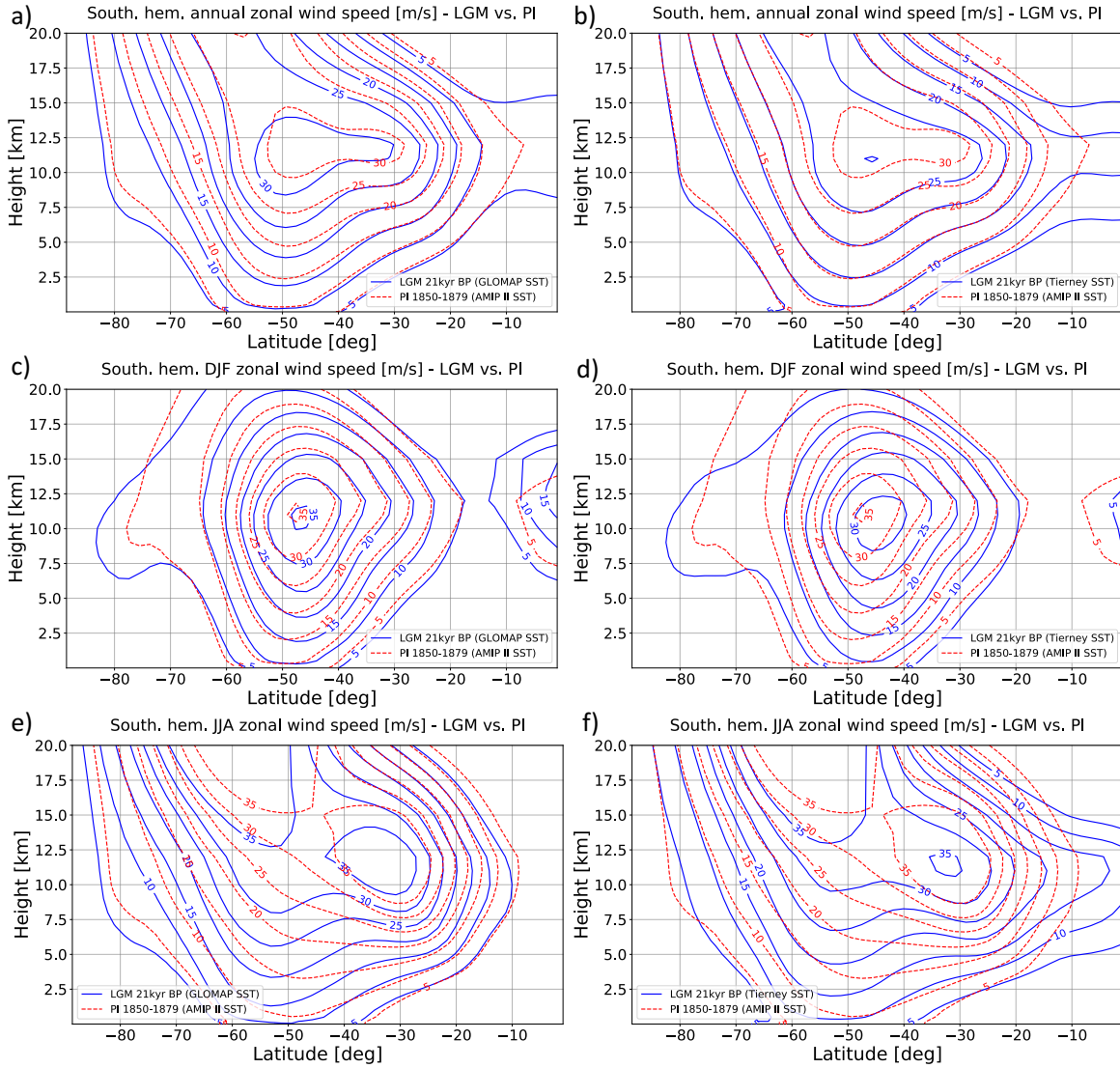


**Figure 6.6.** Zonally-averaged isotachs in  $\text{m s}^{-1}$  for LGM (blue) and PI (red) for GLOMAP SSTs (a, c, e) and Tierney et al. SSTs (b, d, f) in the SH. The subfigures show annually-averaged (a, b), as well as seasonally-averaged conditions for DJF (c, d) and JJA (e, f).

some point, a small perturbation leads to an instability of the zonal flow and it starts to meander (see Fig. 6.3 & Tab. 6.3). It then forms so-called troughs and ridges, allowing the poleward transport of warm air masses and the equatorward transport of cold air masses. This process intensifies until the flow cuts off and forms isolated cyclones and anti-cyclones, where cold and warm air masses are mixed. Over time, the temperature gradient between low and mid-latitudes builds up and the zonal flow sets in again (McMurdie and Houze, 2006; Stocker, 2011).

However, the idealized situation described above is only valid for barotropic conditions, where the conservation of absolute vorticity ensures that the upper-level

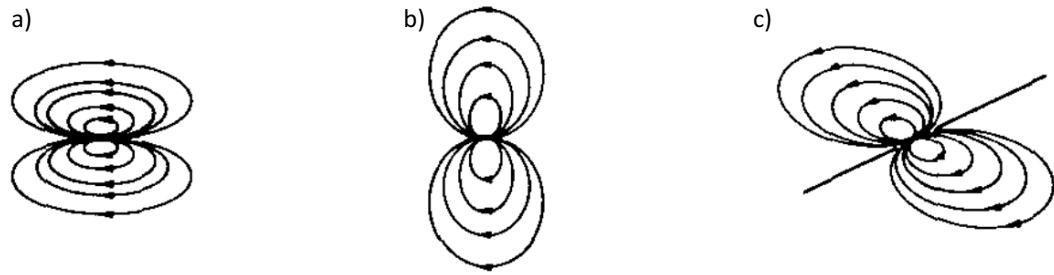


**Figure 6.7.** Vertical cross sections of the stream function for point sources (or azimuthal rings in three dimensions, respectively) of momentum, e.g. a zonal flow in geostrophic balance, as suggested by the SAWYER-ELIASSEN equation. The vortices are shown **(a)** for barotropic conditions with weak inertial stability, **(b)** barotropic conditions with strong inertial stability and **(c)** for baroclinic conditions. [Figure modified from Shapiro (1981)]

airflow meanders horizontally. Quasi-barotropy is only given in the middle of the troposphere. Instead, the horizontal displacement of air masses leads to the formation of airflow divergence and confluence at altitude, which corresponds to regions of confluence and divergence at low levels. As a consequence, a vertical airflow arises, which superimposes the horizontal basic flow. This results in a westwards directed flow with vertical and meridional deflections, and the propagation of these meanders is called baroclinic ROSSBY wave (Holton, 2004).

A mathematical framework in order to investigate the vertical cross section of this so-called *secondary circulation* in meridional direction by a streamfunction approach has been provided in form of the SAWYER-ELIASSEN (SE) equation (Sawyer, 1956; Eliassen, 1962). The analysis of the SE equation shows that the shape of the isotachs in a vertical cross section for a azimuthal flow in geostrophic and hydrostatic balance, which represents a source of momentum, is essentially determined by three terms (Wang and Smith, 2019):

- the *static stability*, which depends on the vertical temperature gradient, i.e. the lapse rate. A weak lapse rate corresponds to weak restoring forces, i.e. lower static stability, in vertical direction, and leads to a larger vertical extend of the cross sections of the isotachs.
- the *inertial stability*, which depends on the horizontal momentum gradient. A smaller gradient implies weaker restoring forces, i.e. lower inertial stability, in meridional direction, which result in a horizontal stretching and a vertical compression of the streamfunction (6.7a), and vice versa for higher inertial stability (6.7b).

- the *baroclinicity*, which depends on the vertical momentum gradient. Baroclinicity leads to a rather diagonal shape of the vortex compared to barotropic conditions (6.7c).

The previous considerations allow for some insights on the simulations results shown in Figs. 6.5 and 6.6. The vertical stretching of the cross section of the annually-averaged isotachs in the Northern Hemisphere (6.5b, c) suggest a weaker static stability due to a reduced lapse rate compared to PI (6.5a), which would be in agreement with the strong surface cooling for both GLOMAP and Tierney et al. SSTs due to the ice sheets over North America and Europe. Additionally, this finding would also be in accordance with the increased spreading of the  $\Theta$  isolines in the middle and upper troposphere in the low- and mid-latitudes. Although an increase in inertial stability would lead to a similar effect (see Fig. 6.7b), this explanation seems unlikely for Tierney et al. SSTs because the speed of the core of the zonal flow is as high as for PI. However, for GLOMAP SSTs, the higher wind speed in the core of the zonal flow ( $30 \text{ m s}^{-1}$ , Fig. 6.5b) compared to PI ( $25 \text{ m s}^{-1}$ , Fig. 6.5a), which is caused by the larger temperature gradient between low and high latitudes, might have led to a stronger meridional momentum gradient, which in turn would have caused higher inertial stability and therefore would have contributed to the vertical elongation. Generally, the zonal circulation appears to be uniformly shifted towards lower altitudes during the LGM, a effect which can be seen best in Figs. 6.5g, h and i for the Northern Hemisphere and Fig. 6.6 for the SH. This might be caused by the reduced convection due to the lower temperatures and the vertically less extensive troposphere, as discussed in Chapter 4 for the dust transport in lower levels during the LGM (see Fig. 4.6).

In the SH, a vertical stretching cannot be observed. Instead, the zonally-averaged cross sections of the isotachs show a horizontal stretching for both GLOMAP and Tierney SSTs (Fig. 6.6a, b), which indicates lower inertial stability. In south.-hem. summer (DJF), the zonal circulation appears uniformly shifted equatorwards by 2 to 3° latitude during the LGM for both GLOMAP and Tierney et al. SSTs compared to PI, rather than stretched horizontally (Fig. 6.6c, d). The effect is more pronounced for Tierney et al. SSTs and might be caused by lower temperatures in low latitudes during summer. During south.-hem. winter (JJA), the effect of the vortex shearing (see Fig. 6.7c) can be well observed for both GLOMAP and Tierney et al. SSTs (Fig. 6.6e, f). In winter, the temperature gradients between low and high latitudes are the greatest, and the front in between has the highest baroclinicity. Considering the stronger shear of the vortices for GLOMAP and Tierney SSTs com-

pared to PI (Figs. 6.6e, f), the baroclinicity in the SH during the LGM was much higher in winter compared to PI. This can be explained by the much stronger cooling in the high latitudes during the LGM, as indicated by the  $\Theta = 280$  K isotherm (Figs. 6.5g, h, i). The circulation for Tierney et al. SSTs indicates a weak inertial stability during JJA in the middle and high troposphere between 5 km and 15 km (Fig. 6.6f), a feature which can also be seen in the annually averaged pattern (Fig. 6.6b). This finding is in agreement with Table 6.3, which suggest strong meridional deflections, i.e. a higher MI, of the zonal circulation at the 300 hPa level compared to GLOMAP SSTs and PI. Particularly the shift in the lower troposphere is in agreement with the higher 10 m wind speed over south. South America (Fig. 6.2f, Tab. 6.2) compared to LGM with GLOMAP SSTs (Fig. 6.2e, f; Tab. 6.2).

Kohfeld et al. (2013) provide a synthesis on paleo-data of terrestrial moisture, dust deposition, SSTs, ocean productivity and other proxies for the LGM. Due to the interactions of the climate elements, the interpretation of these data in terms of position and strength of the westerlies in the SH during the LGM is ambiguous and allows for several scenarios. However, based on terrestrial moisture data from the west coast of south. South America and South Africa, which suggest increased precipitation, the authors conclude that a equatorward shift of the westerlies would be in best agreement with the observational data. Simulations by Sime et al. (2013), however, show that the increased precipitation in these regions were also reproduced by a model which indicates even a poleward shift of the westerlies. The simulation results presented in this study do not clearly indicate a annually-averaged, uniform shift over the whole vertical extent in either direction, neither for GLOMAP nor for Tierney et al. SSTs. Instead, they suggest weaker inertial stability and thus a meridional stretching of the cross section of the zonally-averaged circulation, a effect that is generally more pronounced for Tierney et al. SSTs. Consequently, the wind speeds in the lower troposphere closer to the equator are higher. This can also be seen in Figs. 6.2e and f, particularly the stronger equatorward displacement of the 10 m wind speed for Tierney et al. compared to GLOMAP SSTs. However, during south.-hem. summer (DJF), the zonally-averaged circulation pattern in the SH appears to be shifted equatorwards, around 2 to 3° for GLOMAP SSTs and 4 to 5° for Tierney et al. SSTs compared to PI (Figs. 6.6c, d). During winter (JJA), this is counteracted by a poleward shift of the zonally-averaged circulation in the lower troposphere compared to PI due to increased barotropicity and low inertial stability in the middle and upper troposphere, particularly for Tierney et al. SSTs (Figs. 6.6e, f).

In summary, the results suggest that the weaker meridional temperature gradient between the high and low latitudes for Tierney et al. SSTs (due to the stronger cooling in the tropics, see Fig. 6.1a, b) compared to GLOMAP SSTs result in a zonal flow with less total momentum, particularly in the middle and upper troposphere. This leads in turn to a weaker meridional momentum gradient, i.e. lower inertial stability, and the vertical cross sections of the zonally-averaged isotachs are stretched horizontally. The equatorward shift of increased terrestrial moisture during the LGM indicated by data (Markgraf et al., 1992; Kohfeld et al., 2013) would also be in agreement with an equatorward stretching of the zonal circulation in the middle and upper troposphere, because atmospheric water vapor is transported at these levels.

#### 6.4. SUMMARY AND CONCLUSIONS

Prescribing GLOMAP and Tierney et al. SSTs results in substantially different mineral dust cycles for LGM climate. The differences can be traced back to changes in vegetation cover and meteorological factors like wind speed and precipitation in the source regions. Moreover, the spatial correlation analysis between dust deposition at EDC and sea level pressure patterns in the SH during SON, i.e. the season of highest dust delivery to Antarctica, suggest that the efficiency of transport pathways from the source regions to Antarctica strongly varies with the prescribed SSTs. This affects additionally the contribution of the individual sources to dust deposited over Antarctica. GLOMAP SSTs lead to a higher agreement with observational data in terms of total dust deposition in the South Pacific / Pacific SO. Tierney et al. SSTs, on the other hand, result in a predominant Patagonian source contribution to the total dust deposited over Antarctica during the LGM, which is in much better agreement with measured data on dust provenance.

The verification of simulation results in terms of three-dimensional atmospheric circulation patterns during the LGM, which are produced by a model with data-based SST and SIC boundary conditions, is generally very challenging. It relies on the comparison to paleo-data, e.g. for terrestrial moisture, dust deposition as well as ocean productivity and circulation. Although all aforementioned proxies are influenced by the atmospheric circulation, also other factors play a role and offer several possible explanations (Kohfeld et al., 2013). Since SIC were identical in both LGM experiments, this study clearly demonstrates that changes solely in the SSTs lead to substantial differences in the obtained results. Therefore, the most expedient and desirable approach would be on the data side in terms of reduc-

ing the uncertainties in the SST reconstruction for the LGM (see also Wolff et al. (2010)).

The analysis provided in this study also focuses on the zonally-averaged response of the zonal circulation in the SH to different SSTs. It shows that changes in strength, shape and position can be traced back to changes in absolute temperature, static and inertial stability as well as baroclinicity of the atmosphere. A uniform, annually-averaged shift of the westerlies is not found for either SST reconstruction. However, the horizontal stretching of the zonal circulation particularly in the lower troposphere, which is most pronounced during south.-hem. summer (DJF), would also explain measured trends in terrestrial moisture in the SH, which have been interpreted as a indicator for a equatorward shift of the westerlies. The stronger ridging of the atmospheric circulation in the SH during the LGM suggested by Markgraf et al. (1992) would also be in agreement with the found horizontal stretching of the zonally-averaged pattern due to reduced inertial stability.

The next step on the modelling side could be a detailed comparison of the simulated circulation in specific regions to observational data. Williams et al. (2009), for instance, found evidence that dust from the Lake Eyre Basin / Simpson Desert in Australia was transported around 350 km (approx. 3°) further northwards during glacial times compared to present-day dust fluxes. The authors state that this finding is consistent with a equatorward shift of the subtropical ridge and might therefore also apply to the mid-latitude westerlies. Uncertainties also still remain for Patagonian climate conditions during the LGM. The seasonality and interplay between dust production, glacier extent, precipitation patterns, type and amount of vegetation as well as the atmospheric circulation patterns is still a matter of current research (Markgraf et al., 1992; Haberzettl et al., 2009; Wolff et al., 2010; Lamy et al., 2014). However, since the glacier mask used in this study does not account for the ice sheet covering parts of the Southern Andes in Patagonia during the LGM (e.g. Hulton et al. (2002)), it would need to be adjusted. Since the glacier mask has been kept constant in this study, the lack of the Patagonian ice sheet is not problematic and allows for the investigation of climate changes solely imposed by changes in the SSTs. Additionally, due to the rather coarse resolution of T63 (1.875° x 1.875°) only a few grid points would be covered by the glacier. However, if simulations are performed with a higher spatial resolution and a focus on the regional climate in Patagonia, the consideration of the ice sheet is indispensable.

As shown in this study, the vertical temperature profile of the atmosphere influences the circulation. Future research could then also include the comparison of

the vertical temperature profile along mountains to observational data, which suggest that the snowline was uniformly lower during the LGM (Broecker and Denton, 1989). Since assumed latitudinal shifts in the westerlies are typically in the order of magnitude of a few degrees, a higher spatial resolution than used in this study might be beneficial in order to investigate changes on a regional scale.



"Further, we have to be prepared always for the possibility that each new discovery, no matter what science furnishes it, may modify the conclusions we draw."

---

(Alfred Wegener, *The Origin of Continents and Oceans*)

## 7. FINAL CONSIDERATIONS

### 7.1. CONCLUSION

In this thesis, the aerosol-climate model ECHAM6.3-HAM2.3 is used to investigate the mineral dust cycle for PD, PI and LGM climate with a focus on the SH. Of particular interest are all processes which affect mineral dust emission, transport and deposition, including climatic factors in the source regions as well as atmospheric circulation and precipitation patterns, and how they are influenced by different climate conditions as a result of varying sea surface temperatures. The research questions formulated in the beginning of this thesis guided the research documented in the chapters 4, 5 and 6, and a concise answer to each of them is given in the following:

1. **How well is the chosen model able to simulate dust fluxes in comparison to observational data for present day, pre-industrial and LGM climate, particularly in the SH?**

For present-day climate, ECHAM6.3-HAM2.3 yields results for mineral dust deposition that are globally in good agreement with observational data (see appendix A). For pre-industrial climate, the simulated dust deposition is too low in comparison to observational data and other modelling studies. Particularly dust emissions from Australia seem to be underestimated, which results in too low dust deposition fluxes in the southern South Pacific. The model performs generally well under LGM climate conditions and reproduces the observed increase in global dust deposition. However, the simulated dust deposition during the LGM is underestimated in the South Pacific and too high over Antarctica. The discrepancy might be caused by shortcomings in the model in terms of dust transport efficiency and deposition, but also the marine sediment data might not properly account for non-aeolian contributions.

The increase in dust burden and deposition in the SH during the LGM can be traced back to strongly increased emissions from the major dust source regions Australia, southern South America and South Africa, which in turn are caused by the generally drier climate (except for Patagonia), increased wind speed over the source regions and reduced vegetation. Increased particle lifetimes due to drier climate conditions during the LGM are not sufficient in order to explain the increased dust deposition over Antarctica; instead, the model suggests that a substantial increase in source strength is additionally necessary in order to explain the observations (see appendix B). Particularly in Patagonia, the additional land areas due to the lower sea level contributed substantially to the increased source strength. Reduced precipitation over the SO results in longer particle lifetimes. However, the simulated influence of precipitation on particle lifetimes has to be assessed carefully because the prescribed sea surface temperatures, which have a strong influence on the precipitation patterns, might be too warm.

**2. Can simulation results help to improve constraining proper, global sea surface temperature reconstructions for the LGM?**

Prescribing both GLOMAP and Tierney et al. SSTs in ECHAM6.3-HAM2.3 and comparing the simulated land surface temperatures to reconstructed data based on noble gas concentrations in groundwater did not provide clear indications which SST dataset results in a better agreement. GLOMAP SSTs, which suggest a weaker cooling during the LGM compared to pre-industrial climate than Tierney et al. SSTs, lead to a good agreement between observational data and simulation results along the glacier margins in North America and Europe, but the simulated land surface temperatures are systematically too warm in the tropics and subtropics, and vice versa for Tierney et al. SST. The approach of using climate models in order to verify prescribed boundary conditions is generally challenging and requires the correct representation of several important feedback mechanisms in the model, e.g. the soil-albedo feedback or the water vapor-lapse rate feedback. Another source of uncertainty in the models is the spatial resolution, which is generally confined due to limited computational resources and therefore requires the representation of many important sub-grid scale processes in form of parameterizations. Improvements could be achieved by repeating the same experiments, i.e. prescribing the same SSTs, with different AGCMs in order to reduce individual model biases by using multi-model means instead. For a thorough

comparison between simulation results and observational data, a higher data availability would be necessary.

**3. What are the effects of prescribing different sea surface temperature reconstructions on the mineral dust cycle and the atmospheric dynamics in the SH?**

The globally and regionally differences in the suggested SST cooling between GLOMAP and Tierney et al. SSTs during the LGM compared to PI has a substantial influence on the simulated mineral dust budget. On the one hand, changes in source strength in the major source regions in the SH can be traced back to changes in vegetation, wind speed close to the ground and precipitation. On the other hand, the induced changes in atmospheric circulation patterns over the source regions and along the transport pathways to the deposition regions over the SO and Antarctica play also an important role. The simulations for the LGM with Tierney et al. SSTs show a high agreement with observational data in terms of individual source contribution of south. South America and Australia to the dust deposition over Antarctica. GLOMAP SSTs result in a stronger Australian dust source during the LGM and a higher agreement with observational data in terms of absolute dust deposition in the Pacific SO, but the simulated individual source contribution is not supported by data. Additionally, it has to be kept in mind that GLOMAP SSTs might globally be too warm by up to 1 °C due to the used reconstruction method.

The atmospheric circulation during the LGM is generally characterized by weaker static stability in the Northern Hemisphere due to a reduced lapse rate and weaker inertial stability due to lower horizontal momentum gradients of the zonal flow compared to PI. Particularly during south.-hem. winter (JJA), the baroclinicity in the front between low and high latitudes in the SH appears to be stronger for both LGM experiments compared to PI. For Tierney et al. SSTs, the inertial stability in the middle and upper troposphere appears strongly reduced. During south.-hem. summer (DJF), the zonal circulation is almost uniformly shifted equatorwards for both LGM experiments by 2 to 3° with GLOMAP SSTs and 4 to 5° with Tierney et al. SSTs is found. Annually-averaged, this leads to a horizontal stretching of the vertical cross sections of the zonal flow close to the ground such that the region of high zonal wind stress is shifted equatorwards by 2 to 3° of latitude for Tierney et al. SSTs. So far, the uncertainty concerning the south.-hem. circulation during the LGM is high, and data would support several hypothesis' in terms of position

and strength of the westerlies. Reliable insights on the dynamics by models are only possible once the constraints on the boundary conditions in terms of SST and SIC are tighter from the data side.

Although the model clearly indicates a strong sensitivity of the mineral dust cycle to changes in the climatic conditions, it has to be kept in mind that all results are eventually produced by one specific model and might therefore be influenced by biases. Uncertainties are introduced by the limited complexity of the model, i.e. determined by the physical and chemical processes which are being considered (or not), and the way these considered processes are represented in the model, i.e. whether they are parameterized or calculated explicitly.

The modal approach to represent the aerosol particle size distribution by superimposed lognormal modes (Vignati et al., 2004; Stier et al., 2005), for instance, allows for more complex physical and chemical interactions of dust in the model compared to representing mineral dust just by a mass concentration (*bulk approach*, Boucher (2015)). However, this feature comes with the disadvantage of higher computational costs, which in turn limits the considered time periods. A very fine representation of the particle size distribution (*bin or sectional approach*, Boucher (2015)) would allow for a detailed investigation of size-dependent processes beyond Mie scattering based on the median radius of a lognormal mode, e.g. particle sorting during transport or microphysical processes in clouds. The inclusion of information on the (spatially varying) mineralogical composition of dust particles and their absorption of longwave radiation would additionally allow for a more reliable assessment of the question whether mineral dust has a net-cooling or warming effect (Albani et al., 2014; Kok et al., 2017).

Another shortcoming applying to most current mineral dust representations in AGCMs is the underestimation of very coarse particles (diameter  $d > 5 \mu\text{m}$ ) in terms of emission and long-range transport (Adebiyi and Kok, 2020; Kok et al., 2021), and even particles with  $d > 75 \mu\text{m}$  have been found in dust traps in the Atlantic Ocean, far away from their source regions (van der Does et al., 2018). The exact reason for this discrepancy is currently unknown, however, several ideas are being discussed. Most models assume a spherical dust particle shape and derive quantities like volume and surface, which are important for transport properties or chemical reactions, just based on the particle diameter. However, particles are usually not perfectly spherical, and the drag coefficient of irregular non-spherical particles increases with decreasing sphericity (Castang M. et al., 2022), which implies lower sinking velocities and therefore higher particle lifetimes (Yang et al., 2013). Another

factor which might play a crucial role is the electric charge of dust particles. The initial charge might be brought upon particles during the saltation process, and due to the Earth's electric field, the gravitational settling of suspended (negatively charged) particles are counteracted by electric forces, which keep the particles aloft (van der Does et al., 2018). Studies suggest that the electrostatic effects could even increase the total amount of emitted dust by a factor of 10 (Esposito et al., 2016). Although the initial charge would be lost soon after emission, dust plumes likely maintain a charged state via triboelectric charging between interacting particles (Harrison et al., 2016). These findings strongly suggest the introduction of electrically charged particles into dust models to account for their effects, either in form of parameterizations or magnetohydrodynamic models of the atmosphere.

### 7.2. OUTLOOK

The obtained dust deposition fields will be used as input for an Atmosphere/Ocean General Circulation Model coupled to a biogeochemical model (e.g. Schourup-Kristensen et al. (2014)) in the scope of the project *DustIron* in order to investigate the effects of dust-induced iron fertilization on the oceanic bioproductivity in the SO during the LGM. The upper limit of this effect has been constrained to around 40 ppm based on paleoceanographic data (Martínez-García et al., 2011). However, the analysis of a high-resolution record of dust deposition and oceanic productivity from the Antarctic Zone shows that high deposition and high productivity were indeed antiphased, suggesting that iron fertilization was unlikely responsible for a substantial share of the observed CO<sub>2</sub> reduction (Weber et al., 2022). Instead, the authors suggest that other processes like an extended sea-ice cover, reduced bottom water export and increased water column stratification might have played a more crucial role. The finding of a weak influence of iron fertilization on atmospheric CO<sub>2</sub> reduction is partially supported by recent modelling studies with more sophisticated models. For instance, Lambert et al. (2015) constrained the effect to around 20 ppm on multimillennial timescales, and Muglia et al. (2017) found an even weaker effect of around 13 ppm by assuming a 10 times higher dust iron solubility during the LGM compared to PI in the SO, even though hydrothermal and sedimentary iron fluxes were likewise considered.

Since increased dust deposition in the SO did not only occur during the LGM, but started already around 50 kyr before the LGM (Martínez-García et al., 2014), the highest effects of iron fertilization on the atmospheric CO<sub>2</sub> level might have already occurred before the LGM. To test this hypothesis, transient simulations

from the LIG to the LGM would be necessary. However, this approach is currently not feasible with a complex, coupled model setup due to computational limitations. Alternatively, individual time slices for several periods between the LIG and the LGM could be investigated. Though, such a setup would need to account for other effects as well. A drier climate towards the LGM might have resulted in slower weathering and therefore dust production. However, if a dust source is very active for a long time and the weathering rate is too slow to replenish it, the source might become depleted (Rea, 1994; Fischer et al., 2007). To account for such an effect in a transient simulation, *weathering* or at least *finite dust sources* would have to be included.

The fertilizing effects of iron addition into the oceans and the subsequent impact on the atmospheric CO<sub>2</sub> concentration are also being considered as a potential mean for geoengineering (e.g. Smetacek et al. (2012); Boyd and Bressac (2016)). Model results suggest that the effectiveness of iron fertilization depends on many factors like the ocean circulation and the biogeochemistry, and depending on the depth of the carbon sequestration, more than 66 % might be reexposed to the atmosphere on a typical timescale of 38 yr (Robinson et al., 2014). This indicates that, apart from political and societal implications of exploiting geoengineering methods in order to counteract climate change, we have to make sure to understand the process of CO<sub>2</sub> sequestration in the oceans due to iron fertilization in all details *before* we utilize such a method. If not, unforeseen consequences might be detrimental in the near or even far future.

Generally, the adequate representation of mineral dust in weather and climate models might become increasingly important due to climate change. Modelling studies suggest that we are facing a time of globally increased dust burden due to higher aridity and anthropogenic land use change (Stanelle et al., 2014). Due to the known effects of small mineral dust particles on human health (e.g. Morman and Plumlee (2013); Schweitzer et al. (2018)), the forecast of dust storms in regions with high exposure and vulnerability could become very important.

Mineral dust plays also a crucial role in other scientific fields, e.g. in Astrophysics, and modelling advances in either field might be beneficial for the other. The relationship between horizontal (saltation) and vertical (emission) dust flux implemented in HAM2.3, for instance, is based on a scheme developed by White (1979), who investigated aeolian soil transport on Mars. But also outside of planetary atmospheres, knowledge about physical and chemical properties of mineral dust is indispensable to understand certain fundamental processes, e.g. the for-

mation of rocky planets in protoplanetary disks. In contrast to the Earth's atmosphere, where the interaction between dry dust particles can be neglected in terms of agglomeration (Stier et al., 2005), the evolution of planets requires grain growth. This process goes through phases of coagulation / agglomeration and accretion (e.g. Dullemond and Dominik (2005)), and models also need to account for counteracting processes such as fragmentation (Birnstiel et al., 2010, 2012). Moreover, the gas density in protoplanetary disks, which is much lower than in the Earth's atmosphere, results in a strong influence of dust on the thermodynamic properties and hydrodynamic stability of the disk, which in turn affects planet formation (Lin and Youdin, 2017).



## A. MODEL-DATA COMPARISON FOR PRESENT DAY CLIMATE

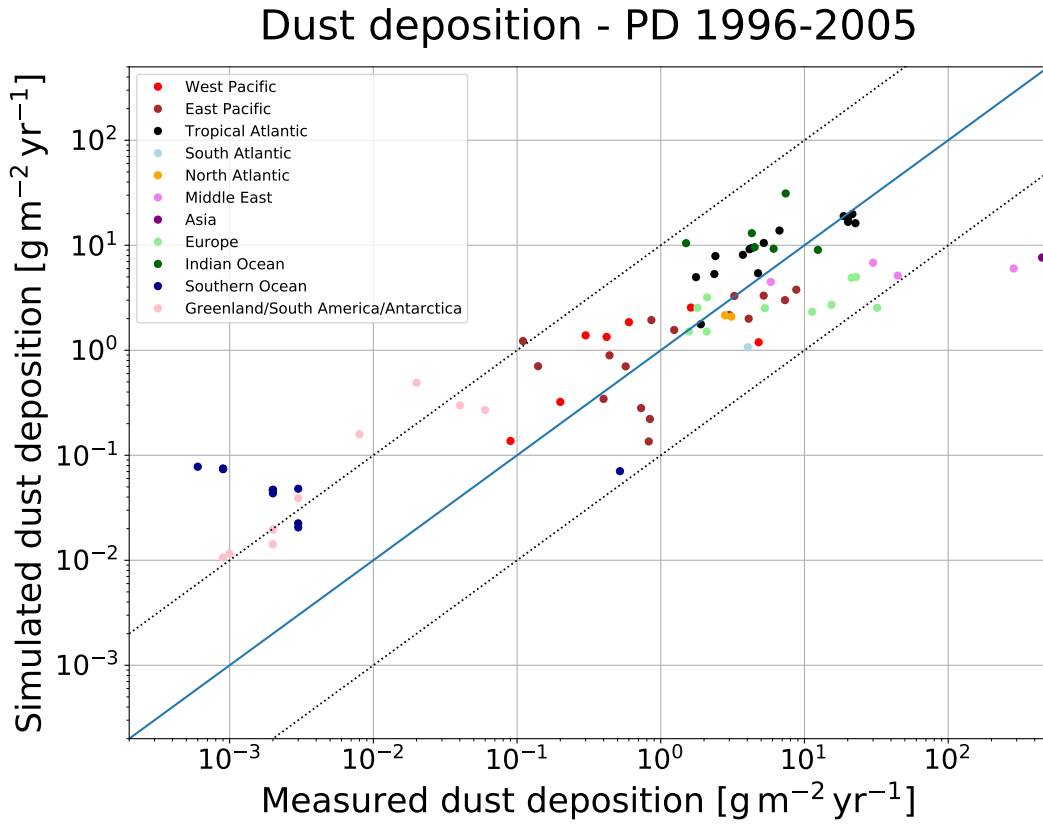


**Figure A.1.** Scatterplot showing the comparison of the total dust deposition simulated by our model to observational data from 84 sites [Huneus et al. (2011)] for present-day climate conditions. The plot suggests in particular in the West Pacific an improvement of the model used in our study compared to the older version used by Stanelle et al. (2014).

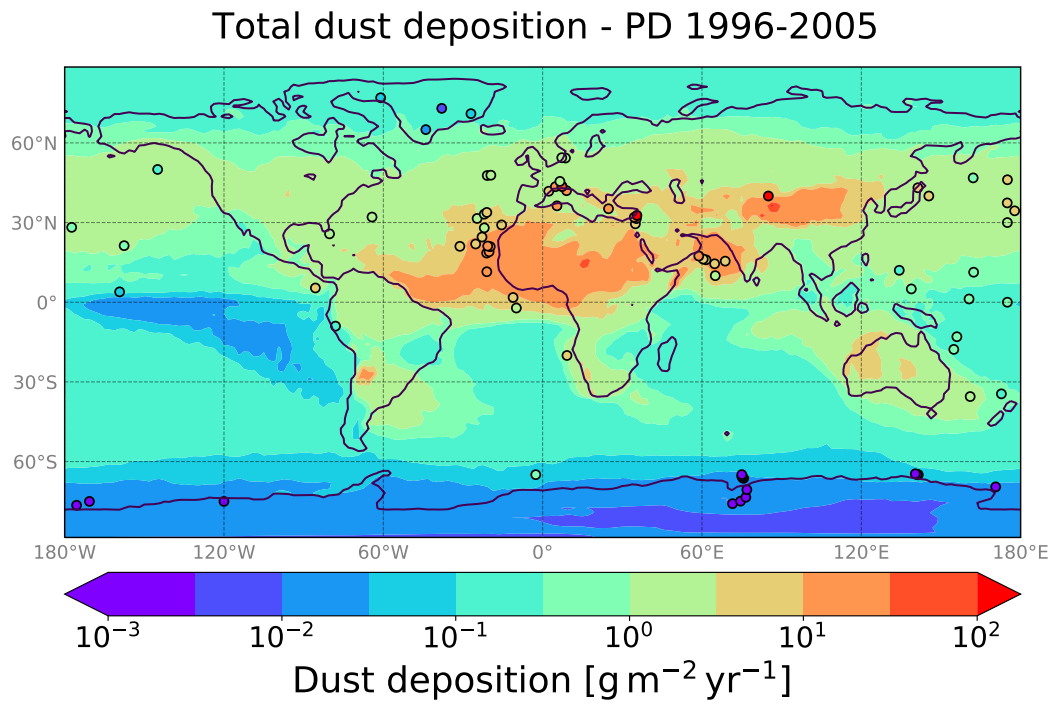


**Figure A.2.** The map shows dust deposition data from 84 sites (points, Huneus et al. (2011)) compared to the dust deposition simulated by our model for present-day climate conditions.

## B. SOURCE STRENGTH INCREASE VS. PARTICLE LIFETIME

### LIFETIME

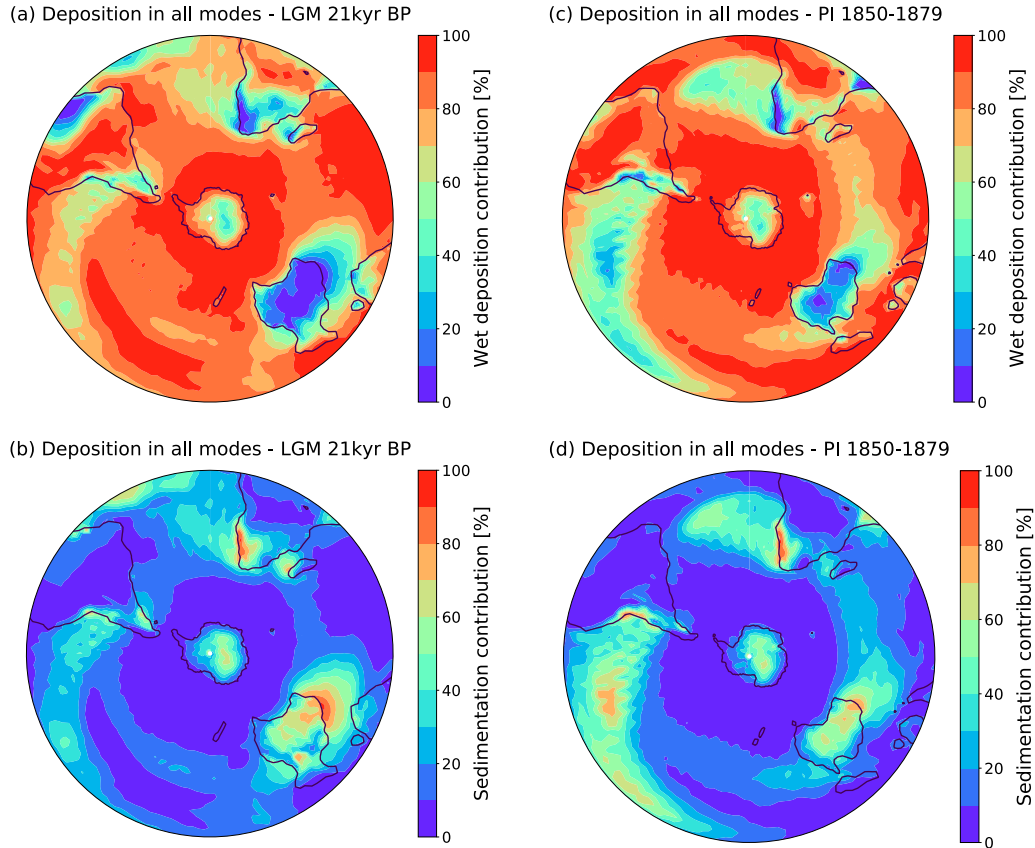


**Figure B.1.** Contribution of sedimentation and wet deposition to the total dust deposition for LGM (a, b) and PI (c, d) in percent.

Generally, the results in chapter 4 indicate globally a particle lifetime increase (all modes) of +0.53 days during the LGM, and specifically +0.31 days in the Southern Hemisphere, which are attributed to the generally drier climate. However Fig. 4.5a (Chapter 4) suggests opposing trends for the Pacific SO (increasing trend) and the Atlantic SO (decreasing trend) region. In the following, the discussion is based on values for burden and (wet) deposition for the two regions stated above for both PI and LGM. As shown in Fig. B.1 and Table 4.5 (Chapter 4), wet deposition is the predominant deposition mechanism (> 90%) in the Southern Ocean region and consequently, contributions from dry deposition and sedimentation are neglected. The following particle lifetimes  $\tau$  can be obtained:

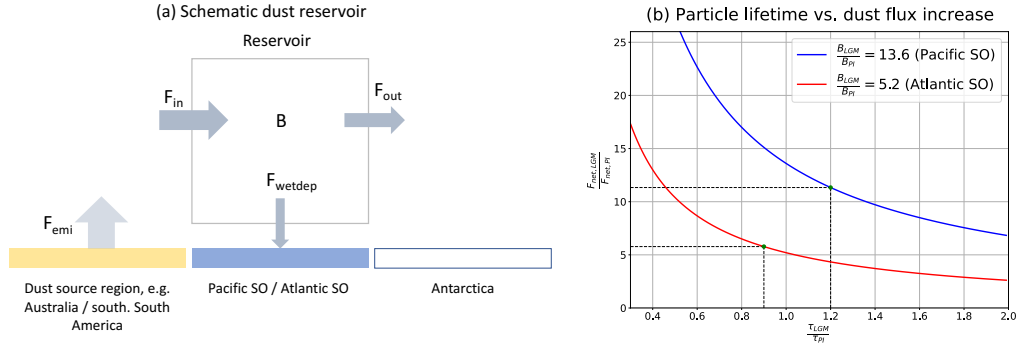


**Figure B.2.** Schematic representation of the atmospheric dust reservoir over the Pacific SO / Atlantic SO containing the dust burden  $B$  and all fluxes into and out of the reservoir (a). Figure (b) shows the net flux ratio depending on the particle lifetime ratio in order to get the simulated dust burden ratio of 13.6 for the Pacific SO region, respectively, 5.2 for the Atlantic SO region.

- $\tau_{LGM,Atlantic,SO} = 6.8$  d
- $\tau_{PI,Atlantic,SO} = 7.4$  d
- $\tau_{LGM,Pacific,SO} = 9$  d
- $\tau_{PI,Pacific,SO} = 7.4$  d

It shall be taken up on the debate about the relative importance of changes in source strength and particle lifetime in determining the LGM increase in dust concentration (Fischer et al., 2007; Wolff et al., 2010). Although an ultimate answer on this matter will not be possible, the goal is to get at least some new insights in the scope of our simulations. Therefore, a highly simplified description is used (see B.2a), assuming the atmosphere above the Pacific SO, respectively, Atlantic SO to be a dust reservoir with capacity  $B$  (burden), which is filled by the dust influx  $F_{in}$  and loses mass due to wet deposition  $F_{wetdep}$  and dust transport to Antarctica  $F_{out}$ . Here,  $F_{in}$  is assumed to be proportional to the dust source strength  $F_{emi}$ . Consequently, the temporal change of  $B$  can be described by

$$\frac{dB(t)}{dt} = F_{in} - F_{wetdep} - F_{out} = -F_{wetdep} + (F_{in} - F_{out}) = -F_{wetdep} + F_{net} \quad (15)$$

The wet deposition flux  $F_{wetdep}$  can be assumed to be proportional to  $B$  with a decay constant  $\lambda$  (inverse particle lifetime) and we can finally write

$$\frac{dB(t)}{dt} = -\lambda B(t) + F_{net}, \quad (16)$$

with the solution

$$B(t) = Ae^{-\lambda t} + \frac{F_{\text{net}}}{\lambda} \quad (17)$$

Since we are interested in the long-term equilibrium between influxes and losses, we write

$$\lim_{t \rightarrow \infty} B(t) = \frac{F_{\text{net}}}{\lambda} \quad (18)$$

Consequently, the burden is determined by the net influx and the decay rate. For the LGM/PI ratio, we can write

$$\frac{B_{\text{LGM}}}{B_{\text{PI}}} = \frac{\lambda_{\text{PI}}}{\lambda_{\text{LGM}}} \frac{F_{\text{net,LGM}}}{F_{\text{net,PI}}} \quad (19)$$

Since the high burden ratio is apparently required in the model for the increased dust concentration over Antarctica, the interplay between the particle lifetime ratio and the net influx ratio can be investigated now. Figure B.2b shows the results for the LGM/PI burden ratio for the Pacific SO region (13.6) and the Atlantic SO region (5.2). The plot suggests that the more the particle lifetime increases, the less of a source strength increase is necessary (and vice versa) to obtain the simulated dust burden ratio. The values for the lifetime and burden ratio are calculated based on the values given above.

## REFERENCES

- Abdul-Razzak, H. and Ghan, S.: A parameterization of aerosol activation: 2. Multiple aerosol types, *Journal of Geophysical Research*, 105, 6837–6844, <https://doi.org/10.1029/1999JD901161>, 2000.
- Adams, J. M. and Faure, H.: A new estimate of changing carbon storage on land since the last glacial maximum, based on global land ecosystem reconstruction, *Global and Planetary Change*, 16-17, 3–24, [https://doi.org/10.1016/S0921-8181\(98\)00003-4](https://doi.org/10.1016/S0921-8181(98)00003-4), 1998.
- Adebiyi, A. A. and Kok, J. F.: Climate models miss most of the coarse dust in the atmosphere, *Science Advances*, 6, eaaz9507, <https://doi.org/10.1126/sciadv.aaz9507>, 2020.
- Albani, S. and Mahowald, N. M.: Paleodust Insights into Dust Impacts on Climate, *Journal of Climate*, 32, 7897–7913, <https://doi.org/10.1175/JCLI-D-18-0742.1>, 2019.
- Albani, S., Mahowald, N. M., Delmonte, B., Maggi, V., and Winckler, G.: Comparing modeled and observed changes in mineral dust transport and deposition to Antarctica between the Last Glacial Maximum and current climates, *Climate Dynamics*, 38, 1731–1755, <https://doi.org/10.1007/s00382-011-1139-5>, 2012.
- Albani, S., Mahowald, N. M., Perry, A. T., Scanza, R. A., Zender, C. S., Heavens, N. G., Maggi, V., Kok, J. F., and Otto-Bliesner, B. L.: Improved dust representation in the Community Atmosphere Model, *Journal of Advances in Modeling Earth Systems*, 6, 541–570, <https://doi.org/https://doi.org/10.1002/2013MS000279>, \_eprint: <https://agupubs.onlinelibrary.wiley.com/doi/pdf/10.1002/2013MS000279>, 2014.
- Albani, S., Mahowald, N. M., Murphy, L. N., Raiswell, R., Moore, J. K., Anderson, R. F., McGee, D., Bradtmiller, L. I., Delmonte, B., Hesse, P. P., and Mayewski, P. A.: Paleodust variability since the Last Glacial Maximum and implications for iron inputs to the ocean, *Geophysical Research Letters*, 43, 3944–3954, <https://doi.org/https://doi.org/10.1002/2016GL067911>, \_eprint: <https://agupubs.onlinelibrary.wiley.com/doi/pdf/10.1002/2016GL067911>, 2016.
- Alley, R. B. and Bender, M. L.: Greenland Ice Cores: Frozen in Time, *Scientific American*, <https://doi.org/10.1038/scientificamerican0298-80>, 1998.
- Baines, P. and Palmer, T. N.: Rationale for a new physically-based parametrization of subgrid-scale orographic effects, <https://doi.org/10.21957/h4h36b3u>, pages: 11 Place: Shinfield Park, Reading Publisher: ECMWF, 1990.
- Balkanski, Y., Schulz, M., Claquin, T., and Guibert, S.: Reevaluation of Mineral aerosol radiative forcings suggests a better agreement with satellite and AERONET data, *Atmospheric Chemistry and Physics*, 7, 81–95, <https://doi.org/10.5194/acp-7-81-2007>, publisher: Copernicus GmbH, 2007.
- Bartlein, P. J., Harrison, S. P., Brewer, S., Connor, S., Davis, B. A. S., Gajewski, K., Guiot, J., Harrison-Prentice, T. I., Henderson, A., Peyron, O., Prentice, I. C., Scholze, M., Seppä, H., Shuman, B., Sugita, S., Thompson, R. S., Viau, A. E., Williams, J., and Wu, H.: Pollen-based continental climate reconstructions at 6 and 21 ka: a global synthesis, *Climate Dynamics*, 37, 775–802, <https://doi.org/10.1007/s00382-010-0904-1>, 2011.
- Basile, I., Grousset, F. E., Revel, M., Petit, J. R., Biscaye, P. E., and Barkov, N. I.: Patagonian origin of glacial dust deposited in East Antarctica (Vostok and Dome C) during glacial stages 2, 4 and 6, *Earth and Planetary Science Letters*, 146, 573–589, [https://doi.org/10.1016/S0012-821X\(96\)00255-5](https://doi.org/10.1016/S0012-821X(96)00255-5), 1997.
- Bathiany, S., Dijkstra, H., Crucifix, M., Dakos, V., Brovkin, V., Williamson, M. S., Lenton, T. M., and Scheffer, M.: Beyond bifurcation: using complex models to understand and predict abrupt climate change, *Dynamics and Statistics of the Climate System*, 1, dzw004, <https://doi.org/10.1093/climsys/dzw004>, 2016.
- Berner, R. A., Lasaga, A. C., and Garrels, R. M.: The carbonate-silicate geochemical cycle and its effect on atmospheric carbon dioxide over the past 100 million years, *American Journal of Science*, 283, 641–683, <https://doi.org/10.2475/ajs.283.7.641>, publisher: American Journal of Science Section: Articles, 1983.

## References

- Birnstiel, T., Dullemond, C. P., and Brauer, F.: Gas- and dust evolution in protoplanetary disks, *Astronomy & Astrophysics*, 513, A79, <https://doi.org/10.1051/0004-6361/200913731>, publisher: EDP Sciences, 2010.
- Birnstiel, T., Klahr, H., and Ercolano, B.: A simple model for the evolution of the dust population in protoplanetary disks, *Astronomy & Astrophysics*, 539, A148, <https://doi.org/10.1051/0004-6361/201118136>, publisher: EDP Sciences, 2012.
- Biscaye, P. E., Grousset, F. E., Revel, M., Van der Gaast, S., Zielinski, G. A., Vaars, A., and Kukla, G.: Asian provenance of glacial dust (stage 2) in the Greenland Ice Sheet Project 2 Ice Core, Summit, Greenland, *Journal of Geophysical Research: Oceans*, 102, 26765–26781, <https://doi.org/10.1029/97JC01249>, \_eprint: <https://onlinelibrary.wiley.com/doi/pdf/10.1029/97JC01249>, 1997.
- Bony, S., Colman, R., Kattsov, V., Allan, R., Bretherton, C., Dufresne, J., Hall, A., Hallegatte, S., Holland, M., Ingram, W., Randall, D., Soden, B., Tselioudis, G., and Webb, M.: How well do we understand and evaluate climate change feedback processes?, *Journal of Climate*, p. 3445, <https://doi.org/10.1175/JCLI3819.1>, publisher: American Meteorological Society, 2006.
- Boucher, O.: *Atmospheric Aerosols: Properties and Climate Impacts*, Springer Netherlands, <https://doi.org/10.1007/978-94-017-9649-1>, 2015.
- Bourke, W.: An Efficient, One-Level, Primitive-Equation Spectral Model, *Monthly Weather Review*, 100, 683–689, [https://doi.org/10.1175/1520-0493\(1972\)100<0683:AEOPSM>2.3.CO;2](https://doi.org/10.1175/1520-0493(1972)100<0683:AEOPSM>2.3.CO;2), publisher: American Meteorological Society Section: Monthly Weather Review, 1972.
- Boyd, P. W. and Bressac, M.: Developing a test-bed for robust research governance of geoengineering: the contribution of ocean iron biogeochemistry, *Philosophical Transactions of the Royal Society A: Mathematical, Physical and Engineering Sciences*, 374, 20150299, <https://doi.org/10.1098/rsta.2015.0299>, 2016.
- Braconnot, P., Otto-Bliesner, B., Harrison, S., Joussaume, S., Peterchmitt, J.-Y., Abe-Ouchi, A., Crucifix, M., Driesschaert, E., Fichefet, T., Hewitt, C. D., Kageyama, M., Kitoh, A., L ain e, A., Loutre, M.-F., Marti, O., Merkel, U., Ramstein, G., Valdes, P., Weber, S. L., Yu, Y., and Zhao, Y.: Results of PMIP2 coupled simulations of the Mid-Holocene and Last Glacial Maximum &ndash; Part 1: experiments and large-scale features, *Climate of the Past*, 3, 261–277, <https://doi.org/10.5194/cp-3-261-2007>, publisher: Copernicus GmbH, 2007.
- Braconnot, P., Harrison, S. P., Kageyama, M., Bartlein, P. J., Masson-Delmotte, V., Abe-Ouchi, A., Otto-Bliesner, B., and Zhao, Y.: Evaluation of climate models using palaeoclimatic data, *Nature Climate Change*, 2, 417–424, <https://doi.org/10.1038/nclimate1456>, number: 6 Publisher: Nature Publishing Group, 2012.
- Brinkop, S. and Roeckner, E.: Sensitivity of a general circulation model to parameterizations of cloud–turbulence interactions in the atmospheric boundary layer, *Tellus A*, 47, 197–220, <https://doi.org/https://doi.org/10.1034/j.1600-0870.1995.t01-1-00004.x>, \_eprint: <https://onlinelibrary.wiley.com/doi/pdf/10.1034/j.1600-0870.1995.t01-1-00004.x>, 1995.
- Broecker, W. S. and Denton, G. H.: The role of ocean-atmosphere reorganizations in glacial cycles, *Geochimica et Cosmochimica Acta*, 53, 2465–2501, [https://doi.org/10.1016/0016-7037\(89\)90123-3](https://doi.org/10.1016/0016-7037(89)90123-3), aDS Bibcode: 1989GeCoA..53.2465B, 1989.
- Buizert, C., Fudge, T. J., Roberts, W., Ritz, C., Lefebvre, E., Sherriff-Tadano, S., Abe-Ouchi, A., Martin, C., Corr, H. F. J., Severinghaus, J. P., Beaudette, R., Steig, E. J., Epifanio, J., Siler, N., Brook, E., Kawamura, K., Oyabu, I., Sowers, T., Sigl, M., Severi, M., and Dunbar, N.: How cold was Antarctica during the Last Glacial Maximum?, 2019, C13B–04, URL <https://ui.adsabs.harvard.edu/abs/2019AGUFM.C13B..04B>, conference Name: AGU Fall Meeting Abstracts ADS Bibcode: 2019AGUFM.C13B..04B, 2019.
- Cakmur, R. V., Miller, R. L., Perlwitz, J., Geogdzhayev, I. V., Ginoux, P., Koch, D., Kohfeld, K. E., Tegen, I., and Zender, C. S.: Constraining the magnitude of the global dust cycle by minimizing the difference between a model and observations, *Journal of Geophysical Research: Atmospheres*, 111, <https://doi.org/10.1029/2005JD005791>, \_eprint: <https://onlinelibrary.wiley.com/doi/pdf/10.1029/2005JD005791>, 2006.
- Cao, J., Wang, B., and Liu, J.: Attribution of the Last Glacial Maximum climate formation, *Climate Dynamics*, 53, 1661–1679, <https://doi.org/10.1007/s00382-019-04711-6>, 2019.

## References

---

- Capua, G. D. and Coumou, D.: Changes in meandering of the Northern Hemisphere circulation, *Environmental Research Letters*, 11, 094 028, <https://doi.org/10.1088/1748-9326/11/9/094028>, publisher: IOP Publishing, 2016.
- Carslaw, K. S., Boucher, O., Spracklen, D. V., Mann, G. W., Rae, J. G. L., Woodward, S., and Kulmala, M.: A review of natural aerosol interactions and feedbacks within the Earth system, *Atmospheric Chemistry and Physics*, 10, 1701–1737, <https://doi.org/10.5194/acp-10-1701-2010>, 2010.
- Castang M., C., Lain, S., Garcia, D., and Sommerfeld, M.: Aerodynamic coefficients of irregular non-spherical particles at intermediate Reynolds numbers, *Powder Technology*, 402, 117 341, <https://doi.org/10.1016/j.powtec.2022.117341>, 2022.
- Cheng, T., Peng, Y., Feichter, J., and Tegen, I.: An improvement on the dust emission scheme in the global aerosol-climate model ECHAM5-HAM, *Atmos. Chem. Phys.*, p. 13, 2008.
- Clark, P. U. and Mix, A. C.: Ice sheets and sea level of the Last Glacial Maximum, *Quaternary Science Reviews*, 21, 1–7, [https://doi.org/10.1016/S0277-3791\(01\)00118-4](https://doi.org/10.1016/S0277-3791(01)00118-4), 2002.
- Clark, P. U., Dyke, A. S., Shakun, J. D., Carlson, A. E., Clark, J., Wohlfarth, B., Mitrovica, J. X., Hostetler, S. W., and McCabe, A. M.: The Last Glacial Maximum, *Science*, 325, 710–714, <https://doi.org/10.1126/science.1172873>, publisher: American Association for the Advancement of Science Section: Research Article, 2009.
- CLIMAP PROJECT MEMBERS: The Surface of the Ice-Age Earth, *Science*, 191, 1131–1137, <https://doi.org/10.1126/science.191.4232.1131>, publisher: American Association for the Advancement of Science, 1976.
- Croft, B., Lohmann, U., Martin, R. V., Stier, P., Wurzler, S., Feichter, J., Posselt, R., and Ferrachat, S.: Aerosol size-dependent below-cloud scavenging by rain and snow in the ECHAM5-HAM, *Atmospheric Chemistry and Physics*, 9, 4653–4675, <https://doi.org/10.5194/acp-9-4653-2009>, publisher: Copernicus GmbH, 2009.
- Croft, B., Lohmann, U., Martin, R. V., Stier, P., Wurzler, S., Feichter, J., Hoose, C., Heikkilä, U., van Donkelaar, A., and Ferrachat, S.: Influences of in-cloud aerosol scavenging parameterizations on aerosol concentrations and wet deposition in ECHAM5-HAM, *Atmospheric Chemistry and Physics*, 10, 1511–1543, <https://doi.org/10.5194/acp-10-1511-2010>, publisher: Copernicus GmbH, 2010.
- De Deckker, P., Norman, M., Goodwin, I. D., Wain, A., and Gingele, F. X.: Lead isotopic evidence for an Australian source of aeolian dust to Antarctica at times over the last 170,000 years, *Palaeogeography, Palaeoclimatology, Palaeoecology*, 285, 205–223, <https://doi.org/10.1016/j.palaeo.2009.11.013>, 2010.
- Delmonte, B., Petit, J., and Maggi, V.: Glacial to Holocene implications of the new 27000-year dust record from the EPICA Dome C (East Antarctica) ice core, *Climate Dynamics*, 18, 647–660, <https://doi.org/10.1007/s00382-001-0193-9>, 2002.
- Delmonte, B., Petit, J.-R., Andersen, K., Basile-Doelsch, I., Maggi, V., and Lipenkov, V.: Dust size evidence for opposite regional atmospheric circulation changes over East Antarctica during the last climatic transition, *Climate Dynamics*, 23, 427–438, <https://doi.org/10.1007/s00382-004-0450-9>, 2004.
- Delmonte, B., Andersson, P. S., Hansson, M., Schöberg, H., Petit, J. R., Basile-Doelsch, I., and Maggi, V.: Aeolian dust in East Antarctica (EPICA-Dome C and Vostok): Provenance during glacial ages over the last 800 kyr, *Geophysical Research Letters*, 35, <https://doi.org/10.1029/2008GL033382>, \_eprint: <https://onlinelibrary.wiley.com/doi/pdf/10.1029/2008GL033382>, 2008.
- Dietrich, R. V.: Impact Abrasion of Harder by Softer Materials, *The Journal of Geology*, 85, 242–246, <https://doi.org/10.1086/628289>, publisher: The University of Chicago Press, 1977.
- Dong, B. and Valdes, P. J.: Climates at the Last Glacial Maximum: Influence of Model Horizontal Resolution, *Journal of Climate*, 13, 1554–1573, [https://doi.org/10.1175/1520-0442\(2000\)013<1554:CATLGM>2.0.CO;2](https://doi.org/10.1175/1520-0442(2000)013<1554:CATLGM>2.0.CO;2), publisher: American Meteorological Society Section: Journal of Climate, 2000.
- Dortmans, B., Langford, W. F., and Willms, A. R.: An energy balance model for paleoclimate transitions, *Climate of the Past*, 15, 493–520, <https://doi.org/10.5194/cp-15-493-2019>, publisher: Copernicus GmbH, 2019.

## References

- Duce, R., Liss, P., Merrill, J., Atlas, E., Buat-Menard, P., Hicks, B., Miller, J., Prospero, J., Arimoto, R., Church, T., Ellis, W., Galloway, J., Hansen, L., Jickells, T., Knap, A., Reinhardt, K., Schneider, B., Soudine, A., Tokos, J., and Zhou, M.: The atmospheric input of trace species to the World ocean, *Global Biogeochemical Cycles*, 5, 193–259, <https://doi.org/10.1029/91GB01778>, 1991.
- Dufresne, J.-L., Gautier, C., Ricchiazzi, P., and Fouquart, Y.: Longwave Scattering Effects of Mineral Aerosols, *Journal of the Atmospheric Sciences*, 59, 1959–1966, [https://doi.org/10.1175/1520-0469\(2002\)059<1959:LSEOMA>2.0.CO;2](https://doi.org/10.1175/1520-0469(2002)059<1959:LSEOMA>2.0.CO;2), publisher: American Meteorological Society Section: *Journal of the Atmospheric Sciences*, 2002.
- Dullemond, C. P. and Dominik, C.: Dust coagulation in protoplanetary disks: A rapid depletion of small grains, *Astronomy & Astrophysics*, 434, 971–986, <https://doi.org/10.1051/0004-6361:20042080>, number: 3 Publisher: EDP Sciences, 2005.
- Durack, P. J. and Taylor, K. E.: input4MIPs.CMIP6.CMIP.PCMDI.PCMDI-AMIP-1-1-6, <https://doi.org/10.22033/ESGF/input4MIPs.12381>, publisher: Earth System Grid Federation type: dataset, 2019.
- Eliassen, A.: On the vertical circulation in frontal zones, 24, 147–160, 1962.
- Esposito, F., Molinaro, R., Popa, C. I., Molfese, C., Cozzolino, F., Marty, L., Taj-Eddine, K., Di Achille, G., Franzese, G., Silvestro, S., and Ori, G. G.: The role of the atmospheric electric field in the dust-lifting process, *Geophysical Research Letters*, 43, 5501–5508, <https://doi.org/10.1002/2016GL068463>, \_eprint: <https://onlinelibrary.wiley.com/doi/pdf/10.1002/2016GL068463>, 2016.
- Evans, S., Dawson, E., and Ginoux, P.: Linear Relation Between Shifting ITCZ and Dust Hemispheric Asymmetry, *Geophysical Research Letters*, 47, e2020GL090499, <https://doi.org/https://doi.org/10.1029/2020GL090499>, \_eprint: <https://agupubs.onlinelibrary.wiley.com/doi/pdf/10.1029/2020GL090499>, 2020.
- Farrera, I., Harrison, S., Prentice, I., Ramstein, G., Joel, G., Bartlein, P., Raymonde, B., Bush, M., Cramer, W., Von Grafenstein, U., Holmgren, K., Henry, H., Hope, G., Jolly, D., Lauritzen, S., Ono, Y., Pinot, S., Stute, M., and yu, g.: Tropical climates at the Last Glacial Maximum: A new synthesis of terrestrial palaeoclimate data. I. Vegetation, lake-levels and geochemistry, *Climate Dynamics*, 15, 823–856, <https://doi.org/10.1007/s003820050317>, 1999.
- Ferreira, D., Marshall, J., and Rose, B.: Climate Determinism Revisited: Multiple Equilibria in a Complex Climate Model, *Journal of Climate*, 24, 992–1012, <https://doi.org/10.1175/2010JCLI3580.1>, publisher: American Meteorological Society Section: *Journal of Climate*, 2011.
- Fieguth, P.: Systems Theory, in: *An Introduction to Complex Systems: Society, Ecology, and Nonlinear Dynamics*, edited by Fieguth, P., pp. 13–39, Springer International Publishing, Cham, [https://doi.org/10.1007/978-3-319-44606-6\\_3](https://doi.org/10.1007/978-3-319-44606-6_3), 2017.
- Fischer, H., Siggaard-Andersen, M.-L., Ruth, U., Röthlisberger, R., and Wolff, E.: Glacial/interglacial changes in mineral dust and sea-salt records in polar ice cores: Sources, transport, and deposition, *Reviews of Geophysics*, 45, <https://doi.org/10.1029/2005RG000192>, \_eprint: <https://onlinelibrary.wiley.com/doi/pdf/10.1029/2005RG000192>, 2007.
- Fletcher, B.: The erosion of dust by an airflow, *Journal of Physics D: Applied Physics*, 9, 913–924, <https://doi.org/10.1088/0022-3727/9/6/005>, publisher: IOP Publishing, 1976.
- Fuhrer, K., Wolff, E. W., and Johnsen, S. J.: Timescales for dust variability in the Greenland Ice Core Project (GRIP) ice core in the last 100,000 years, *Journal of Geophysical Research: Atmospheres*, 104, 31 043–31 052, <https://doi.org/10.1029/1999JD900929>, \_eprint: <https://onlinelibrary.wiley.com/doi/pdf/10.1029/1999JD900929>, 1999.
- García-Gaines, R. A. and Frankenstein, S.: USCS and the USDA Soil Classification System : Development of a mapping scheme, REPORT, Cold Regions Research and Engineering Laboratory (U.S.), URL <https://erdc-library.erdcren.mil/jspui/handle/11681/5485>, accepted: 2016-03-21T16:37:47Z Publication Title: This Digital Resource was created in Microsoft Word and Adobe Acrobat, 2015.
- Giorgetta, M. A., Roeckner, E., Mauritsen, T., Bader, J., Crueger, T., Esch, M., Rast, S., Kornblueh, L., Schmidt, H., Kinne, S., Hohenegger, C., Möbis, B., Krismer, T., Wieners, H., and Stevens, B.: The atmospheric general circulation model ECHAM6: Model description, *Reports on Earth System Science*, p. 177, 2013.

## References

---

- Gordon, A. L.: Oceanography of Antarctic waters, in: Antarctic Research Series, edited by Reid, J. L., vol. 15, pp. 169–203, American Geophysical Union, Washington, D. C., <https://doi.org/10.1029/AR015p0169>, 1971.
- Goudie, A. S.: The History and Nature of Wind Erosion in Deserts, *Annual Review of Earth and Planetary Sciences*, 36, 97–119, <https://doi.org/10.1146/annurev.earth.36.031207.124353>, [\\_eprint: https://doi.org/10.1146/annurev.earth.36.031207.124353](https://doi.org/10.1146/annurev.earth.36.031207.124353), 2008.
- Gras, J. L.: AEROSOLS | Climatology of Tropospheric Aerosols, pp. 13–20, Elsevier, 2003.
- Haberzettl, T., Anselmetti, F. S., Bowen, S. W., Fey, M., Mayr, C., Zolitschka, B., Ariztegui, D., Mauz, B., Ohlendorf, C., Kastner, S., Lücke, A., Schäbitz, F., and Wille, M.: Late Pleistocene dust deposition in the Patagonian steppe - extending and refining the paleoenvironmental and tephrochronological record from Laguna Potrok Aike back to 55ka, *Quaternary Science Reviews*, 28, 2927–2939, <https://doi.org/10.1016/j.quascirev.2009.07.021>, 2009.
- Hagemann, S. and Stacke, T.: Impact of the soil hydrology scheme on simulated soil moisture memory, *Climate Dynamics*, 44, 1731–1750, <https://doi.org/10.1007/s00382-014-2221-6>, 2015.
- Hand, J. L., Mahowald, N. M., Chen, Y., Siefert, R. L., Luo, C., Subramaniam, A., and Fung, I.: Estimates of atmospheric-processed soluble iron from observations and a global mineral aerosol model: Biogeochemical implications, *Journal of Geophysical Research (Atmospheres)*, 109, D17 205, <https://doi.org/10.1029/2004JD004574>, aDS Bibcode: 2004JGRD..10917205H, 2004.
- Hargreaves, J., Annan, J., Yoshimori, M., and Abe-Ouchi, A.: Can the Last Glacial Maximum constrain climate sensitivity?, *Geophysical Research Letters*, 39, 24 702, <https://doi.org/10.1029/2012GL053872>, 2012.
- Harrison, R. G., Barth, E., Esposito, F., Merrison, J., Montmessin, F., Aplin, K. L., Borlina, C., Berthelier, J. J., Déprez, G., Farrell, W. M., Houghton, I. M. P., Renno, N. O., Nicoll, K. A., Tripathi, S. N., and Zimmerman, M.: Applications of Electrified Dust and Dust Devil Electrodynamics to Martian Atmospheric Electricity, *Space Science Reviews*, 203, 299–345, <https://doi.org/10.1007/s11214-016-0241-8>, 2016.
- Heintzenberg, J.: AEROSOLS | Physics and Chemistry of Aerosols, in: *Encyclopedia of Atmospheric Sciences*, pp. 34–40, Elsevier, 2003.
- Hoffert, M. I. and Covey, C.: Deriving global climate sensitivity from palaeoclimate reconstructions, *Nature*, 360, 573–576, <https://doi.org/10.1038/360573a0>, number: 6404 Publisher: Nature Publishing Group, 1992.
- Holton, J.: *An Introduction to Dynamic Meteorology*, vol. 88, 4 edn., URL <https://www.elsevier.com/books/an-introduction-to-dynamic-meteorology/holton/978-0-12-354015-7>, 2004.
- Hovan, S., Rea, D., and Pisias, N.: Late Pleistocene Continental Climate and Oceanic Variability Recorded in Northwest Pacific Sediments, *Paleoceanography*, 6, 349–370, <https://doi.org/10.1029/91PA00559>, 1991.
- Hulton, N. R. J., Purves, R. S., McCulloch, R. D., Sugden, D. E., and Bentley, M. J.: The Last Glacial Maximum and deglaciation in southern South America, *Quaternary Science Reviews*, 21, 233–241, [https://doi.org/10.1016/S0277-3791\(01\)00103-2](https://doi.org/10.1016/S0277-3791(01)00103-2), 2002.
- Huneeus, N., Schulz, M., Balkanski, Y., Griesfeller, J., Prospero, J., Kinne, S., Bauer, S., Boucher, O., Chin, M., Dentener, F., Diehl, T., Easter, R., Fillmore, D., Ghan, S., Ginoux, P., Grini, A., Horowitz, L., Koch, D., Krol, M. C., Landing, W., Liu, X., Mahowald, N., Miller, R., Morcrette, J.-J., Myhre, G., Penner, J., Perlwitz, J., Stier, P., Takemura, T., and Zender, C. S.: Global dust model intercomparison in AeroCom phase I, *Atmospheric Chemistry and Physics*, 11, 7781–7816, <https://doi.org/10.5194/acp-11-7781-2011>, 2011.
- James, I. N.: The Antarctic drainage flow: implications for hemispheric flow on the Southern Hemisphere, *Antarctic Science*, 1, 279–290, <https://doi.org/10.1017/S0954102089000404>, number: 03 Publisher: Cambridge University Press, 1989.
- Kageyama, M., Albani, S., Braconnot, P., Harrison, S. P., Hopcroft, P. O., Ivanovic, R. F., Lambert, F., Marti, O., Peltier, W. R., Peterschmitt, J.-Y., Roche, D. M., Tarasov, L., Zhang, X., Brady, E. C., Haywood, A. M., LeGrande, A. N., Lunt, D. J., Mahowald, N. M., Mikolajewicz, U., Nisancioglu, K. H., Otto-Bliesner, B. L., Renssen, H., Tomas, R. A., Zhang, Q., Abe-Ouchi, A., Bartlein, P. J., Cao, J., Li, Q., Lohmann, G., Ohgaito, R., Shi, X., Volodin, E., Yoshida,

## References

---

- K., Zhang, X., and Zheng, W.: The PMIP4 contribution to CMIP6 – Part 4: Scientific objectives and experimental design of the PMIP4-CMIP6 Last Glacial Maximum experiments and PMIP4 sensitivity experiments, *Geoscientific Model Development*, 10, 4035–4055, <https://doi.org/10.5194/gmd-10-4035-2017>, 2017.
- Kageyama, M., Harrison, S. P., Kapsch, M.-L., Lofverstrom, M., Lora, J. M., Mikolajewicz, U., Sherriff-Tadano, S., Vadsaria, T., Abe-Ouchi, A., Bouttes, N., Chandan, D., Gregoire, L. J., Ivanovic, R. F., Izumi, K., LeGrande, A. N., Lhardy, F., Lohmann, G., Morozova, P. A., Ohgaito, R., Paul, A., Peltier, W. R., Poulsen, C. J., Quiquet, A., Roche, D. M., Shi, X., Tierney, J. E., Valdes, P. J., Volodin, E., and Zhu, J.: The PMIP4 Last Glacial Maximum experiments: preliminary results and comparison with the PMIP3 simulations, *Climate of the Past*, 17, 1065–1089, <https://doi.org/10.5194/cp-17-1065-2021>, publisher: Copernicus GmbH, 2021.
- Knippertz, P. and Todd, M. C.: Mineral dust aerosols over the Sahara: Meteorological controls on emission and transport and implications for modeling, *Reviews of Geophysics*, 50, <https://doi.org/10.1029/2011RG000362>, \_eprint: <https://onlinelibrary.wiley.com/doi/pdf/10.1029/2011RG000362>, 2012.
- Koffman, B. G., Goldstein, S. L., Winckler, G., Borunda, A., Kaplan, M. R., Bolge, L., Cai, Y., Recasens, C., Koffman, T. N. B., and Vallelonga, P.: New Zealand as a source of mineral dust to the atmosphere and ocean, *Quaternary Science Reviews*, 251, 106659, <https://doi.org/10.1016/j.quascirev.2020.106659>, 2021.
- Kohfeld, K. E. and Harrison, S. P.: DIRTMAP: the geological record of dust, *Earth-Science Reviews*, 54, 81–114, [https://doi.org/10.1016/S0012-8252\(01\)00042-3](https://doi.org/10.1016/S0012-8252(01)00042-3), 2001.
- Kohfeld, K. E. and Ridgwell, A.: Glacial-interglacial variability in atmospheric CO<sub>2</sub>, in: *Geophysical Monograph Series*, vol. 187, pp. 251–286, American Geophysical Union, Washington, D. C., <https://doi.org/10.1029/2008GM000845>, 2009.
- Kohfeld, K. E., Graham, R. M., de Boer, A. M., Sime, L. C., Wolff, E. W., Le Quéré, C., and Bopp, L.: Southern Hemisphere westerly wind changes during the Last Glacial Maximum: paleo-data synthesis, *Quaternary Science Reviews*, 68, 76–95, <https://doi.org/10.1016/j.quascirev.2013.01.017>, 2013.
- Kok, J. F., Ridley, D. A., Zhou, Q., Miller, R. L., Zhao, C., Heald, C. L., Ward, D. S., Albani, S., and Haustein, K.: Smaller desert dust cooling effect estimated from analysis of dust size and abundance, *Nature Geoscience*, 10, 274–278, <https://doi.org/10.1038/ngeo2912>, 2017.
- Kok, J. F., Adebisi, A. A., Albani, S., Balkanski, Y., Checa-Garcia, R., Chin, M., Colarco, P. R., Hamilton, D. S., Huang, Y., Ito, A., Klose, M., Leung, D. M., Li, L., Mahowald, N. M., Miller, R. L., Obiso, V., Pérez García-Pando, C., Rocha-Lima, A., Wan, J. S., and Whicker, C. A.: Improved representation of the global dust cycle using observational constraints on dust properties and abundance, *Atmospheric Chemistry and Physics*, 21, 8127–8167, <https://doi.org/10.5194/acp-21-8127-2021>, publisher: Copernicus GmbH, 2021.
- Krätschmer, S., van der Does, M., Lamy, F., Lohmann, G., Voelker, C., and Werner, M.: Simulating glacial dust changes in the Southern Hemisphere using ECHAM6.3-HAM2.3, *Climate of the Past*, 18, 67–87, <https://doi.org/10.5194/cp-18-67-2022>, 2022.
- Lamarque, J.-F., Bond, T. C., Eyring, V., Granier, C., Heil, A., Klimont, Z., Lee, D., Liousse, C., Mieville, A., Owen, B., Schultz, M. G., Shindell, D., Smith, S. J., Stehfest, E., Van Aardenne, J., Cooper, O. R., Kainuma, M., Mahowald, N., McConnell, J. R., Naik, V., Riahi, K., and van Vuuren, D. P.: Historical (1850–2000) gridded anthropogenic and biomass burning emissions of reactive gases and aerosols: methodology and application, *Atmospheric Chemistry and Physics*, 10, 7017–7039, <https://doi.org/10.5194/acp-10-7017-2010>, publisher: Copernicus GmbH, 2010.
- Lambert, F., Delmonte, B., Petit, J. R., Bigler, M., Kaufmann, P. R., Hutterli, M. A., Stocker, T. F., Ruth, U., Steffensen, J. P., and Maggi, V.: Dust-climate couplings over the past 800,000 years from the EPICA Dome C ice core, *Nature*, 452, 616–619, <https://doi.org/10.1038/nature06763>, 2008.
- Lambert, F., Tagliabue, A., Shaffer, G., Lamy, F., Winckler, G., Farias, L., Gallardo, L., and De Pol-Holz, R.: Dust fluxes and iron fertilization in Holocene and Last Glacial Maximum climates: Dust and Iron Fertilization, *Geophysical Research Letters*, 42, 6014–6023, <https://doi.org/10.1002/2015GL064250>, 2015.

## References

---

- Lamy, F., Gersonde, R., Winckler, G., Esper, O., Jaeschke, A., Kuhn, G., Ullermann, J., Martinez-Garcia, A., Lambert, F., and Kilian, R.: Increased Dust Deposition in the Pacific Southern Ocean During Glacial Periods, *Science*, 343, 403–407, <https://doi.org/10.1126/science.1245424>, publisher: American Association for the Advancement of Science Section: Report, 2014.
- Laurent, B., Marticorena, B., Bergametti, G., Tegen, I., Schepanski, K., and Heinold, B.: Modelling mineral dust emissions, *IOP Conference Series: Earth and Environmental Science*, 7, 012006, <https://doi.org/10.1088/1755-1307/7/1/012006>, 2009.
- Lay, T., Hernlund, J., and Buffett, B. A.: Core–mantle boundary heat flow, *Nature Geoscience*, 1, 25–32, <https://doi.org/10.1038/ngeo.2007.44>, number: 1 Publisher: Nature Publishing Group, 2008.
- Lenton, T. M., Held, H., Kriegler, E., Hall, J. W., Lucht, W., Rahmstorf, S., and Schellnhuber, H. J.: Tipping elements in the Earth's climate system, *Proceedings of the National Academy of Sciences*, 105, 1786–1793, <https://doi.org/10.1073/pnas.0705414105>, 2008.
- Li, F., Ginoux, P., and Ramaswamy, V.: Distribution, transport, and deposition of mineral dust in the Southern Ocean and Antarctica: Contribution of major sources, *Journal of Geophysical Research*, 113, D10207, <https://doi.org/10.1029/2007JD009190>, 2008.
- Li, F., Ginoux, P., and Ramaswamy, V.: Transport of Patagonian dust to Antarctica, *Journal of Geophysical Research: Atmospheres*, 115, <https://doi.org/https://doi.org/10.1029/2009JD012356>, \_eprint: <https://agupubs.onlinelibrary.wiley.com/doi/pdf/10.1029/2009JD012356>, 2010.
- Lin, M.-K. and Youdin, A. N.: A Thermodynamic View of Dusty Protoplanetary Disks, *The Astrophysical Journal*, 849, 129, <https://doi.org/10.3847/1538-4357/aa92cd>, publisher: American Astronomical Society, 2017.
- Lin, S.-J. and Rood, R.: Multidimensional Flux-Form Semi-Lagrangian Transport Schemes, *Mon. Wea. Rev.*, 124, 2046–2070, [https://doi.org/10.1175/1520-0493\(1996\)124<2046:MFFSLT>2.0.CO;2](https://doi.org/10.1175/1520-0493(1996)124<2046:MFFSLT>2.0.CO;2), 1996.
- Lohmann, G. and Lorenz, S.: On the hydrological cycle under paleoclimatic conditions as derived from AGCM simulations, *Journal of Geophysical Research: Atmospheres*, 105, 17417–17436, <https://doi.org/10.1029/2000JD900189>, \_eprint: <https://onlinelibrary.wiley.com/doi/pdf/10.1029/2000JD900189>, 2000.
- Lohmann, G., Wagner, A., and Prange, M.: Resolution of the atmospheric model matters for the Northern Hemisphere Mid-Holocene climate, *Dynamics of Atmospheres and Oceans*, 93, 101–206, <https://doi.org/10.1016/j.jdynatmoce.2021.101206>, 2021.
- Lohmann, U. and Hoose, C.: Sensitivity studies of different aerosol indirect effects in mixed-phase clouds, *Atmospheric Chemistry and Physics*, 9, 8917–8934, <https://doi.org/10.5194/acp-9-8917-2009>, publisher: Copernicus GmbH, 2009.
- Lohmann, U. and Roeckner, E.: Design and performance of a new cloud microphysics scheme developed for the ECHAM general circulation model, *Climate Dynamics*, 12, 557–572, <https://doi.org/10.1007/BF00207939>, 1996.
- Lohmann, U., Stier, P., Hoose, C., Ferrachat, S., Kloster, S., Roeckner, E., and Zhang, J.: Cloud microphysics and aerosol indirect effects in the global climate model ECHAM5-HAM, *Atmos. Chem. Phys.*, p. 22, 2007.
- Loomis, S. E., Russell, J. M., Verschuren, D., Morrill, C., De Cort, G., Sinninghe Damsté, J. S., Olago, D., Eggermont, H., Street-Perrott, F. A., and Kelly, M. A.: The tropical lapse rate steepened during the Last Glacial Maximum, *Science Advances*, 3, e1600815, <https://doi.org/10.1126/sciadv.1600815>, publisher: American Association for the Advancement of Science, 2017.
- Lott, F.: Alleviation of Stationary Biases in a GCM through a Mountain Drag Parameterization Scheme and a Simple Representation of Mountain Lift Forces, *Monthly Weather Review*, 127, 788–801, [https://doi.org/10.1175/1520-0493\(1999\)127<0788:AOSBIA>2.0.CO;2](https://doi.org/10.1175/1520-0493(1999)127<0788:AOSBIA>2.0.CO;2), publisher: American Meteorological Society Section: Monthly Weather Review, 1999.
- Loutre, M.: ICE AGES (MILANKOVITCH THEORY), in: *Encyclopedia of Atmospheric Sciences*, pp. 995–1003, Elsevier, URL [https://www.semanticscholar.org/paper/ICE-AGES-\(MILANKOVITCH-THEORY\)-Loutre/295bb27fafd030489e04d9c770436f13b458af0a](https://www.semanticscholar.org/paper/ICE-AGES-(MILANKOVITCH-THEORY)-Loutre/295bb27fafd030489e04d9c770436f13b458af0a), 2003.

## References

- Lunt, D. J. and Valdes, P. J.: Dust transport to Dome C, Antarctica, at the Last Glacial Maximum and present day, *Geophysical Research Letters*, 28, 295–298, <https://doi.org/10.1029/2000GL012170>, \_eprint: <https://onlinelibrary.wiley.com/doi/pdf/10.1029/2000GL012170>, 2001.
- Lunt, D. J. and Valdes, P. J.: Dust deposition and provenance at the Last Glacial Maximum and present day, *Geophysical Research Letters*, 29, 42–1–42–4, <https://doi.org/https://doi.org/10.1029/2002GL015656>, \_eprint: <https://agupubs.onlinelibrary.wiley.com/doi/pdf/10.1029/2002GL015656>, 2002.
- Maher, B. A., Prospero, J. M., Mackie, D., Gaiero, D., Hesse, P. P., and Balkanski, Y.: Global connections between aeolian dust, climate and ocean biogeochemistry at the present day and at the last glacial maximum, *Earth-Science Reviews*, 99, 61–97, <https://doi.org/10.1016/j.earscirev.2009.12.001>, 2010.
- Mahowald, N., Albani, S., Kok, J. F., Engelstaeder, S., Scanza, R., Ward, D. S., and Flanner, M. G.: The size distribution of desert dust aerosols and its impact on the Earth system, *Aeolian Research*, 15, 53–71, <https://doi.org/10.1016/j.aeolia.2013.09.002>, 2014.
- Mahowald, N. M., Muhs, D. R., Levis, S., Rasch, P. J., Yoshioka, M., Zender, C. S., and Luo, C.: Change in atmospheric mineral aerosols in response to climate: Last glacial period, preindustrial, modern, and doubled carbon dioxide climates, *Journal of Geophysical Research: Atmospheres*, 111, <https://doi.org/https://doi.org/10.1029/2005JD006653>, \_eprint: <https://agupubs.onlinelibrary.wiley.com/doi/pdf/10.1029/2005JD006653>, 2006.
- Manabe, S. and Stouffer, R. J.: Two Stable Equilibria of a Coupled Ocean-Atmosphere Model, *Journal of Climate*, 1, 841–866, [https://doi.org/10.1175/1520-0442\(1988\)001<0841:TSEOAC>2.0.CO;2](https://doi.org/10.1175/1520-0442(1988)001<0841:TSEOAC>2.0.CO;2), publisher: American Meteorological Society Section: *Journal of Climate*, 1988.
- Markgraf, V., Dodson, J. R., Kershaw, A. P., McGlone, M. S., and Nicholls, N.: Evolution of late pleistocene and holocene climates in the circum-south pacific land areas, *Climate Dynamics*, 6, 193–211, <https://doi.org/10.1007/BF00193532>, 1992.
- Markle, B. R., Steig, E. J., Roe, G. H., Winckler, G., and McConnell, J. R.: Concomitant variability in high-latitude aerosols, water isotopes and the hydrologic cycle, *Nature Geoscience*, 11, 853–859, <https://doi.org/10.1038/s41561-018-0210-9>, bandiera\_abtest: a Cg\_type: Nature Research Journals Number: 11 Primary\_atype: Research Publisher: Nature Publishing Group Subject\_term: Atmospheric science;Climate sciences;Cryospheric science;Geochemistry;Palaeoclimate Subject\_term\_id: atmospheric-science;climate-sciences;cryospheric-science;geochemistry;palaeoclimate, 2018.
- Marticorena, B. and Bergametti, G.: Modeling the atmospheric dust cycle: 1. Design of a soil-derived dust emission scheme, *Journal of Geophysical Research*, 100, 16 415, <https://doi.org/10.1029/95JD00690>, 1995.
- Marticorena, B., Bergametti, G., Aumont, B., Callot, Y., N'Doumé, C., and Legrand, M.: Modeling the atmospheric dust cycle: 2. Simulation of Saharan dust sources, *Journal of Geophysical Research: Atmospheres*, 102, 4387–4404, <https://doi.org/https://doi.org/10.1029/96JD02964>, \_eprint: <https://agupubs.onlinelibrary.wiley.com/doi/pdf/10.1029/96JD02964>, 1997.
- Martin, J. H.: Glacial-interglacial CO<sub>2</sub> change: The Iron Hypothesis, *Paleoceanography*, 5, 1–13, <https://doi.org/https://doi.org/10.1029/PA005i001p00001>, \_eprint: <https://agupubs.onlinelibrary.wiley.com/doi/pdf/10.1029/PA005i001p00001>, 1990.
- Martin, J. H. and Fitzwater, S. E.: Iron deficiency limits phytoplankton growth in the north-east Pacific subarctic, *Nature*, 331, 341–343, <https://doi.org/10.1038/331341a0>, 1988.
- Martin, J. H., Gordon, R. M., and Fitzwater, S. E.: Iron in Antarctic waters, *Nature*, 345, 156–158, <https://doi.org/10.1038/345156a0>, bandiera\_abtest: a Cg\_type: Nature Research Journals Number: 6271 Primary\_atype: Research Publisher: Nature Publishing Group, 1990.
- Martínez-García, A., Rosell-Melé, A., Jaccard, S. L., Geibert, W., Sigman, D. M., and Haug, G. H.: Southern Ocean dust–climate coupling over the past four million years, *Nature*, 476, 312–315, <https://doi.org/10.1038/nature10310>, number: 7360 Publisher: Nature Publishing Group, 2011.

## References

---

- Martínez-García, A., Sigman, D., Ren, H., Anderson, R., Straub, M., Hodell, D., Jaccard, S., Eglinton, T., and Haug, G.: Iron Fertilization of the Subantarctic Ocean During the Last Ice Age. *Science (New York, N.Y.)*, 343, 1347–50, <https://doi.org/10.1126/science.1246848>, 2014.
- Masson-Delmotte, V., Schulz, M., Abe-Ouchi, A., Beer, J., Ganopolski, A., Gonzalez Rouco, J., Jansen, E., Lambeck, K., Luterbacher, J., Naish, T., Osborn, T., Otto-Bliesner, B., Quinn, T., Ramesh, R., Rojas, M., Shao, X., and Timmermann, A.: Information from paleoclimate archives, in: *Climate change 2013: the physical science basis*, edited by Stocker, T., Qin, D., Plattner, G.-K., Tignor, M., Allen, S., Boschung, J., Nauels, A., Xia, Y., Bex, V., and Midgley, P., pp. 383–464, Cambridge University Press, <https://doi.org/10.1017/CBO9781107415324.013>, 2013.
- Masson-Delmotte, V., Zhai, P., Pirani, A., Connors, S., Péan, C., Berger, S., Caud, N., Chen, Y., Goldfarb, L., Gomis, M. I., Huang, M., Leitzell, K., Lonnoy, E., Matthews, J. B. R., Maycock, T., Waterfield, T., Yelekçi, O., Yu, R., and Zhou, B., eds.: *Climate Change 2021: The Physical Science Basis. Contribution of Working Group I to the Sixth Assessment Report of the Intergovernmental Panel on Climate Change*, Cambridge University Press, 2021.
- McGee, D., Broecker, W. S., and Winckler, G.: Gustiness: The driver of glacial dustiness?, *Quaternary Science Reviews*, 29, 2340–2350, <https://doi.org/10.1016/j.quascirev.2010.06.009>, 2010.
- McGee, D., Winckler, G., Borunda, A., Serno, S., Anderson, R., Recasens, C., Bory, A., Gaiero, D., Jaccard, S., Kaplan, M., McManus, J., Revel, M., and Sun, Y.: Tracking eolian dust with helium and thorium: Impacts of grain size and provenance, *Geochimica et Cosmochimica Acta*, 175, <https://doi.org/10.1016/j.gca.2015.11.023>, 2015.
- McGowan, H. A., Petherick, L. M., and Kamber, B. S.: Aeolian sedimentation and climate variability during the late Quaternary in southeast Queensland, Australia, *Palaeogeography, Palaeoclimatology, Palaeoecology*, 265, 171–181, <https://doi.org/10.1016/j.palaeo.2008.05.011>, 2008.
- McIntyre, A. and Cline, R.: Seasonal reconstructions of the earth's surface at the last glacial maximum, num Pages: 18 Series Number: MC-36 Series: Map and chart series / Geological Society of America, 1981.
- McMurdie, W. L. and Houze, R. A.: 8 - Weather Systems, in: *Atmospheric Science (Second Edition)*, edited by Wallace, J. M. and Hobbs, P. V., pp. 313–373, Academic Press, San Diego, <https://doi.org/10.1016/B978-0-12-732951-2.50013-2>, 2006.
- McMurry, P. H.: AEROSOLS | Observations and Measurements, in: *Encyclopedia of Atmospheric Sciences*, pp. 20–34, Elsevier, 2003.
- Meehl, G. A., Senior, C. A., Eyring, V., Flato, G., Lamarque, J.-F., Stouffer, R. J., Taylor, K. E., and Schlund, M.: Context for interpreting equilibrium climate sensitivity and transient climate response from the CMIP6 Earth system models, *Science Advances*, 6, <https://doi.org/10.1126/sciadv.aba1981>, publisher: American Association for the Advancement of Science, 2020.
- Meyer, V. D., Hefter, J., Lohmann, G., Max, L., Tiedemann, R., and Mollenhauer, G.: Summer temperature evolution on the Kamchatka Peninsula, Russian Far East, during the past 20 000 years, *Climate of the Past*, 13, 359–377, <https://doi.org/10.5194/cp-13-359-2017>, publisher: Copernicus GmbH, 2017.
- Milankovitch, M.: Canon of insolation and the iceage problem, *Koniglich Serbische Akademie Beograd Special Publication*, 132, publisher: U. S. Dept. of Commerce and National Science Foundation, 1941.
- Miller, M. J., Palmer, T. N., and Swinbank, R.: Parametrization and influence of subgridscale orography in general circulation and numerical weather prediction models, *Meteorology and Atmospheric Physics*, 40, 84–109, <https://doi.org/10.1007/BF01027469>, 1989.
- Mix, A., Morey, A., Piasias, N., and Hostetler, S.: Foraminiferal faunal estimates of paleotemperature: Circumventing the No-analog problem yields cool Ice Age tropics, *Paleoceanography*, 14, <https://doi.org/10.1029/1999PA900012>, 1999.
- Morman, S. A. and Plumlee, G. S.: The role of airborne mineral dusts in human disease, *Aeolian Research*, 9, 203–212, <https://doi.org/10.1016/j.aeolia.2012.12.001>, 2013.

## References

---

- Muglia, J., Somes, C. J., Nickelsen, L., and Schmittner, A.: Combined Effects of Atmospheric and Seafloor Iron Fluxes to the Glacial Ocean: LAST GLACIAL MAXIMUM OCEAN IRON CYCLE, *Paleoceanography*, 32, 1204–1218, <https://doi.org/10.1002/2016PA003077>, 2017.
- Neubauer, D., Ferrachat, S., Siegenthaler-Le Drian, C., Stier, P., Partridge, D. G., Tegen, I., Bey, I., Stanelle, T., Kokkola, H., and Lohmann, U.: The global aerosol–climate model ECHAM6.3–HAM2.3 – Part 2: Cloud evaluation, aerosol radiative forcing, and climate sensitivity, *Geoscientific Model Development*, 12, 3609–3639, <https://doi.org/10.5194/gmd-12-3609-2019>, 2019.
- Otto-Bliesner, B. L., Brady, E. C., Clauzet, G., Tomas, R., Levis, S., and Kothavala, Z.: Last Glacial Maximum and Holocene Climate in CCSM3, *Journal of Climate*, 19, 2526–2544, <https://doi.org/10.1175/JCLI3748.1>, publisher: American Meteorological Society Section: *Journal of Climate*, 2006.
- Palmer, T. N., Shutts, G. J., and Swinbank, R.: Alleviation of a systematic westerly bias in general circulation and numerical weather prediction models through an orographic gravity wave drag parametrization, *Quarterly Journal of the Royal Meteorological Society*, 112, 1001–1039, <https://doi.org/10.1002/qj.49711247406>, \_eprint: <https://onlinelibrary.wiley.com/doi/pdf/10.1002/qj.49711247406>, 1986.
- Paul, A. and Schäfer-Neth, C.: Modeling the water masses of the Atlantic Ocean at the Last Glacial Maximum, *Paleoceanography*, 18, <https://doi.org/10.1029/2002PA000783>, 2003.
- Paul, A., Mulitza, S., Stein, R., and Werner, M.: A global climatology of the ocean surface during the Last Glacial Maximum mapped on a regular grid (GLOMAP), *Climate of the Past*, 17, 805–824, <https://doi.org/10.5194/cp-17-805-2021>, publisher: Copernicus GmbH, 2021.
- Peixoto, J. P. and Oort, A. H.: *Physics of Climate*, Springer, New York, URL <https://link.springer.com/book/9780883187128>, 1992.
- Penner, J., Andreae, M., Annegarn, H., Barrie, L., Feichter, J., Hegg, D., Achuthan, J., Leaitch, R., Murphy, D., Nganga, J., and Pitari, G.: Aerosols, their Direct and Indirect Effects, *Climate Change 2001: The Scientific Basis. Contribution of Working Group I to the Third Assessment Report of the Intergovernmental Panel on Climate Change*, 289–348 (2001), 2001.
- Pitchford, J.: Iron limitation, grazing pressure and oceanic high nutrient-low chlorophyll (HNLC) regions, *Journal of Plankton Research*, 21, 525–547, <https://doi.org/10.1093/plankt/21.3.525>, 1999.
- Powers, L., Johnson, T. C., Werne, J., Castañeda, I., EC, H., Sinninghe-Damste, J., and Schouten, S.: Large temperature variability in the southern African tropics since the Last Glacial Maximum, *Geophysical Research Letters*, 32, <https://doi.org/10.1029/2004GL022014>, 2005.
- Pérez, C., Nickovic, S., Pejanovic, G., Baldasano, J. M., and Özsoy, E.: Interactive dust-radiation modeling: A step to improve weather forecasts, *Journal of Geophysical Research: Atmospheres*, 111, <https://doi.org/10.1029/2005JD006717>, \_eprint: <https://onlinelibrary.wiley.com/doi/pdf/10.1029/2005JD006717>, 2006.
- Ray, N. and Adams, J.: A GIS-based vegetation map of the world at the Last Glacial Maximum (25,000–15,000 BP), *Internet Archaeology*, 11, URL <https://archive-ouverte.unige.ch/unige:17817>, 2001.
- Rea, D. K.: The paleoclimatic record provided by eolian deposition in the deep sea: The geologic history of wind, *Reviews of Geophysics*, 32, 159–195, <https://doi.org/10.1029/93RG03257>, \_eprint: <https://onlinelibrary.wiley.com/doi/pdf/10.1029/93RG03257>, 1994.
- Reichholf, J. H.: Is Saharan Dust a Major Source of Nutrients for the Amazonian Rain Forest?, *Studies on Neotropical Fauna and Environment*, 21, 251–255, <https://doi.org/10.1080/01650528609360710>, publisher: Taylor & Francis \_eprint: <https://doi.org/10.1080/01650528609360710>, 1986.
- Reick, C. H., Raddatz, T., Brovkin, V., and Gayler, V.: Representation of natural and anthropogenic land cover change in MPI-ESM, *Journal of Advances in Modeling Earth Systems*, 5, 459–482, <https://doi.org/https://doi.org/10.1002/jame.20022>, \_eprint: <https://agupubs.onlinelibrary.wiley.com/doi/pdf/10.1002/jame.20022>, 2013.

## References

---

- Richter, D. and Gill, T.: Challenges and Opportunities in Atmospheric Dust Emission, Chemistry, and Transport, *Bulletin of the American Meteorological Society*, 99, ES115–ES118, <https://doi.org/10.1175/BAMS-D-18-0007.1>, publisher: American Meteorological Society Section: Bulletin of the American Meteorological Society, 2018.
- Ridgwell, A. J. and Watson, A. J.: Feedback between aeolian dust, climate, and atmospheric CO<sub>2</sub> in glacial time: GLACIAL DUST-CO<sub>2</sub> -CLIMATE FEEDBACK, *Paleoceanography*, 17, 11–1–11–11, <https://doi.org/10.1029/2001PA000729>, 2002.
- Robinson, J., Popova, E. E., Yool, A., Srokosz, M., Lampitt, R. S., and Blundell, J. R.: How deep is deep enough? Ocean iron fertilization and carbon sequestration in the Southern Ocean, *Geophysical Research Letters*, 41, 2489–2495, <https://doi.org/10.1002/2013GL058799>, 2014.
- Roeckner, E., Brokopf, R., Esch, M., Giorgetta, M., Hagemann, S., Kornblueh, L., Manzini, E., Schlese, U., and Schulzweida, U.: Sensitivity of Simulated Climate to Horizontal and Vertical Resolution in the ECHAM5 Atmosphere Model, *Journal of Climate*, 19, 3771–3791, <https://doi.org/10.1175/JCLI3824.1>, 2006.
- Rojas, M., Kageyama, M., Crucifix, M., Hewitt, C., Abe-Ouchi, A., Ohgaito, R., Brady, E., and Hope, P.: The Southern Westerlies during the Last Glacial Maximum in PMIP2 simulations, *Climate Dynamics*, 32, 525–548, <https://doi.org/10.1007/s00382-008-0421-7>, 2009.
- Romanova, V., Lohmann, G., Grosfeld, K., and Butzin, M.: The relative role of oceanic heat transport and orography on glacial climate, *Quaternary science reviews*, 25, 832–845, <https://doi.org/10.1016/j.quascirev.2005.07.007>, number: 7, 2006.
- Ruddiman, W.: *Earth's Climate: Past and Future*, WH Freeman, New York, 3rd ed. 2013 edition edn., 2013.
- Rue, E. L. and Bruland, K. W.: The role of organic complexation on ambient iron chemistry in the equatorial Pacific Ocean and the response of a mesoscale iron addition experiment, *Limnology and Oceanography*, 42, 901–910, <https://doi.org/10.4319/lo.1997.42.5.0901>, [\\_eprint: https://onlinelibrary.wiley.com/doi/pdf/10.4319/lo.1997.42.5.0901](https://onlinelibrary.wiley.com/doi/pdf/10.4319/lo.1997.42.5.0901), 1997.
- Sarmiento, J. L. and Gruber, N.: *Ocean Biogeochemical Dynamics*, Princeton University Press, URL <https://press.princeton.edu/books/hardcover/9780691017075/ocean-biogeochemical-dynamics>, 2006.
- Sawyer, J. S.: The vertical circulation at meteorological fronts and its relation to frontogenesis | *Proceedings of the Royal Society of London. Series A. Mathematical and Physical Sciences*, URL <https://royalsocietypublishing.org/doi/abs/10.1098/rspa.1956.0039>, 1956.
- Schepanski, K.: Transport of Mineral Dust and Its Impact on Climate, *Geosciences*, 8, 151, <https://doi.org/10.3390/geosciences8050151>, number: 5 Publisher: Multidisciplinary Digital Publishing Institute, 2018.
- Schmittner, A. and Galbraith, E. D.: Glacial greenhouse-gas fluctuations controlled by ocean circulation changes, *Nature*, 456, 373–376, <https://doi.org/10.1038/nature07531>, 2008.
- Schmittner, A., Urban, N. M., Shakun, J. D., Mahowald, N. M., Clark, P. U., Bartlein, P. J., Mix, A. C., and Rosell-Melé, A.: Climate Sensitivity Estimated from Temperature Reconstructions of the Last Glacial Maximum, *Science*, 334, 1385–1388, <https://doi.org/10.1126/science.1203513>, publisher: American Association for the Advancement of Science, 2011.
- Schneider von Deimling, T., Ganopolski, A., Held, H., and Rahmstorf, S.: How cold was the Last Glacial Maximum?, *Geophysical Research Letters*, 33, <https://doi.org/10.1029/2006GL026484>, [\\_eprint: https://onlinelibrary.wiley.com/doi/pdf/10.1029/2006GL026484](https://onlinelibrary.wiley.com/doi/pdf/10.1029/2006GL026484), 2006.
- Schourup-Kristensen, V., Sidorenko, D., Wolf-Gladrow, D. A., and Völker, C.: A skill assessment of the biogeochemical model REcoM2 coupled to the Finite Element Sea Ice–Ocean Model (FESOM 1.3), *Geoscientific Model Development*, 7, 2769–2802, <https://doi.org/10.5194/gmd-7-2769-2014>, 2014.
- Schultz, M. G., Stadtler, S., Schröder, S., Taraborrelli, D., Franco, B., Krefting, J., Henrot, A., Ferrachat, S., Lohmann, U., Neubauer, D., Siegenthaler-Le Drian, C., Wahl, S., Kokkola, H., Kühn, T., Rast, S., Schmidt, H., Stier, P., Kinnison, D., Tyndall, G. S., Orlando, J. J., and Wespes, C.: The chemistry–climate model ECHAM6.3-HAM2.3-MOZ1.0, *Geoscientific Model Development*, 11, 1695–1723, <https://doi.org/10.5194/gmd-11-1695-2018>, 2018.

## References

- Schweitzer, M. D., Calzadilla, A. S., Salamo, O., Sharifi, A., Kumar, N., Holt, G., Campos, M., and Mirsaedi, M.: Lung health in era of climate change and dust storms, *Environmental Research*, 163, 36–42, <https://doi.org/10.1016/j.envres.2018.02.001>, 2018.
- Seltzer, A. M., Ng, J., Aeschbach, W., Kipfer, R., Kulongoski, J. T., Severinghaus, J. P., and Stute, M.: Widespread six degrees Celsius cooling on land during the Last Glacial Maximum, *Nature*, 593, 228–232, <https://doi.org/10.1038/s41586-021-03467-6>, number: 7858 Publisher: Nature Publishing Group, 2021.
- Shackleton, N. J.: Carbon-13 in Uvigerina: Tropical Rainforest History and the Equatorial Pacific Carbonate Dissolution Cycles., Tech. Rep. ADA049905, Lamont-Doherty Geological Observatory Palisades N Y, URL <https://ntrl.ntis.gov/NTRL/dashboard/searchResults/titleDetail/ADA049905.xhtml>, num Pages: 28, 1977.
- Shao, Y.: Physics and Modelling of Wind Erosion, Springer Dordrecht, 2 edn., URL <https://link.springer.com/book/10.1007/978-1-4020-8895-7>, <https://doi.org/10.1007/978-1-4020-8895-7>, 2008.
- Shao, Y., Wyrwoll, K.-H., Chappell, A., Huang, J., Lin, Z., McTainsh, G. H., Mikami, M., Tanaka, T. Y., Wang, X., and Yoon, S.: Dust cycle: An emerging core theme in Earth system science, *Aeolian Research*, 2, 181–204, <https://doi.org/10.1016/j.aeolia.2011.02.001>, 2011.
- Shapiro, M. A.: Frontogenesis and Geostrophically Forced Secondary Circulations in the Vicinity of Jet Stream-Frontal Zone Systems, *Journal of the Atmospheric Sciences*, 38, 954–973, [https://doi.org/10.1175/1520-0469\(1981\)038<0954:FAGFSC>2.0.CO;2](https://doi.org/10.1175/1520-0469(1981)038<0954:FAGFSC>2.0.CO;2), publisher: American Meteorological Society Section: Journal of the Atmospheric Sciences, 1981.
- Shikazono, N.: Components of the Earth System, in: Introduction to Earth and Planetary System Science: New View of Earth, Planets and Humans, edited by Shikazono, N., pp. 11–41, Springer Japan, Tokyo, [https://doi.org/10.1007/978-4-431-54058-8\\_2](https://doi.org/10.1007/978-4-431-54058-8_2), 2012.
- Shin, S.-I., Liu, Z., Otto-Bliesner, B., Brady, E., Kutzbach, J., and Harrison, S.: A Simulation of the Last Glacial Maximum climate using the NCAR-CCSM, *Climate Dynamics*, 20, 127–151, <https://doi.org/10.1007/s00382-002-0260-x>, 2003.
- Shoenfelt, E. M., Winckler, G., Lamy, F., Anderson, R. F., and Bostick, B. C.: Highly bioavailable dust-borne iron delivered to the Southern Ocean during glacial periods, *Proceedings of the National Academy of Sciences*, 115, 11 180–11 185, <https://doi.org/10.1073/pnas.1809755115>, 2018.
- Sime, L. C., Kohfeld, K. E., Le Quéré, C., Wolff, E. W., de Boer, A. M., Graham, R. M., and Bopp, L.: Southern Hemisphere westerly wind changes during the Last Glacial Maximum: model-data comparison, *Quaternary Science Reviews*, 64, 104–120, <https://doi.org/10.1016/j.quascirev.2012.12.008>, 2013.
- Simmons, A. J. and Jiabin, C.: The calculation of geopotential and the pressure gradient in the ECMWF atmospheric model: Influence on the simulation of the polar atmosphere and on temperature analyses, *Quarterly Journal of the Royal Meteorological Society*, 117, 29–58, <https://doi.org/https://doi.org/10.1002/qj.49711749703>, <https://rmets.onlinelibrary.wiley.com/doi/pdf/10.1002/qj.49711749703>, 1991.
- Simmons, A. J., Burridge, D. M., Jarraud, M., Girard, C., and Wergen, W.: The ECMWF medium-range prediction models development of the numerical formulations and the impact of increased resolution, *Meteorology and Atmospheric Physics*, 40, 28–60, <https://doi.org/10.1007/BF01027467>, 1989.
- Smetacek, V., Klaas, C., Strass, V. H., Assmy, P., Montresor, M., Cisewski, B., Savoye, N., Webb, A., d'Ovidio, F., Arrieta, J. M., Bathmann, U., Bellerby, R., Berg, G. M., Croot, P., Gonzalez, S., Henjes, J., Herndl, G. J., Hoffmann, L. J., Leach, H., Losch, M., Mills, M. M., Neill, C., Peeken, I., Röttgers, R., Sachs, O., Sauter, E., Schmidt, M. M., Schwarz, J., Terbrüggen, A., and Wolf-Gladrow, D.: Deep carbon export from a Southern Ocean iron-fertilized diatom bloom, *Nature*, 487, 313–319, <https://doi.org/10.1038/nature11229>, 2012.
- Smoluchowski, M. v.: Versuch einer mathematischen Theorie der Koagulationskinetik kolloider Lösungen, *Zeitschrift für Physikalische Chemie*, 92U, 129–168, <https://doi.org/10.1515/zpch-1918-9209>, publisher: De Gruyter (O), 1918.

## References

---

- Spracklen, D. V., Carslaw, K. S., Kulmala, M., Kerminen, V.-M., Sihto, S.-L., Riipinen, I., Merikanto, J., Mann, G. W., Chipperfield, M. P., Wiedensohler, A., Birmili, W., and Lihavainen, H.: Contribution of particle formation to global cloud condensation nuclei concentrations, *Geophysical Research Letters*, 35, <https://doi.org/https://doi.org/10.1029/2007GL033038>, \_eprint: <https://agupubs.onlinelibrary.wiley.com/doi/pdf/10.1029/2007GL033038>, 2008.
- Stanelle, T., Bey, I., Raddatz, T., Reick, C., and Tegen, I.: Anthropogenically induced changes in twentieth century mineral dust burden and the associated impact on radiative forcing, *Journal of Geophysical Research: Atmospheres*, 119, 13,526–13,546, <https://doi.org/https://doi.org/10.1002/2014JD022062>, \_eprint: <https://agupubs.onlinelibrary.wiley.com/doi/pdf/10.1002/2014JD022062>, 2014.
- Steffensen, J. P.: The size distribution of microparticles from selected segments of the Greenland Ice Core Project ice core representing different climatic periods, *Journal of Geophysical Research: Oceans*, 102, 26 755–26 763, <https://doi.org/https://doi.org/10.1029/97JC01490>, \_eprint: <https://agupubs.onlinelibrary.wiley.com/doi/pdf/10.1029/97JC01490>, 1997.
- Steig, E. J.: PALEOCLIMATOLOGY | Ice Cores, in: *Encyclopedia of Atmospheric Sciences*, pp. 1673–1680, Elsevier, 2003.
- Stevens, B., Giorgetta, M., Esch, M., Mauritsen, T., Crueger, T., Rast, S., Salzmann, M., Schmidt, H., Bader, J., Block, K., Brokopf, R., Fast, I., Kinne, S., Kornbluh, L., Lohmann, U., Pincus, R., Reichler, T., and Roeckner, E.: Atmospheric component of the MPI-M Earth System Model: ECHAM6, *Journal of Advances in Modeling Earth Systems*, 5, 146–172, <https://doi.org/10.1002/jame.20015>, \_eprint: <https://onlinelibrary.wiley.com/doi/pdf/10.1002/jame.20015>, 2013.
- Stier, P., Feichter, J., Kinne, S., Kloster, S., Vignati, E., Wilson, J., Ganzeveld, L., Tegen, I., Werner, M., Balkanski, Y., Schulz, M., Boucher, O., Minikin, A., and Petzold, A.: The aerosol-climate model ECHAM5-HAM, *Atmospheric Chemistry and Physics*, 5, 1125–1156, <https://doi.org/10.5194/acp-5-1125-2005>, publisher: Copernicus GmbH, 2005.
- Stocker, T.: Introduction to Climate Modelling, <https://doi.org/10.1007/978-3-642-00773-6>, journal Abbreviation: Introduction to Climate Modelling, by Stocker, Thomas. ISBN: 978-3-642-00772-9. Berlin: Springer, 2011 Publication Title: Introduction to Climate Modelling, by Stocker, Thomas. ISBN: 978-3-642-00772-9. Berlin: Springer, 2011, 2011.
- Struve, T., Pahnke, K., Lamy, F., Wengler, M., Böning, P., and Winckler, G.: A circumpolar dust conveyor in the glacial Southern Ocean, *Nature Communications*, 11, 5655, <https://doi.org/10.1038/s41467-020-18858-y>, number: 1 Publisher: Nature Publishing Group, 2020.
- Stärz, M., Lohmann, G., and Knorr, G.: The effect of a dynamic soil scheme on the climate of the mid-Holocene and the Last Glacial Maximum, *Climate of the Past*, 12, 151–170, <https://doi.org/10.5194/cp-12-151-2016>, publisher: Copernicus GmbH, 2016.
- Sundqvist, H., Berge, E., and Kristjánsson, J. E.: Condensation and Cloud Parameterization Studies with a Mesoscale Numerical Weather Prediction Model, *Monthly Weather Review*, 117, 1641, [https://doi.org/10.1175/1520-0493\(1989\)117<1641:CACPSW>2.0.CO;2](https://doi.org/10.1175/1520-0493(1989)117<1641:CACPSW>2.0.CO;2), 1989.
- Takemura, T., Egashira, M., Matsuzawa, K., Ichijo, H., O'ishi, R., and Abe-Ouchi, A.: A simulation of the global distribution and radiative forcing of soil dust aerosols at the Last Glacial Maximum, *Atmospheric Chemistry and Physics*, 9, 3061–3073, <https://doi.org/10.5194/acp-9-3061-2009>, publisher: Copernicus GmbH, 2009.
- Taylor, K., Williamson, D., and Zwiers, F.: AMIP II Sea Surface Temperature and Sea Ice Concentration Boundary Conditions, *PCMDI Rep.*, 60, 2000.
- Tegen, I. and Fung, I.: Modeling of mineral dust in the atmosphere: Sources, transport, and optical thickness, *Journal of Geophysical Research: Atmospheres*, 99, 22 897–22 914, <https://doi.org/https://doi.org/10.1029/94JD01928>, \_eprint: <https://agupubs.onlinelibrary.wiley.com/doi/pdf/10.1029/94JD01928>, 1994.

## References

---

- Tegen, I. and Lacis, A. A.: Modeling of particle size distribution and its influence on the radiative properties of mineral dust aerosol, *Journal of Geophysical Research: Atmospheres*, 101, 19237–19244, <https://doi.org/10.1029/95JD03610>, 1996.
- Tegen, I. and Schepanski, K.: Climate Feedback on Aerosol Emission and Atmospheric Concentrations, *Current Climate Change Reports*, 4, 1–10, <https://doi.org/10.1007/s40641-018-0086-1>, 2018.
- Tegen, I., Harrison, S. P., Kohfeld, K., Prentice, I. C., Coe, M., and Heimann, M.: Impact of vegetation and preferential source areas on global dust aerosol: Results from a model study, *Journal of Geophysical Research: Atmospheres*, 107, AAC 14–1–AAC 14–27, <https://doi.org/https://doi.org/10.1029/2001JD000963>, \_eprint: <https://agupubs.onlinelibrary.wiley.com/doi/pdf/10.1029/2001JD000963>, 2002.
- Tegen, I., Neubauer, D., Ferrachat, S., Siegenthaler-Le Drian, C., Bey, I., Schutgens, N., Stier, P., Watson-Parris, D., Stanelle, T., Schmidt, H., Rast, S., Kokkola, H., Schultz, M., Schroeder, S., Daskalakis, N., Barthel, S., Heinold, B., and Lohmann, U.: The global aerosol–climate model ECHAM6.3–HAM2.3 – Part 1: Aerosol evaluation, *Geoscientific Model Development*, 12, 1643–1677, <https://doi.org/10.5194/gmd-12-1643-2019>, 2019.
- Tharammal, T., Paul, A., Merkel, U., and Noone, D.: Influence of Last Glacial Maximum boundary conditions on the global water isotope distribution in an atmospheric general circulation model, *Climate of the Past*, 9, 789–809, <https://doi.org/10.5194/cp-9-789-2013>, publisher: Copernicus GmbH, 2013.
- Tiedtke, M.: A Comprehensive Mass Flux Scheme for Cumulus Parameterization in Large-Scale Models, *Monthly Weather Review*, 117, 1779–1800, [https://doi.org/10.1175/1520-0493\(1989\)117<1779:ACMFSF>2.0.CO;2](https://doi.org/10.1175/1520-0493(1989)117<1779:ACMFSF>2.0.CO;2), publisher: American Meteorological Society Section: Monthly Weather Review, 1989.
- Tierney, J. E., Zhu, J., King, J., Malevich, S. B., Hakim, G. J., and Poulsen, C. J.: Glacial cooling and climate sensitivity revisited, *Nature*, 584, 569–573, <https://doi.org/10.1038/s41586-020-2617-x>, number: 7822 Publisher: Nature Publishing Group, 2020.
- Toggweiler, J. R.: Variation of atmospheric CO<sub>2</sub> by ventilation of the ocean's deepest water, *Paleoceanography*, 14, 571–588, <https://doi.org/10.1029/1999PA900033>, \_eprint: <https://onlinelibrary.wiley.com/doi/pdf/10.1029/1999PA900033>, 1999.
- Toggweiler, J. R., Russell, J. L., and Carson, S. R.: Midlatitude westerlies, atmospheric CO<sub>2</sub>, and climate change during the ice ages, *Paleoceanography*, 21, <https://doi.org/10.1029/2005PA001154>, \_eprint: <https://onlinelibrary.wiley.com/doi/pdf/10.1029/2005PA001154>, 2006.
- Trudgill, M. D., Shuttleworth, R., Bostock, H. C., Burke, A., Cooper, M. J., Greenop, R., and Foster, G. L.: The Flux and Provenance of Dust Delivered to the SW Pacific During the Last Glacial Maximum, *Paleoceanography and Paleoclimatology*, 35, e2020PA003869, <https://doi.org/10.1029/2020PA003869>, \_eprint: <https://agupubs.onlinelibrary.wiley.com/doi/pdf/10.1029/2020PA003869>, 2020.
- Vallelonga, P.: The enigma of dust provenance: where else does Antarctic dust come from?, *Past Global Changes Magazine*, 22, 74–75, <https://doi.org/10.22498/pages.22.2.74>, 2014.
- van der Does, M., Knippertz, P., Zschenderlein, P., Harrison, R., and Stuut, J.-B.: The mysterious long-range transport of giant mineral dust particles, *Science Advances*, 4, <https://doi.org/10.1126/sciadv.aau2768>, 2018.
- van der Does, M., Wengler, M., Lamy, F., Martínez-García, A., Jaccard, S. L., Kuhn, G., Lanny, V., Stuut, J.-B. W., and Winckler, G.: Opposite dust grain-size patterns in the Pacific and Atlantic sectors of the Southern Ocean during the last 260,000 years, *Quaternary Science Reviews*, 263, 106978, <https://doi.org/10.1016/j.quascirev.2021.106978>, 2021.
- Vignati, E., Wilson, J., and Stier, P.: M7: An efficient size-resolved aerosol microphysics module for large-scale aerosol transport models, *Journal of Geophysical Research: Atmospheres*, 109, <https://doi.org/https://doi.org/10.1029/2003JD004485>, \_eprint: <https://agupubs.onlinelibrary.wiley.com/doi/pdf/10.1029/2003JD004485>, 2004.
- Waelbroeck, Paul, Kucera, M., Rosell-Melé, Wejnets, Schneider, Mix, A., Abelmann, Bard, E., Barker, S., Benways, Cacho, I., Chen, M.-T., Cortijo, Crosta, X., Anne, d. V., Dokken, T., Duprat, Elderfield, and Members, M.: Constraints on the magnitude and patterns of ocean cooling at the Last Glacial Maximum, *Nature Geoscience*, 9, 127–132, <https://doi.org/10.1038/NGEO411>, 2009.

## References

---

- Wallace, J. M. and Hobbs, P. V.: 4 - Radiative Transfer, in: *Atmospheric Science (Second Edition)*, pp. 113–152, Academic Press, San Diego, <https://doi.org/10.1016/B978-0-12-732951-2.50009-0>, 2006.
- Wang, R., Kuhn, G., Gong, X., Biskaborn, B., Gersonde, R., Lembke-Jene, L., Lohmann, G., Tiedemann, R., and Diekmann, B.: Deglacial Land-Ocean Linkages at the Alaskan Continental Margin in the Bering Sea, *Frontiers in Earth Sciences*, 9, 1, <https://doi.org/10.3389/feart.2021.712415>, 2021.
- Wang, S. and Smith, R. K.: Consequences of regularizing the Sawyer–Eliassen equation in balance models for tropical cyclone behaviour, *Quarterly Journal of the Royal Meteorological Society*, 145, 3766–3779, <https://doi.org/10.1002/qj.3656>, <https://onlinelibrary.wiley.com/doi/pdf/10.1002/qj.3656>, 2019.
- Weber, M. E., Bailey, I., Hemming, S. R., Martos, Y. M., Reilly, B. T., Ronge, T. A., Brachfeld, S., Williams, T., Raymo, M., Belt, S. T., Smik, L., Vogel, H., Peck, V. L., Armbrecht, L., Cage, A., Cardillo, F. G., Du, Z., Fauth, G., Fogwill, C. J., Garcia, M., Garnsworthy, M., Glüder, A., Guitard, M., Gutjahr, M., Hernández-Almeida, I., Hoem, F. S., Hwang, J.-H., Iizuka, M., Kato, Y., Kenlee, B., OConnell, S., Pérez, L. F., Seki, O., Stevens, L., Tauxe, L., Tripathi, S., Warnock, J., and Zheng, X.: Antiphased dust deposition and productivity in the Antarctic Zone over 1.5 million years, *Nature Communications*, 13, 2044, <https://doi.org/10.1038/s41467-022-29642-5>, 2022.
- Werner, M., Tegen, I., Harrison, S. P., Kohfeld, K. E., Prentice, I. C., Balkanski, Y., Rodhe, H., and Roelandt, C.: Seasonal and interannual variability of the mineral dust cycle under present and glacial climate conditions, *Journal of Geophysical Research: Atmospheres*, 107, AAC 2–1–AAC 2–19, <https://doi.org/https://doi.org/10.1029/2002JD002365>, <https://agupubs.onlinelibrary.wiley.com/doi/pdf/10.1029/2002JD002365>, 2002.
- White, B. R.: soil transport by winds on Mars, *Journal of Geophysical Research: Solid Earth*, 84, 4643–4651, <https://doi.org/https://doi.org/10.1029/JB084iB09p04643>, [\\_eprint: https://agupubs.onlinelibrary.wiley.com/doi/pdf/10.1029/JB084iB09p04643](https://agupubs.onlinelibrary.wiley.com/doi/pdf/10.1029/JB084iB09p04643), 1979.
- Williams, G. P. and Bryan, K.: Ice Age Winds: An Aquaplanet Model, *Journal of Climate*, 19, 1706–1715, <https://doi.org/10.1175/JCLI3766.1>, publisher: American Meteorological Society Section: *Journal of Climate*, 2006.
- Williams, M., Cook, E., van der Kaars, S., Barrows, T., Shulmeister, J., and Kershaw, P.: Glacial and deglacial climatic patterns in Australia and surrounding regions from 35000 to 10000 years ago reconstructed from terrestrial and near-shore proxy data, *Quaternary Science Reviews*, 28, 2398–2419, <https://doi.org/10.1016/j.quascirev.2009.04.020>, 2009.
- Wilson, J., Cuvelier, C., and Raes, F.: A modeling study of global mixed aerosol fields, *Journal of Geophysical Research: Atmospheres*, 106, 34 081–34 108, <https://doi.org/https://doi.org/10.1029/2000JD000198>, [\\_eprint: https://agupubs.onlinelibrary.wiley.com/doi/pdf/10.1029/2000JD000198](https://agupubs.onlinelibrary.wiley.com/doi/pdf/10.1029/2000JD000198), 2001.
- Wolff, E., Barbante, C., Becagli, S., Bigler, M., Boutron, C., Castellano, E., de Angelis, M., Federer, U., Fischer, H., Fundel, F., Hansson, M., Hutterli, M., Jonsell, U., Karlin, T., Kaufmann, P., Lambert, F., Littot, G., Mulvaney, R., Röthlisberger, R., Ruth, U., Severi, M., Siggaard-Andersen, M., Sime, L., Steffensen, J., Stocker, T., Traversi, R., Twarloh, B., Udisti, R., Wagenbach, D., and Wegner, A.: Changes in environment over the last 800,000 years from chemical analysis of the EPICA Dome C ice core, *Quaternary Science Reviews*, 29, 285–295, <https://doi.org/10.1016/j.quascirev.2009.06.013>, 2010.
- Wyrтки, K.: The thermohaline circulation in relation to the general circulation in the oceans, *Deep Sea Research (1953)*, 8, 39–64, [https://doi.org/10.1016/0146-6313\(61\)90014-4](https://doi.org/10.1016/0146-6313(61)90014-4), 1961.
- Yang, W., Marshak, A., Kostinski, A. B., and Várnai, T.: Shape-induced gravitational sorting of Saharan dust during transatlantic voyage: Evidence from CALIOP lidar depolarization measurements, *Geophysical Research Letters*, 40, 3281–3286, <https://doi.org/10.1002/grl.50603>, [\\_eprint: https://onlinelibrary.wiley.com/doi/pdf/10.1002/grl.50603](https://onlinelibrary.wiley.com/doi/pdf/10.1002/grl.50603), 2013.
- Yin, J. H. and Battisti, D. S.: The Importance of Tropical Sea Surface Temperature Patterns in Simulations of Last Glacial Maximum Climate, *Journal of Climate*, 14, 565–581, [https://doi.org/10.1175/1520-0442\(2001\)014<0565:Tiotss>2.0.CO;2](https://doi.org/10.1175/1520-0442(2001)014<0565:Tiotss>2.0.CO;2), publisher: American Meteorological Society Section: *Journal of Climate*, 2001.

## *References*

---

Zhang, Z.: Multivariate Time Series Analysis in Climate and Environmental Research, Springer, <https://doi.org/10.1007/978-3-319-67340-0>, 2018.

Zhuang, G., Yi, Z., Duce, R. A., and Brown, P. R.: Link between iron and sulphur cycles suggested by detection of Fe (n) in remote marine aerosols, *Nature*, 355, 537–539, publisher: Nature Publishing Group, 1992.

